Order Number 9405548

Interfacial scattering and microparticle resonances in random media

Li, Jiang Hong, Ph.D.

City University of New York, 1993

U·M·I
300 N. Zeeb Rd.
Ann Arbor, MI 48106

INTERFACIAL SCATTERING AND MICROPARTICLE RESONANCES IN RANDOM MEDIA

by

JIANG HONG LI

A dissertation submitted to the Graduate Faculty in Physics in partial fulfillment of the requirements for the degree of Doctor of Philosophy, The City University of New York.

1993

This Manuscript has been read and accepted for the Graduate Faculty in Physics in satisfaction of the dissertation requirement for the degree of Doctor of Philosophy.

September 14, 1993
Date

Chair of Examining Committee

Sept 22, 1993
Date

Executive Officer

Prof. Azriel Z. Genack

Prof. Melvyn Lax

Dr. Ping Sheng

Prof. Narciso Garcia

Prof. Alexander A. Lisyansky

Supervisory Committee

THE CITY UNIVERSITY OF NEW YORK

ACKNOWLEDGMENTS

I am grateful to my thesis supervisor, Professor Azriel Z. Genack, for his continuous support and encouragement throughout this work. Without his guidance in every phase of this work, this thesis would have been impossible. I wish to thank Professor Narciso Garcia for his generous help throughout this thesis work. I wish to thank Professor Alexander A. Lisyansky who performed many of the calculations used in this thesis. I wish to thank Professor Tak D. Cheung of Queensborough Community College for his valuable help in optical measurements. I would like to thank Mr. Dmitry Livdan and Mr. Walter Polkosnik for their contribution to this work. I would like to thank Mr. Ed Kuhner for his expert technical assistance.

I would like to thank Professor Melvin Lax, Dr. Ping Sheng, Professor Narciso Garcia and Professor Alexander A. Lisyansky for having served in my thesis Supervisory Committee.

I would like to take this opportunity to thank my wife Wen for her continuous support.

It is my pleasure to extend my thanks to all members of the faculty and staff at the department of physics, Queens College.

My thesis is part of the research program, studying wave propagation in random media, supported by grants of Professor Genack and Professor Garcia from the National Science Foundation and the Petroleum Research of the American Chemistry Society.

TABLE OF CONTENTS

List of Figures

CHAPTER 1 INTRODUCTION

The last decade has witnessed a revival of the study of wave propagation in random media, spurred by the analogy between classical and quantum wave propagation [1]. The particle diffusion theory, which successfully describes many features of electronic transport in weakly scattering systems, has been widely used to describe wave propagation in random media. Qualitative agreement is found between the diffusion theory and a variety of measurements, including the total transmission [2], transit time distribution [3], coherent backscattering [4-7] and intensity correlation functions versus frequency [2], time [8-11] and angle [12]. But a quantitative description of wave propagation can only be given if interfacial scattering and microparticle resonances are considered [13-24]. Providing a quantitative description of wave propagation in random media by including the influence of interfacial scattering and microparticle resonances is the goal of this thesis. It provides a description of both static and dynamic transport and makes the connection between them.

The simplest systems in which the diffusion model is appropriate are unbounded collections of randomly distributed point scatterers. In such systems the transport mean free path ℓ, which is the distance over which the direction of the wave is randomized, is the same as the scattering mean free path $\ell_s = (\sigma n)^{-1}$, where σ is the total scattering cross-section of individual scatterers, and n is the density of the scatterers. The rate of transport is given by the diffusion coefficient D, which can be calculated from the Boltzmann relation,

$$D = \frac{1}{3} v\ell . \tag{1.1}$$

where v is the velocity of wave in the medium. The intensity at an arbitrary point can be obtained by solving the diffusion equation in an infinite medium. But in practice, such an ideal system does not exist. All samples are bounded. Scatterers are often comparable in size to the wavelength. In such real systems the simple description mentioned above is not valid. The influence of interfacial scattering and microparticle resonances must be carefully examined before any quantitative description can be achieved.

To solve the diffusion equation for a bounded system, proper boundary condition must be used. Because waves are randomized inside the media, partial waves approach the boundary at all angles. Due to the total internal reflection at the sample boundaries, a large portion of intensity is reflected back to the sample. Internal reflection must therefore be incorporated into the diffusion model. Another issue which must be dealt with is the randomization processes of the coherent incident wave near the input surface. Since the diffusion model can only be applied to randomized waves, the influence of the randomization processes can only be incorporated into the diffusion model via additional assumptions. The self consistency of the diffusion model including parameters which represent wave reflection and randomization at the interfaces must be established experimentally.

If interfacial scattering is properly considered, the transport mean free path ℓ and diffusion coefficient D can be determined accurately by comparing the calculation based on the diffusion model with experiments. The next question is the connection between

ℓ and D which reflect steady state and dynamic transport properties, respectively. Eq (1.1) has been used to give such a connection. The velocity in Eq (1.1) was assumed to be the phase velocity $v_p = c/n$, where c is the speed of light and n is the average refractive index of the sample. For scatterers comparable in size to the wavelength, however, the speed of energy transport on microscopic scale may be lower than v_p due to the resonances of waves with the microstructure [18]. This question has not previously been answered in measurements in samples of uniform spheres with different filling fractions in a broad range of frequencies.

Our goal is to provide a quantitative description wave of transport and an accurate determination of ℓ and D. Important progress has been made in the last decade. Densely packed, high refractive index particles with size comparable to or larger than the wavelength are used to construct strongly scattering samples. Both interfacial scattering and microparticle resonances have strong effects in such samples. The most important discoveries in this field in the last decade are probably the observation of the coherent backscattering [4-7], the prediction and observation of the long-range correlation [25-31] and the observation of localization [32-38] in a metallic system [37]. An quantitative diffusion model and the accurate values of ℓ and D are needed in descriptions of all these phenomena.

Macroscopic matrix [26-27] and diagrammatic [28] calculations show that the correlation of the intensity fluctuations can be written as a sum of the three terms distinguished by their range of correlation, $C = C^{(1)} + C^{(2)} + C^{(3)}$. $C^{(1)}$, $C^{(2)}$ and $C^{(3)}$ correspond to the short-range, long-range and uniform correlation, respectively. The

magnitude of these three terms are of order of unity, $1/g$ and $1/g^2$ respectively, where g is the dimensionless conductance, $g \sim N\ell/L$, where N is the number of distinct transverse momentum channels, and ℓ is the transport mean free path. Here, ℓ is the key parameter to determine the degree of correlation.

Coherent backscattering has been observed as the enhancement of the intensity of the scattered light in the backscattering direction. This phenomenon was explained as the constructive interference between a Feynman path and its time-reversed counterpart [4-7]. It is believed that if scattering strength is strong enough, the same mechanism may lead to Anderson localization. In order to obtain agreement between the measured coherent backscattering cone and the theory, interfacial scattering must be considered.

Determining accurate values for ℓ and D is important in determining the proximity to the localization threshold. In the absence of microparticle resonances, spatial and spectral arguments lead to equivalent localization criteria. The Ioffe-Regel criterion in three dimension is $k\ell \leq 1$ [39]. Another spatial criterion is that the dimensionless conductance is less than unity, $g = N\ell/L \leq 1$ in localized regime [40]. These criteria require that ℓ be small to achieve localization. On the other hand, the Thouless criterion states that waves are localized if the Thouless number δ is less than unity, δ is defined as,

$$\delta = \delta E/\Delta E \tag{1.2}$$

where δE is the level width of energy states, ΔE is the average spacing between levels [41-42]. Since $\delta E \sim D/L^2$, the Thouless criterion requires a small D to localize waves. It can be shown that in the absence of microparticle resonances $g = \delta$. In the presence

of resonances, however, the question arises as to whether δ is the appropriate scaling parameter of the localization transition.

Both the scattering at boundaries and microparticle resonances are addressed in this thesis. In order to start with a simpler situation, we first study the influence of interfacial scattering in a sample in which the transport velocity is not influenced by resonances. We provide a quantitative description of wave propagation in a bounded random media utilizing the diffusion formalism with a minimum number of parameters which account for interfacial scattering. We choose a sample in which the internal reflection coefficient R is high but the effect of microparticle resonances is negligible. In this sample we test the diffusion model under the influence of interfacial scattering without involving the complexity of the microparticle resonances. The sample is a sintered alumina of refractive index n = 1.7 with solid fraction 0.97. We test the model by performing a series of independent experiments which allow us to overdetermine the interfacial parameters. We use measurements of the total transmission $T(L)$ in air and in index matching fluid to determine the values of the transport mean free path ℓ, internal reflection coefficient R and coherent penetration depth z_p, which is the length over which the coherent incident wave becomes diffusive. These parameters are also independently obtained from the measurements of the total transmission as a function of the angle of incidence $T(\theta)$. We then test the adequacy of the model and the accuracy of the determination of scattering parameters by comparing calculations using the model with these scattering parameters with measurements of the microscopic intensity distribution on the output surface of the sample. We find that the diffusion model using the

parameters obtained from the transmission measurements gives an excellent prediction for $I(\rho)$ at the output surface for $L \gg \ell$ without any adjustable parameters. We also show that the diffusion model describes angular correlation functions and coherent backscattering.

After the diffusion model has been fully tested with a variety of measurements and the techniques have been developed to determine the transport and interfacial parameters, we study a system in which microparticle resonances exist. This sample is mixtures of randomly positioned alumina spheres with refractive index n = 2.91 and hollow polypropylene spheres. Unique features of this system are the uniform particle size and controllable filling fraction. The properties of wave propagation are mapped as a function of frequency and filling fraction. Sharp resonances are observed for filling fractions up to 0.4. The transport velocity v_t is inferred from the measured ℓ and D. v_t is found to be significantly lower than the phase velocity v_p.

The diffusion model and the experiments verifying this model are described in chapter 2. In chapter 3 we describe the experimental demonstration of the relationship between angular correlation and the spatial intensity distribution. The study of microparticle resonances and transport velocity is described in chapter 4. The results are summarized in chapter 5.

CHAPTER 2 PHOTON DIFFUSION AND INTERFACIAL SCATTERING

2.1 Introduction

Diffusion theory has been widely used to describe a host of measurements, including the transit time distribution, scale dependence of total transmission, intensity correlation functions versus frequency, angle, and time and coherent backscattering [1]. Simplified assumptions regarding the interfacial scattering were used which were not verified experimentally. These assumptions are: (1) The internal reflection can be neglected; (2) the coherent incident wave is randomized in a distance ℓ. Both assumptions are not appropriate in many cases and may cause serious problems in a quantitative description. For example, the total transmission is perhaps the most direct way to test the diffusion model and determine the transport mean free path ℓ. The internal reflection may dramatically enhance total transmission [23]. Internal reflection also lengthens the average path length of propagation in the medium [13,17]. In thin samples, this may affect the transit time distribution and intensity correlation functions.

As a consequence of these unsubstantiated assumptions, discrepancies were found in the fit of diffusion theory to measurements. For example, the measured functional form of the angular intensity correlation function was found substantially narrower than the calculated results [12]. The source of this discrepancy was latter attributed to the internal reflection [14,16,20]. Agreement is always found between the theory and a single measurement, such as the total transmission, coherent backscattering or the transit time distribution using the transport mean free path ℓ or diffusion coefficient D as a fitting parameter. However, inconsistencies were found when results from independent

measurements were compared. Two systems, which are titania spheres embedded in a polystyrene matrix and titania spheres suspended in air, have been extensively studied in both static and dynamic measurements by Genack *et al* [2-3] and Lagendijk *et al* [43]. The diffusion coefficient D obtained from the dynamic measurements, such as the transit time distribution or correlation function with frequency shift, was found significantly smaller than the value inferred from the relation $D = v_p \ell/3$, using the value of ℓ obtained from the measurements of the total transmission or the coherent backscattering.

Various authors have considered the influence of interfacial scattering. It was first proposed by Lagendijk *et al* [13] that the internal reflection must be considered in diffusion model. They developed a formalism for the Green's function that describes diffusive propagation in the presence of internal reflection. They discussed the influence of internal reflection on the coherent backscattering cone and the transit time distribution. Freund *et al* [14] have largely removed the discrepancy between the measurements and the calculation of the angular correlation functions by treating internal reflection coefficient as a fitting parameter. Garcia *et al* [17] considered the influence of internal reflection on the total transmission. They found the total transmission can be expressed solely in terms of boundary properties. Mackintosh *et al* [15] studied wave propagation over short paths near the input surface. They found that the randomization processes depend on the scattering form factor of the scatterers.

In this chapter, we describe optical measurements of the total transmission and reflection as a function of the sample thickness $T(L)$ and $R(L)$, and of the angle of incidence $T(\theta)$, surface intensity profiles $I(\rho)$, coherent backscattering cone $I_c(\theta)$ and the

transit time distribution $T(t)$. The results of $T(L)$ allow us to obtain accurate values for the extrapolation length,

$$z_b = \frac{2\ell}{3}\frac{1+R}{1-R}, \tag{2.1}$$

and the coherent penetration length z_p. ℓ is obtained from the value of z_b measured for a sample immersed in an index matching fluid in which case $R = 0$. R for the sample/air interface is obtained from the value of z_b measured for the sample in air. The same sets of parameters are also obtained from measurements of the transmission as a function of the incident angle $T(\theta)$. We then critically test the diffusion model and accuracy of the measured transport parameters. We measured microscopic intensity distribution on the sample output surface $I(\rho)$ for the sample in air and in the index matching fluid. Excellent agreements is found between the measurements and the calculated $I(\rho)$ using the measured z_p, z_b and ℓ in the diffusion model without any adjustable parameters. We find the range of validity of the diffusion model by comparing the diffusion model and the measurements of $I(\rho)$ for the sample thickness comparable to ℓ and in reflection. We also observe the transition from ballistic to diffusive transport. We infer the value of the diffusion coefficient D from $D = v\ell/3$ assuming v is the phase velocity $v_p = c/n$, where c is the speed of light and n is the average refractive index of the sample. Using the values of D, z_p and z_b we calculate the transit time distribution $T(t)$. Good agreement is found with the measurement.

2.2 Review of Diffusion Model

Different approaches can be taken to treat the randomization of the wave as it enters the sample and the reflection of the wave reaching the surface from the interior of the sample. In this section, we review a diffusion model developed by Lisyansky *et al* [44]. Three interfacial coupling parameters are used to account for the effect of interfacial scattering in this model. These parameters are the coherent penetration depth z_p from the surface at which the incident wave is effectively randomized, and the extrapolation length z_b beyond the input and output boundaries at which the intensity inside the sample extrapolates to zero. Surface intensity profiles and total transmission are obtained by solving diffusion equation which incorporates with these parameters.

Inside a sample of an absorbing random media, in the weakly scattering regime in which $k\ell \gg 1$, where k is magnitude of the photon wave vector and ℓ is the transport mean free path, the average intensity $I(\boldsymbol{r})$ obeys the diffusion equation,

$$\nabla^2 I(\boldsymbol{r}) - \alpha^2 I(\boldsymbol{r}) = -\frac{1}{D} Q(\boldsymbol{r}). \tag{2.2}$$

where $D = v\ell/3$ is the diffusion coefficient, v is the speed of the light in the medium, α is an absorption coefficient, $\alpha^2 = 3/\ell\ell_a$, ℓ_a is an absorption length, and $Q(\boldsymbol{r})$ is a source function. A slab of the random medium of infinite extent in the x, y directions to be positioned along z axis between $0 < z < L$ is considered. The reflection coefficients are R_1 and R_2, respectively, at input and output boundaries. The coherent radiation incident on the sample is assumed to become randomized within a distance z_p, which is of the

order of the transport mean free path. The incoming coherent flux is replaced by a source of diffusive radiation at the plane $z = z_p$ with a strength equal to the incident flux.

Since an assumption is made that there is no incoming flux through the boundaries, the only flux on the boundary towards the interior of the slab is the reflected part of the flux in the outgoing direction. This gives boundary conditions in the form,

$$J_+(x,y,z=0^+) = -R_1 J_-(x,y,z=0^+); \tag{2.3a}$$

$$J_-(x,y,z=L^-) = -R_2(J_+(x,y,z=L^-), \tag{2.3b}$$

where J_+ and J_- are diffusive fluxes in the positive and negative z-directions respectively. Using the relation between the diffusive flux and the intensity of photons,

$$J_\pm(\mathbf{r}) = \frac{I(\mathbf{r})\, v}{4} \mp \frac{D}{2}\frac{\partial I(\mathbf{r})}{\partial z}, \tag{2.4}$$

the boundary conditions for Eq. (2.2) can be rewritten as,

$$\left[\frac{1}{z_1} I(\mathbf{r}) - \frac{d}{dz} I(\mathbf{r})\right]_{z=0^+} = 0; \left[\frac{1}{z_2} I(\mathbf{r}) + \frac{d}{dz} I(\mathbf{r})\right]_{z=L^-} = 0, \tag{2.5}$$

where,

$$z_{1,2} = \frac{2}{3}\ell \frac{1 + R_{1,2}}{1 - R_{1,2}}. \tag{2.6}$$

$R_{1,2}$ represents is the internal reflectivity for the input and output surfaces respectively. In the case of a totally reflective boundaries, Eq. (2.5) gives the condition that the normal component of the total flux through the boundary is zero. In the case that $R_{1,2} = 0$, Eq. (2.5) corresponds to the perfectly absorbing boundaries.

Solving Eq. (2.2) with boundary conditions given by Eq. (2.5) we obtain the intensity distribution along input and output surfaces in a cylindrical coordinate,

$$I(\rho,L) = p\int_0^\infty \frac{\lambda\, d\lambda\, J_0(\lambda\,\rho)[D_1(\lambda)\sinh(k(\lambda)z_p)+\cosh(k(\lambda)z_p)]}{k(\lambda)[1+D_1(\lambda)D_2(\lambda)]\sinh(k(\lambda)L)+[D_1(\lambda)+D_2(\lambda)]\cosh(k(\lambda)L)}. \tag{2.7}$$

$$I(\rho,0) = p\int_0^\infty \frac{\lambda\, d\lambda\, J_0(\lambda\,\rho)[D_1(\lambda)\sinh(k(\lambda)(z_p+L))+\cosh(k(\lambda)(z_p+L))]}{k(\lambda)[1+D_1(\lambda)D_2(\lambda)]\sinh(k(\lambda)L)+[D_1(\lambda)+D_2(\lambda)]\cosh(k(\lambda)L)}. \tag{2.8}$$

Here $J_0(x)$ is the Bessel's function of zero order, $k^2(\lambda) = \lambda^2 + \alpha^2$ and $D_{1,2} = k(\lambda)z_{1,2}$.

The total normalized transmission through the slab can be expressed as,

$$T(L) = \frac{\int_0^\infty \rho\, d\rho\, J_{transmitted}(\rho,L)}{J_{incident}} = \frac{1-R_2}{q}\int_0^\infty \rho\, d\rho\, J_+(\rho,L^-). \tag{2.9}$$

Integrating the transmitted flux corresponding to the intensity distribution given by Eq. (2.9) one obtains the following expression for total normalized transmission through the slab,

$$T(L) = \frac{\sinh(\alpha z_p) + \alpha z_1 \cosh(\alpha z_p)}{(\alpha^2 z_1 z_2 + 1)\sinh(\alpha L) + \alpha (z_1 + z_2)\cosh(\alpha L)}. \tag{2.10}$$

If the notation,

$$z_{b1,2} = \frac{1}{2\alpha} \ln\left(\frac{1 + \alpha z_{1,2}}{1 - \alpha z_{1,2}}\right), \tag{2.11}$$

is introduced, Eq. (2.10) can be rewritten as,

$$T(L) = \frac{1}{\alpha z_{b2}} \frac{\sinh[\alpha(z_p + z_{b1})] \sinh(\alpha z_{b2})}{\sinh[\alpha(L + z_{b1} + z_{b2})]}. \tag{2.12}$$

In the case of a plane wave incident on the slab values z_{bi} given by Eq. (2.12) define the extrapolation lengths on which intensity extrapolated beyond the slab hits zero. These lengths exist only when reflection coefficients $R_{1,2}$ are smaller than $R_c = (1-2\ell/3)/(1+2\ell/3)$. In the case of point source, however, z_{bi} are not extrapolation lengths, an *extrapolation surface* $z_{b0}(\rho)$ can be defined by the equation $I(\rho,z) = 0$. When absorption is weak αL, $\alpha z_{bi} \ll 1$ Eq. (2.12) reduces to

$$T(L) = \frac{z_p + z_{b1}}{L + z_{b1} + z_{b2}}. \tag{2.13}$$

2.3 Samples and Experiments

2.3.a Samples

In order to concentrate on the problem of interfacial scattering without the additional problems of microparticle resonances and rough surface, we chose a optically polished sample in which the internal reflection coefficient is high but in which the effect of sphere resonances is negligible. The sample is 99.7% purity polycrystalline alumina with 0.97 solid fraction provided by Valley Design Corporation. At an incident angle of 11.0 degree, the specular reflection coefficient for the perpendicular polarization is measured to be 7.2%. Using the Fresnel's law we find the effective refractive index 1.70 for the sample which is close to the index of 1.76 of pure alumina. Random grains of average size about 2 μm are shown in the Electron-micrographs of the material as shown in Fig. 2.1. The random voids with size much smaller than the wavelength or the grain boundaries serve as scattering centers, hence sphere resonances are not expected in this sample. Also the transport mean free path is much larger than the wavelength in this sample, indicating a low scatterer density, hence influence of resonances with scatterers is small. The high solid fraction of the sample also provides the advantage of matching the refractive index of the sample by immersing it in the fluid without wetting the sample.

Two wedges of 0.0182 and 0.0091 rad are fabricated by polishing alumina slabs. The thickness of the wedges varies from 40 μm to 640 μm and 15 μm to 200 μm respectively. The wedge geometry provides us the convenience to make measurements

at various sample thickness. The thinner wedge is used to study the transition from ballistic to diffusive transport. Because we use focused incident beam in the measurements, photons spread in the transverse direction in region comparable in size to the thickness of the sample. The variation of the wedge thickness in such small area is negligible.

2.3.b Measurements of Transmission and Reflection

The experimental setup for measuring the total transmission is shown schematically in Fig. 2.2. A 3 mW *He-Ne* laser beam is expanded, collimated and then focused to the sample surface by an *f*/1.4, 5.5 cm focal length Nikon lens. We use an integrating sphere and photomultiplier tube assembly as detector to measure the incident and transmitted flux. The ratio of the transmitted to incident flux gives the transmission coefficient. The incident flux is the part of the incident beam which is not specularly reflected from the input surface. The sample is mounted on a computer-controlled translation stage. We obtain the scale dependence of the total transmission $T(L)$ by detecting the flux captured by an integrating sphere as the wedge is translated. A quartz cell is used when the sample is immersed in an index matching fluid of refractive index 1.70. In this case only relative transmission can be measured because the transmitted light cannot be fully captured by the integrating sphere. The total reflected flux is measured using the same apparatus with the laser beam incident in the opposite port of the integrating sphere. The diffusive reflection is the difference between the total

reflected flux and the specularly reflected flux. The ratio of the diffusive reflection to the incident flux that is not specularly reflected gives the reflection coefficient. We measure the total transmission as a function of the incident angle $T(\theta)$ by rotating the sample-detector assembly with respect to the incident beam.

2.3.c Measurements of Surface Intensity Profiles

The experimental setup for the measurements of surface intensity profiles is shown schematically in Fig. 2.3. We focus the incident laser beam to a 5 μm spot. The intensity profile at the sample surfaces versus transverse coordinate $I(\rho)$ is imaged near the normal to the surface with an *f*/1.4, 5.5 cm focal length Nikon lens. The image is magnified 30 times. The transverse profile through the center of the image of the output intensity distribution is recorded by scanning a photomultiplier tube with an affixed 20 μm aperture in the image plane 175 cm from the sample. Large fluctuations are observed in $I(\rho)$ for a fixed sample. The results reported for $I(\rho)$ are incoherent averages of intensity patterns obtained by scanning the sample in the sample plane at fixed thickness as the data is collected.

2.3.d Measurements of Transit Time Distribution

Measurements of the temporal distribution of a transmitted optical pulse are made using 628 nm pulses derived from a cavity dumped dye laser which is synchronously

pumped by a frequency-doubled mode-locked *YAG* laser. The width of laser pulses is 1 ps. The signal is detected using a 12 μm two stage Hamamatsu microchannel plate photomultiplier. The time distribution is determined by time-correlated single photon counting.

2.4 Results and Discussion

2.4.a Total Transmission and Reflection versus Sample Thickness

We measure the total transmission $T(L)$ and the total reflection $R(L)$ versus sample thickness under the same experimental conditions [23]. The results are shown in Fig. 2.4. For all thickness the sum of $T(L)$ and $R(L)$ is unity within 1% experimental error. The integrating sphere detecting system may respond differently to the incident flux, which is essentially a parallel beam, and to the transmitted flux, which enter the sphere in a range of angles. This is because that the amount of photons which are absorbed by the interior of the integrating sphere or escape through the input port and the gap between the sample and the integrating sphere may be different for light entering the integrating sphere at different angles. From measurements of the variation in intensity readings with the angle at which laser beam enters the integrating sphere we estimate that relative transmission is uncertain to 0.5%. Therefore we conclude that in this sample the absorption is negligible. Eq. (2.13) can be used in this case. If we assume that the angular dependence of the reflected and transmitted flux are the same, the extrapolation length at the input surfaces is the same as the output surface,

$$z_{b1} = z_{b2} = \frac{2\ell}{3}\frac{1+R}{1-R}. \tag{2.14}$$

Measurements which support this assumption will be discussed later. In the following text, we replace both z_{b1} and z_{b2} with z_b. Eq. (2.13) can then be further reduced to,

$$T(L) = \frac{z_b + z_p}{L + 2z_b}. \tag{2.15}$$

$T(L)$ is measured for thicknesses L from 40 μm to 640 μm. A nonlinear least-square fit of Eq. (2.15) to the data was attempted in this thickness range. The fit appear to have failed because for L < 100 μm, the diffusion model may not be valid since the sample thickness is not much larger than the transport mean free path. An excellent fit of Eq (2.15) to the data was obtained when only the data for L > 100 μm are used. We fit the expression $R(L) = 1 - T(L)$ to the total reflection data from L = 100 μm to 640 μm. The fitting results for $T(L)$ and $R(L)$ are shown in Fig. 2.4. z_p = 24.8 μm and z_b = 190.9 μm are determined from the fit. The standard deviation σ for z_p and z_b are 0.1 μm and 0.3 μm respectively.

Can we infer the transport mean free path ℓ from these two parameters? In our model, z_p is the distance over which the waves are randomized *near the boundary*. The transport mean free path, which is the distance over which waves randomize *in the bulk* can be different than z_p. z_b is related to ℓ as in Eq. (2.14). But without knowing the internal reflectivity R, we can not infer ℓ from z_b.

The circumstance in which R is most accurately known is where internal reflection is eliminated so that $R = 0$. This is achieved by immersing the sample in index matching fluid which has the same refractive index as the sample, n = 1.70. The specularly reflected beam disappears entirely when we put the sample in the index matching fluid showing a perfect index matching between the sample and the matching fluid. Only

relative transmission can be measured as discussed in section 2.2.b for the sample immersed in an index matching fluid. This implied that only z_b can be obtained from the fit of diffusion theory to the data. $T(L)$ measured for the sample in the index matching fluid is dramatically different than in air. We plot the inverse of $T(L)$ versus L for the data in the fluid and air in Fig. 2.5. A large difference is found between slopes of these curves. $T(L)$ in the fluid decreases about 6 time faster than in air. This implies that at the same thickness, the total transmitted intensity in the presence of internal reflection is higher than the case in which $R = 0$. This result is consistent with the effect that the internal reflection enhances the total transmission. Because there are more photons near the input interface than the output, more photons are internally reflected at the input surface and reenter the flux propagating to the output surface, hence the total transmission is enhanced.

Taking the inverse of Eq. (2.15) we obtain,

$$T^{-1}(L) = \frac{1}{(z_p+z_b)}L + \frac{2\,z_b}{z_p + z_b}. \qquad (2.16)$$

z_b can be accurately determined from the x-intercept of $T^{-1}(L)$. As shown in Fig. 2b, for $L > 100$ μm $T^{-1}(L)$ both in air and in the index matching fluid are a straight line following the prediction of Eq. (2.16). From the x-intercept of the linear fit of $T^{-1}(L)$ to the data we find $z_b = 190.9$ μm again for the sample in air, and $z_b = 22.3$ μm for the sample immersed in the index matching fluid, with standard deviation σ 0.1 μm. Diffusion theory gives $z_b = 2\ell/3$ for the case in which $R = 0$, whereas the transport theory gives the Milne result $z_b = 0.7104\ell$ [45]. Using the Milne result, we find $\ell = 31.4 \pm 1.5$

μm. To assure the accuracy of these parameters, we examined the systematic error of the measurements. As mentioned above, measurements of total transmission is uncertain to 0.5%. In addition the uncertainties of 1 μm in the thickness of thinnest part of the sample results in uncertainties of 1 μm in z_p and of 1.5 μm in z_b. Using the value of ℓ and the value of z_b in air in the expression for z_b, we obtain R=0.81 for the sample/air interface for diffusing waves. Using the value of z_b to calculate the diffusive angular distribution at the surface gives an angle averaged Fresnel reflection coefficient of 0.76 which is consistent with the measured value of R.

Several conclusions can be made from the above discussion. (1) The influence of internal reflection on the measurements of the total transmission cannot be neglected even at $L \gg z_b$. On the other hand, internal reflection can be neglected at large thickness for measurements which depend on the path length distribution, such as the transit time distribution and intensity correlation functions. (2) The transport mean free path cannot be obtained from a single measurement of the total transmission in the presence of internal reflection. ℓ can be inferred from z_b only if the internal reflectivity is known. (3) z_p is not necessarily equal to ℓ.

In the study presented above we observed the dramatic influence of internal reflection on the total transmission $T(L)$ and obtained agreement with a diffusion model which incorporates interfacial scattering. The only previous calculation of $T(L)$ in the literature which includes the internal reflection is a work by Freund *et al.* They used a multiple-passage argument instead of diffusion theory to treat internal reflection. They expressed the total transmission in the presence of internal reflection in terms of the

internal reflection coefficient R and the total transmission in the absence of the internal reflection. Good agreement between their calculation and our data is shown in Fig. 2.6.

Finally we go back to our assumption that the extrapolation length at the input surface z_{b1} and output surface z_{b2} are equal. Taking the inverse of Eq. (2.13) we find,

$$T^{-1}(L) = \frac{L + z_{b1} + z_{b2}}{z_{b1} + z_p}. \tag{2.17}$$

The x-intercept of $T^{-1}(L)$ is equal to $z_{b1} + z_{b2}$. We measure transmission for two cases in which only the input or the output surfaces is index-matched . The results are shown in Fig. 2.7. Since the x-intercepts of $T^{-1}(L)$ for these two cases are equal within experimental error, we obtain $z_{b1}^{(fluid)} + z_{b2}^{(air)} = z_{b1}^{(air)} + z_{b2}^{(fluid)}$.

2.4.b Total Transmission versus Angle of Incidence

The study of the randomization processes of the incident wave are relevant to propagation in any random medium in which questions of the coupling between media exist, as they do, for example, in connection with the contact resistance or impedance mismatch in electronic or acoustic systems respectively. We attempt to capture the influence these complicated physical processes via a single parameter z_p. It is of interest to test whether this single parameter catches the underlying physics when the illumination of the sample are changed. The measurements of $T(L)$ described above were made under the normal incidence, the angle of incidence is zero, $\theta = 0$. If $\theta > 0$, the randomization processes will occur within smaller distance from the input surface. Within the

framework of the present diffusion model, we expect that the longitudinal penetration depth decreases with θ and varies as $z_p\cos\theta_r$, where θ_r is the angle of refraction in the random medium. Replacing z_p with $z_p\cos\theta_r$ in Eq. (2.15) gives,

$$T(\theta) = \frac{z_p\cos\theta_r + z_b}{L + z_b}. \tag{2.18}$$

From Eq. (2.18), we notice that $T(\theta)$ is sensitive to θ only when z_p is comparable to z_b. To achieve the condition $z_p \sim z_b$, we match the index of the input surface by attaching the sample to a half cylinder glass cell which contains the matching fluid. In this case $\theta = \theta_r$. The measurements of $T(\theta)$ for the sample in which the input surface is index matched and the output is in air is shown in Fig. 2.8. A remarkable agreement is found between the measurements and the calculation of Eq. (2.18) using the values of z_p and z_b for the sample in the index matching fluid and in air. This confirms the accuracy of z_p and z_b obtained from measurements of $T(L)$ and shows that z_p in our diffusion model capture physical reality of the randomization processes of the incident wave with regard to transmission measurements. The result also shows that the interfacial scattering parameters can be obtained independently from this simple measurement.

2.4.c Surface Intensity Profiles

We study surface intensity profiles for two purposes. First, We intend to perform a detailed experiment to critically test our diffusion model. In the previous two sections, we have described the measurements of the total transmitted intensity. Using z_p, z_b and

ℓ determined from these measurements in the diffusion model, we can calculate the diffusion intensity propagator $P(\rho)$ without any adjustable parameter. $P(\rho)$ gives the probability that a photon that enters the sample at the origin on the input surface will exit at a transverse distance ρ along the output surface. A stringent test of the diffusion model is to compare the measurements of the microscopic intensity distribution along the sample surfaces $I(\rho)$ for a point source input with $P(\rho)$. Second, $P(\rho)$ on the input and output surfaces is the underlying particle aspect of the coherent backscattering $I_c(\theta)$ [7] and the angular correlation function $C(\delta\theta)$ [12]. Although $I_c(\theta)$ and $C(\delta\theta)$ have been under intensive study in recent years, the corresponding $I(\rho)$ has not been measured previously [46]. We intend to establish the diffusion formalism for $I(\rho)$ and then to utilize this formalism to predict $I_c(\theta)$ and $C(\delta\theta)$.

The laser beam is focused to a 5 μm spot. The spot is much less than the transport mean free path ℓ = 31.4 μm. We measured $I(\rho)$ on the output surface for the sample in air and the index matching fluid at different thicknesses from 89 to 640 μm. Measurements of $I(\rho)$ for the sample in air are shown in Fig. 2.9 [23]. $I(\rho)$ is normalized by the value at the center of the distribution. Intensity measurements are shown along a line going through the center of the distribution which is taken as the origin in the figure. The solid lines in Fig. 2.9 are calculated from Eq. (2.7). For L > 200 μm we find excellent agreements between the measurements and calculations based on the diffusion model using the transport parameters z_p, z_b and ℓ. The agreement is particularly impressive because the calculation is done without any adjustable parameters. $I(\rho)$ measured at L = 280 μm for the sample in air and in the index matching fluid are shown

in Fig. 2.10. The excellent agreement with the calculation shows that the diffusion model accurately describes the surface intensity profiles in the presence of internal reflection. Measurements of $I(\rho)$ in air are broader than in the index matching fluid. This is because the internal reflection gives rise to extra length to the propagation path, hence more photons exit the sample at larger transverse distance.

2.4.d Validity of Diffusion Model and Ballistic Transport

We have discussed in section 2.4.a that the diffusion model does not describe the total transmission for $L < 100$ μm. In this section, we discuss a test of the range of validity of the diffusion model and a study of ballistic scattering.

It is generally accepted that the diffusion model is valid only at length scale much larger than the transport mean free path ℓ [1]. Over length scale comparable to or less then ℓ, wave transport is ballistic in nature [15]. Here we study the transition from ballistic to diffusive transport. The diffusion model can be fit to the microwave transmission measurements even for the sample thickness slightly less than ℓ [29]. But measurements of the transit time distribution showed that the diffusion model is not valid for small thickness until $L > 10\ell$ [47]. The validity of the diffusion model in reflection is also an important issue. The diffusion theory has been widely used to calculate the angular, temporal and frequency correlation functions in reflection as well as the coherent backscattering cone. Because the reflected light contains the contribution of short paths of several the transport mean free paths, the diffusion model may not be adequate for a

quantitative description. We have shown in the previous sections that the diffusion model predicts accurately a host of measurements in transmission for thick samples, and have measured propagation parameters. Using these parameters in our diffusion model, we calculate the surface intensity profiles in reflection. We also calculate the coherent backscattering cone from the Fourier transform of the intensity profiles in reflection. These allow us to independently test whether these calculations of the diffusion model describe the measurements.

As discussed in section 2.4.c the diffusion model does not fit the total transmission data for sample thickness from 40 to 100 μm. We use the thinner wedge of the same alumina sample with thickness varying from 15 to 200 μm to study ballistic transport. The thin sample hinders only part of the coherent incident beam. The unscattered waves still propagate along the original direction. The scattering theory predicts that the intensity remains in the transmitted coherent beam decreases exponentially with the sample thickness,

$$T_c(L) \propto exp(-L/\ell_s). \tag{2.19}$$

For small sample thickness, the coherent beam is highly visible in the center of the speckle pattern. With increasing sample thickness, the coherent spot becomes dimmer and finally disappears. We measure the intensity in the coherent beam in transmission as a function of the sample thickness. Fig. 2.11 shows that the measured intensity decreases exponentially with the sample thickness as predicted by the scattering theory. The scattering mean free path ℓ_s is obtained from the slope of the exponential decay, ℓ_s = 9.5 μm. ℓ_s and the transport mean free path ℓ are related by the relation,

$$\ell = \frac{\ell_s}{1 - \langle \cos\theta \rangle}, \tag{2.20}$$

here $\langle \cos\theta \rangle$ is the average of the cosine of the scattering angle taken over the differential cross-section $\sigma(\theta)$. This gives $\langle \cos\theta \rangle \approx 2/3$, which is a measure of anisotropy of scattering from individual scatterers in the sample.

For $L \leq 200$ μm the measurements of $I(\rho)$ made with light collected in an angular range from -10 to 10 degree is substantially narrower than the calculation as shown in Fig. 2.12. The difference between the measured $I(\rho)$ and the diffusion model increases with a decreasing sample thickness. We measure the surface intensity profiles at L = 89 μm using a polarized incident laser beam. Intensity profiles are measured in polarization component perpendicular to the incident beam and in unpolarized light. It is shown in Fig. 2.13 that the halfwidth of the measured $I(\rho)$ for both unpolarized light and perpendicular polarization is much less than the calculated width. The measured $I(\rho)$ for unpolarized light is substantially narrower than the perpendicular polarization. This difference cannot be explained within the frame of diffusion theory. In contrast, $T(L)$ is seen in Fig. 2.4 to conform to the predictions of the diffusion model for $L \geq 100$ μm. The reason for this difference is that $I(\rho)$ is measured using a lens to collect light in the forward direction. Light that has not been fully randomized is more sharply peaked in the forward direction and has a narrower distribution in the transverse direction. This light is nearly normal to the output surface and consequently has a larger Fresnel transmission coefficient at the output surface. It, therefore, makes a proportionately greater contribution to the measured $I(\rho)$ than light that has been more completely

randomized. On the other hand, the total transmission in samples in which L is several times larger than ℓ is relatively insensitive to the angular distribution of light at the output surface. Though the transmission coefficient depends strongly upon the orientation at which the light strike the output surface, the probability is high that photons which have reached the output surface will eventually emerge from that surface, even if only after several reflection. We attempted to measure $I(\rho)$ at large angles by changing the angle of the imaging lens with respect to the normal of the sample from 0 to 20 degrees. No significant difference in $I(\rho)$ measured in this angular range is observed. Measurements of $I(\rho)$ at larger angles are not feasible because the intensity profiles may be distorted.

We find significant discrepancies between the calculations and the measurements of the surface intensity profiles in reflection. The experimental arrangement for the measurement of intensity profiles in reflection is similar to that used in transmission, except the imaging lens is placed in the front of the input surface of the sample at an angle of 20 degrees with respect to the normal of the surface to avoid the specular reflection. Fig. 2.14 shows the surface intensity profiles in reflection for parallel and perpendicular polarizations as well as the prediction of diffusion model using the parameters found in section 2.4.a in measurements of total transmission. The intensity profile for the parallel polarization is substantially narrower than for the perpendicular polarization. This difference in different polarizations cannot be described within the framework of the diffusion theory. In transmission, appreciable difference in the intensity profiles for different polarizations was only observed at thickness for which the diffusion model failed to accurately describe $I(\rho)$. Moreover, the intensity profiles for both

polarizations are narrower than the prediction of the diffusion model.

$$I_c(\theta) = \int P(\rho)\exp(-i\frac{2\pi}{\lambda}\theta\rho)d\rho. \tag{2.21}$$

The coherent backscattering cone $I_c(\theta)$ is found to be the Fourier transform of the intensity propagator $P(\rho)$ [7]. We measure $I_c(\theta)$ using the standard experimental setup described in literature. As shown in Fig. 2.15, the measured $I_c(\theta)$ is in good agreement with the Fourier transform of the intensity propagator $P(\rho)$. This shows although the diffusion model does not describe $I(\rho)$ in reflection, it does describe $I_c(\theta)$. This is because the measured $I(\rho)$ contains the contribution of short paths, including single-scattering process, which cannot be described by diffusion theory. On the other hand, there is no contribution from single-scattering to the coherent backscattering cone [48].

2.4.e The transit time distribution

In preceding sections, we have discussed measurements of static transport. In this section, we describe time-resolved measurements. Because it is expected that the influence of microparticle resonances is negligible in the alumina sample, we intent to make connection between static and time-resolved measurements using the value of the phase velocity in the Boltzmann relation $D = \frac{1}{3}v\ell$.

The distribution of photon transit time $T(t)$ is calculated by solving the diffusion equation,

$$\frac{\partial I(r,t)}{\partial t} - D\nabla^2 I(r,t) + \frac{1}{\tau_a} I(r,t) = Q(r,t), \tag{2.22}$$

with the boundary condition that the photon density is zero at the distance z_b outside the sample surface. This can be simulated by the method of images in which positive sources which are delta functions in space and time are placed at $z = z_p + 2Ln$ and equal and negative sources are placed at $z = -z_p + 2Ln$, where n ranges over all the integers. This gives,

$$T(t;L) = \frac{\exp(-\frac{t}{\tau_a})}{(4\pi Dt)^{1/2}} \sum [\exp(-\frac{|(2n-1)(L+2z_b)-2(z_p+z_b)|^2}{4Dt}) - \exp(-\frac{|(2n-1)(L+2z_b)|^2}{4Dt})]. \tag{2.23}$$

In the summation, n ranges over all the integers, τ_a is the absorption time. We measure the transit time distribution using correlated single photon counting technique described in section 2.2.d for the alumina wedge at L = 640 μm. The triangles in Fig. 2.16 are the measured instrument response to the incident pulse, the dots are the measured transmitted pulse. The line through the dots is the reconvolution of the measured instrument response to the incident pulses with the calculated $T(t)$ from Eq. (2.23). Four parameters, z_p, z_b, D and τ_a are used to calculate $T(t)$. We use the values of z_b = 190.9 μm and z_p = 24.8 μm determined from the total transmission measurements in section 2.4.a. Because of the absence of spherical scatterers and low scatterer density, the influence of microparticle resonances is negligible. We use the value of phase velocity $v_p = c/n$, where c is the

speed of light and $n = 1.70$ is the refractive index of alumina, and the measured transport mean free path $\ell = 31.4$ μm to calculate $D = \frac{1}{3}v\ell$. Results of total transmission and surface intensity profiles indicate absorption is negligible for $L < 640$ μm, this implies $L_a > 640$ μm. We use different values of L_a to calculate $\tau_a = L_a^2/D$. We find that $L_a \approx 700$ μm gives the best fit with the data. It is shown in Fig. 2.16 that the measured $T(t)$ is well described by Eq. (2.23) using the transport parameters obtained from measurements of static transport. This verifies that the value of phase velocity can be used in the Boltzmann relation to connect D and ℓ in the absence of spherical scatterers and when the scatterer density is low.

2.5 Conclusion

In conclusion, we have demonstrated that diffusion theory incorporating interfacial scattering can quantitatively describe a broad array of independent optical measurements of integrated and local intensity. These results allow us to determine the range of validity of diffusion theory and accurately determine ℓ, R and z_p for the first time without making any sample-specific assumptions.

CHAPTER 3 CORRELATION IN LASER SPECKLE

3.1 Introduction

We have shown in chapter 2 that the diffusion model quantitatively describes average transport. In this chapter, we apply this model to describe the wave nature of propagation. We confirm a general expression for angular correlation functions with arbitrary shift in incident and scattered wave vectors by measurements of angular correlation within the static speckle pattern $C(\Delta\theta)$ and of the "memory effect" $C(\delta\theta)$. We demonstrate that $C(\Delta\theta)$ is given by Fourier transforms of the intensity distribution on the output surface $I(\rho)$, and $C(\delta\theta)$ is given by Fourier transforms of the intensity propagator between the input and output surfaces $P(\rho)$. Measurements of $C(\Delta\theta)$ and $C(\delta\theta)$ in samples with and without internal reflection are in excellent agreement with the diffusion model without adjustable parameters.

Large intensity fluctuations as a function of the spatial, spectral or temporal parameters of the incident or scattered wave display the nature of multiply scattered waves in random media. Perhaps the most dramatic manifestation of intensity fluctuation is the grainy appearance of the scattered laser light known as laser speckle. Laser speckle has been studied extensively since it is first observed more than thirty years ago [49]. In conventional study of laser speckle, a fundamental assumption is that intensity of scattered light at different points in a random medium or from a rough surface is totally uncorrelated. Recently, however, it is predicted and observed that scattered waves in different points in random media are correlated [25-31]. As a result, transmitted waves in different speckle spots are not totally random. Intensity correlation in transmitted light

has generally been considered in a waveguide geometry between the $N = Ak^2/2\pi$ distinct transverse momentum and polarization channels of a waveguide of area A, where k is the magnitude of the wave vector. The transmission coefficient from channel a on the left of the disordered region to channel b on the right is denoted as T_{ba}. Macroscopic matrix and diagrammatic calculations show that the correlation matrix $C_{ab,a'b'} = <\delta T_{ba} \delta T_{b'a'}>$ of fractional fluctuations, in the transmission coefficients from their ensemble average values $\delta T_{ba} = (T_{ba} - \langle T_{ba} \rangle) / \langle T_{ba} \rangle$ can then be written as a sum of three terms distinguished by the range of correlation between modes [26-28],

$$C_{ab,a'b'} = C^{(1)}_{ab,a'b'} + C^{(2)}_{ab,a'b'} + C^{(3)}_{ab,a'b'}. \tag{3.1}$$

When the sample length L within the waveguide is much greater than its width $W \sim A^{1/2}$, the ensemble average of the intensity distribution in the transverse coordinate has the width W independent of the distribution of the incident excitation. The correlation matrix, may then be written as [26-27],

$$\delta_{aa'} \delta_{bb'} + A_2 (\delta_{aa'} + \delta_{bb'}) + A_3 . \tag{3.2}$$

The coefficients A_1, A_2, and A_3 are of order 1, $1/g$ and $1/g^2$ respectively, where g is the dimensionless conductance, $g \sim N\ell/L$, where ℓ is the photon transport mean free path.

The first term arises in the field factorization approximation, $C^{(1)}_{ab,a'b'} = |I_{ab,a'b'}|$,

where $I_{ab,a'b'} = \langle \boldsymbol{E}_{ab} \cdot \boldsymbol{E}^{*}_{a'b'} \rangle$, and <...> denotes an average over an ensemble of sample

configurations. This term dominates intensity fluctuations. The Kronecker delta in the

C_1 term represents the sharp cutoff of correlation between different transverse momentum channels with a correlation wave vector of $\delta k \sim 1/W$. The C_2 term gives rise to long-range correlation and dominates transmission fluctuations whereas the C_3 term is the source of universal conductance fluctuations. Only the lowest order C_1 term will be discussed here.

For a slab geometry in which the width of the output intensity distribution $\delta\rho_b$ is much greater than the slab thickness, $\delta\rho_b \gg L$, Feng *et al* found the expression for the C_1 term [28],

$$C^{(1)}_{k_a k_b k_a' k_b'} = A_1 \delta_{\Delta k_a, \Delta k_b} F_1(\Delta k_a L), \tag{3.3}$$

where,

$$F_1(x) = x^2/\sinh^2 x. \tag{3.4}$$

The range of the correlation function $F_1(\Delta k_a L)$ for identical shifts in the incident and scattered wave vectors is $\delta k \sim 1/L$. On the other hand, the Kronecker delta in shifts Δk_a and Δk_b of the incident and scattered wave vectors, respectively, reflects the very short range correlation when either the incident or scattered wave vector is changed separately if $\delta\rho_b$ is very large. However, the range of this short range correlation function increases as $\delta\rho_b$ decreases. If $\delta\rho_b$ is comparable to L, as it is the case for a focused incident beam, the correlation range of this correlation is comparable to the correlation range of F_1. Freund *et al* reported an experimental observation of the C_1 term in the case in which the intensity correlation function in which both the incident and scattered wave vector are shifted by the same amount. In this case the intensity correlation function has been called

the "memory effect" because the output speckle pattern appears to track changes in the incident wave vector and the correlation wave vector is therefore considerably larger than is found within the speckle pattern for fixed incident excitation. A quantitative study of the correlation within the static speckle pattern of transmitted multiply scattered light and its relationship to the "memory effect" has not been presented previously. In this chapter we will describe a general expression for angular correlation functions with arbitrary shift in incident and scattered wave vectors in the field factorization approximation. We then confirm experimentally this expression in measurements of angular correlation within the static speckle pattern and of the "memory effect". It is shown that for a focused incident beam, the correlation function within the speckle pattern and the "memory effect" are given by the same expression.

Freund *et al* [12] found a substantial discrepancy between measurements of the "memory effect" and calculations by Feng *et al.* They showed latter that this discrepancy could be largely removed by incorporating internal reflection in the description of transport and using the internal reflection coefficient R in the expression for the "memory effect" as a fitting parameter [14,16]. In this chapter, we describe measurements of the "memory effect" for the sample in which internal reflection is eliminated by immersing the sample into the index matching fluid. We prove that our diffusion model and the calculation of Feng *et al* describes the measurements of "memory effect" in this case. We also measure the intensity correlation function within the laser speckle pattern for fixed excitation and the "memory effect" in the presence of internal reflection. We find excellent agreement between the prediction of our diffusion model using the scattering

and interfacial parameters determined in chapter 2 and the measurements.

We demonstrate experimentally that measurements of the angular intensity correlation function within the static speckle pattern and the "memory effect" are the Fourier transforms, respectively, of measurements of the intensity distribution on the output surface and of the propagator between the input and output surfaces which is the output spatial intensity distribution for a tightly focused incident beam.

3.2 Samples and Experiments

Measurements are made on a 280 μm slab of the same alumina material described in chapter 2. In the present experiments we use the same laser light source as described in section 2.3.b. The size of the incident beam can be varied by adjusting the spacing between the lenses and the sample. Measurements of the surface intensity profiles, the intensity correlation within laser speckle and the "memory effect" are made in the following procedure. A laser beam is focused to 5 μm on the sample surface. Intensity spectra in the far-field as a function of the angle of the detector with respect to the normal of the fixed sample are recorded by sweeping the detector 175 cm from the sample along an arc from -1.5 to 1.5 degree as shown in Fig. 3.1. The normalized intensity correlation function versus shift $\Delta\theta$ in the angle of the detector, $C(\Delta\theta) = \langle \delta I(\theta)\delta I(\theta+\Delta\theta)\rangle$, was computed from 100 such intensity spectra recorded by illuminating different areas of the sample. Correlation functions are calculated using intensity spectra normalized by the angular intensity distribution $<I(\theta)>$ obtained from the average of all spectra. We place a Nikon lens in the front of the sample. The surface transverse intensity profile is magnified 30 times. The transverse profile through the center of the image is recorded by the procedure described in section 2.3.c. We then increase the laser spot size by adjusting the position of the lens at the input side. The surface intensity profile becomes broader and the grainy laser speckle pattern becomes finer with an increasing size of the incident laser beam. We record intensity spectra in the far-field as a function of the angle of the detector and the transverse profile of the image for a 2

mm incident beam.

In order to change the angle of the sample with respect to the incident beam, We mount the sample on the center of a goniometer. Scattered light in the far-field is detected by a fixed detector in the forward direction 175 cm from the sample as shown in Fig. 3.2. The intensity fluctuates as the sample is rotated. We record the intensity spectra as a function of the rotation angle of the sample with respect to the normal of the sample. The total rotation of the sample is about 3 degrees. These measurements were made for 50 μm and 2 mm incident beams. Measurements are made for the sample immersed in index matching fluid as well as in air. The cumulant intensity correlation function versus shift $\delta\theta$ in the sample rotation angle, namely the "memory effect" $C(\delta\theta) = \langle \delta I(\theta)\delta I(\theta+\delta\theta)\rangle$, was calculated using 100 intensity spectra normalized by the average of all intensity spectra.

3.3 Results and Discussion

3.3.a Measurements of $C(\Delta\theta)$ and $C(\delta\theta)$

We use symbol $E_{\{k_a\}k_b}$ to denote the field of scattered wave with wave vector k_b arising from a distribution of incident wave vectors represented by $\{k_a\}$ which give rise to an intensity distribution $I(\rho_a)$ in the transverse coordinate ρ_a on the incident surface. If all the k_a's are shifted by a small amount Δk_a, The field correlation function $I_{\{k_a\}k_b\{k_{a'}\}k_{b'}}$ between $E_{\{k_a\}k_b}$ and $E_{\{k_{a'}\}k_{b'}}$ can be written as [50,24],

$$I_{\{k_a\}k_b\{k_{a'}\}k_{b'}} \propto \int\int I(\rho_a)P(\rho_b-\rho_a)\exp(i(\Delta k_a\cdot\rho_a-\Delta k_b\cdot\rho_b))d\rho_a d\rho_b \tag{3.5}$$

where $k_{a'} = k_a + \Delta k_a$, $k_{b'} = k_b + \Delta k_b$, $P(\rho_b - \rho_a)$ is the intensity propagator in the transverse displacement between the input and output surfaces. For $g \gg 1$, the intensity correlation function is the amplitude square of the field correlation function. Eq. (3.7) gives a general expression for angular correlation functions with arbitrary shift in incident and scattered wave vectors.

If the incident wave with respect to the sample is not shifted, $\Delta k_a = 0$, the intensity correlation function with shift in scattered wave vector k_b for this case can be calculated by integrating Eq. (3.5) over ρ_a and then taking the amplitude square. This

gives,

$$C(\Delta \boldsymbol{k}_b) \propto \left|\int I(\boldsymbol{\rho}_b)\exp(-i\Delta \boldsymbol{k}_b\cdot\boldsymbol{\rho}_b)\, d\boldsymbol{\rho}_b\right|^2, \qquad \Delta \boldsymbol{k}_a = 0, \tag{3.6}$$

where $I(\rho_b) = \int I(\rho_a)P(\rho_b - \rho_a)d\rho_a$ is the intensity distribution on the output surface given by the convolution of the input intensity distribution with the propagator. If $\boldsymbol{k}_a$ and $\boldsymbol{k}_b$ are shifted by the same amount, $\Delta \boldsymbol{k}_a = \Delta \boldsymbol{k}_b \equiv \Delta \boldsymbol{k}$, we obtain the intensity correlation function,

$$C(\Delta \boldsymbol{k}) \propto \left|\int P(\boldsymbol{\rho})\exp(-i\Delta \boldsymbol{k}\cdot\boldsymbol{\rho})\, d\boldsymbol{\rho}\right|^2, \qquad \Delta \boldsymbol{k}_a = \Delta \boldsymbol{k}_b. \tag{3.7}$$

This expression gives the "memory effect".

We notice from Eq. (3.9) that the "memory effect" $C(\delta\theta)$ is the amplitude square of the Fourier transform of the intensity propagator $P(\rho)$. In the diffusive regime, the width of $P(\rho)$ is roughly the sample thickness L, the correlation range of $C(\delta\theta)$ is then $\delta k \sim L$. δk is independent of the width of the incident spot. In contrast, the range of intensity correlation within the speckle pattern $C(\Delta\theta)$ δk_b decreases with an increasing size of the incident beam $\delta\rho_a$. This is because $\delta k_b \sim 1/\delta\rho_b$, where $\delta\rho_b$ is the width of the intensity profile on the output surface, which increases with $\delta\rho_a$. The angular range of $C(\Delta\theta)$ is generally much shorter than $C(\delta\theta)$ since $\delta\rho_b$ is larger than L unless the incident beam is tightly focused. If a tightly focused incident beam is used to measure $C(\Delta\theta)$, it will be the same as $C(\delta\theta)$, since the intensity profile on the output surface $I(\rho_b)$ in this case is equal to the intensity propagator $P(\rho)$. δk_b decreases with a increasing size of the incident beam.

Measurements of the angular intensity correlation functions within speckle pattern

$C(\Delta\theta)$ for an incident beam focused to a 5 μm diameter spot and for a beam expanded to a 2.0 mm diameter spot are shown as the dots in Fig. 3.3 [51]. In the same figure, measurements of the "memory effect" $C(\delta\theta)$ for an incident beam focused to a 50 μm diameter spot and for a beam expanded to a spot 2.0 mm in diameter are shown as the triangles.

These results verify the properties of the correlation functions we described above. Measurements of the "memory effect" $C(\delta\theta)$ for 50 μm and 2.0 mm diameter incident spots are essentially the same. Measurements of the angular intensity correlation functions within speckle pattern $C(\Delta\theta)$ for 5 μm diameter incident spot are also seen to be essentially the same as the measured $C(\delta\theta)$. On the other hand the width of the measured $C(\Delta\theta)$ decreases with an increasing size of the incident spot. It is shown in Fig. 3.3 that $C(\Delta\theta)$ measured for a 2.0 mm diameter incident beam is much narrower than $C(\Delta\theta)$ measured for a 5 μm diameter incident beam.

3.3.b Relation between Correlation and Intensity Distribution

Eq. (3.8) shows that the intensity correlation function within static speckle pattern $C(\Delta\theta)$ forms a Fourier transform pair with the surface intensity distribution $I(\rho_b)$. Eq. (3.9) shows that the "memory effect" $C(\delta\theta)$ forms a Fourier transform pair with the intensity propagator $P(\rho)$.

The intensity profiles at the output surface $I(\rho_b)$ for 5 μm and 2.0 mm diameter incident spot are shown in Fig. 3.4. $P(\rho)$ calculated using the interfacial scattering

parameters determined from measurements of total transmission in the diffusion model described in chapter 2 gives the solid line in Fig. 3.4. It is in excellent agreement with the measured intensity profile for a focused incident beam.

The intensity correlation functions versus detector angle $C(\Delta\theta)$ for an incident beam focused to a 5 μm diameter spot and for a beam expanded to a spot 2.0 mm in diameter on the alumina sample in air are shown as the dots and triangles in Fig. 3.5. The solid lines are the amplitude square of the Fourier transform of the surface intensity distribution $I(\rho_b)$ measured for the focused and broad beams. The agreement with the corresponding correlation functions confirms Eq. (3.6).

The angular correlation function $C(\delta\theta)$ measured for the sample in air is shown in Fig. 3.6. The dots give the measured intensity correlation function with sample rotation angle $C(\delta\theta)$ using a laser beam focused to 50 μm. The triangles give the same correlation function for a 2 mm diameter incident beam. The solid line shown in Fig. 3.6 gives the amplitude square of the Fourier transform of the intensity profile for a tightly focused spot. The dashed line in Fig. 3.6 is the square amplitude of the Fourier transform of the diffusion propagator $P(\rho)$ calculated using scattering parameters measured in chapter 2 for this sample. The agreement confirms Eq. (3.7). This also confirms that measurements of angular correlation functions are consistent with diffusion theory.

The relations verified above can be considered as the application of the classical coherence theory to the scattered light from random media. The ensemble average of the surface intensity distribution is similar to a quasi-monochromatic incoherent light source. The van Cittert-Zernike theorem states that the correlation between two points in the

radiation field from a monochromatic incoherent source can be given by the Fourier transform of the spatial intensity distribution of the source [52]. If these two points are in the far-field, the van Cittert-Zernike can be translated into Eq. (3.6).

The results for $C(\delta\theta)$ are analogous to the intensity correlator with frequency shift in which the input and detected frequency are shifted by the same amount. The intensity correlation function with frequency shift is then the Fourier transform of the time of flight distribution across the slab which is the propagator in the time domain [11].

3.3.c Influence of Internal Reflection

We have demonstrated in the previous section that using Eqs. (3.6) and (3.7), we can predict the angular correlation function within speckle pattern $C(\Delta\theta)$ and the "memory effect" $C(\delta\theta)$ from the Fourier transforms of $I(\rho_b)$ and $P(\rho)$ respectively. The measurements of $C(\Delta\theta)$ and $C(\delta\theta)$ in the previous section are made for the sample in air. In this section we demonstrate the influence of internal reflection on the "memory effect" and show that the diffusion model which incorporates interfacial scattering describes the correlation with and without internal reflection. We also show that the calculation by Feng *et al*, which neglects internal reflection, does not describe measurements of $C(\delta\theta)$ in the presence of internal reflection but agrees with the measured $C(\delta\theta)$ when internal reflection is eliminated.

The angular correlation function $C(\delta\theta)$ measured for the sample in air and the amplitude square of the Fourier transform of the intensity profile for a tightly focused

spot shown in Fig. 3.6 are reproduced in Fig. 3.7. The dashed line in Fig. 3.7 is the angular form factor F_1 given by Eq. (3.4). This shows that Eq. (3.4) does not describe the "memory effect" in the presence of internal reflection.

The role of internal reflection is further considered in the measurements of the angular correlation function $C(\delta\theta)$ for the sample immersed in index matching fluid for an incident beam focused to a 50 μm spot. with n = 1.70. The correlation function, shown in Fig. 3.8, is broader than for the sample in air because the surface propagator is narrower. The solid line is the amplitude square of the Fourier transform of the calculated diffusion propagator with R = 0 using the propagation parameters given above. This line is also in excellent agreement with Eq. (3.7) using the intensity profile measured for a tightly focused beam. The dashed line is the angular form factor F_1 given in Eq. (3.4). The agreement demonstrates that the calculations of Feng *et al* accurately describe the "memory effect" in the absence of internal reflection.

3.4 Conclusion

We have confirmed a general expression for angular correlation functions with arbitrary shift in incident and scattered wave vectors in the field factorization approximation in a study of angular correlation within the static speckle pattern and of the "memory effect". We show that the intensity correlation function within the laser speckle pattern $C(\Delta\theta)$ and the "memory effect" $C(\delta\theta)$ form Fourier transform pairs with the surface intensity distribution $I(\rho_b)$ and the intensity propagator $P(\rho)$ respectively. We demonstrate that the angular intensity correlation function in transmission is fully described by the photon diffusion model when internal reflection is taken into account.

CHAPTER 4 MICROPARTICLE RESONANCES AND TRANSPORT VELOCITY

4.1 Introduction

In this chapter we consider the connection between spatial and temporal measurements in terms of the fundamental bulk transport parameters in space and time, ℓ and D. In order to achieve this, we considered resonances with microstructures. For particle diffusion, ℓ and D are connected by the Boltzmann relation $D = \frac{1}{3}v\ell$, where v is the velocity of particles traveling between scatterers, ℓ is the transport mean free path. This picture is valid for photon diffusion if the size of scatterers is much less than the wavelength. In this case $\ell = \ell_s$, $v = v_p$, where ℓ_s is the scattering mean free path, v_p is the phase velocity. For scatterers comparable in size to the wavelength, however, this picture is not valid. It is well known that for spherical scatterers with diameter comparable to or larger than the wavelength, energy density of waves inside scatterers can be extremely high at resonance [53]. Photons may be 'trapped' in the scatterers. The dwell time of photons within scatterers can be longer than propagation time between scatterers. The influence of resonances may be succinctly accounted by introducing an additional phenomenological parameter, the transport velocity v_t, defined by the relation, $D = \frac{1}{3}v_t\ell$ [18].

Determination of the transport velocity was attempted both theoretically and experimentally [18,54-57]. For a sample of titania particles suspended in air, van Albada *et al* determined the diffusion coefficient D from measurements of correlation function with frequency shift in reflection [18]. They also determined the transport mean free path ℓ from measurements of the total transmission. The potential important influence of

interfacial scattering upon transmission was not determined from experiments. These results led to an extremely small value of the transport velocity. They proposed that the low values of the diffusion coefficient D were caused by the small value of v_t instead of the small values of ℓ.

van Albada *et al* developed a theory based on the Bethe-Salpeter equation in the low density approximation. They argued that their approach confirmed the observed low value of the transport velocity. Barabanenkov *et al*, also developed a theory based on the low-density approximation of the Bethe-Salpeter equation, with a generalized Ward identity for scalar waves [54]. They concluded that the transport velocity is the same as the phase velocity in the low density limit. Soukoulis *et al* used the coherent-potential-approximation to calculate the transport velocity and compared their calculation with our experimental results discussed below [57].

To determine the transport velocity v_t experimentally, it is necessary to quantitatively determine the values of both ℓ and D. As discussed in chapter 2, ℓ can only be obtained once interfacial interactions are properly taken into account. It cannot be accurately determined, therefore, from a single measurement of transmission or from measurements of distributions or correlation in reflection. On the other hand, D can be reliably obtained from measurements of spectral correlation functions or from pulsed measurements in transmission. As long as $L \gg z_b$, spectral correlation functions and the time of fight distribution are not significantly influenced by internal reflectivity.

In this chapter, we study microwave radiation propagation in systems of randomly positioned nearly spherical dielectric particles of uniform size. The volume filling

fraction of the system f is controlled by mixing the alumina spheres with hollow polypropylene spheres. We study transport properties as a function of filling fraction and frequency. We determine the diffusion coefficient D from the intensity correlation function with frequency shift. Resonances are observed in the diffusion coefficient for filling fraction from $f = 0.10$ to 0.4. The resonance structure disappears at $f = 0.56$ where the dielectric spheres are in contact with one another. The method we used in chapter 2 to determine the transport mean free path ℓ is not suitable here because measurements of total transmission is not readily accomplished and the index-matching of a composite structure is not possible. Using the diffusion model established in chapter 2 which includes the influence of interfacial scattering, we developed new methods of measuring ℓ for these samples. The frequency dependence of ℓ for a sample of randomly distributed polystyrene spheres is determined from measurements of intensity distribution inside the sample by Garcia *et al* [24]. The frequency dependence of ℓ for the alumina sample is determined from measurements of transmission through a combination of the alumina sample and the polystyrene sample. We infer the transport velocity v_t from the measured value of D and ℓ. We find v_t to be significantly lower than the phase velocity estimated from a volume fraction argument.

4.2 Samples and Experiments

4.2.a Samples

We have studied the frequency dependence of microwave propagation in two samples in which sphere resonances are clearly exhibited. The first sample is a mixture of nearly spherical, ⅜-inch diameter particles of 90% alumina supplied by Coors Ceramics Inc. and hollow polypropylene spheres of the same diameter with wall thickness of 0.2 mm. The index of refraction of the alumina spheres is 2.91. By varying the volume fraction f of alumina spheres, it is possible to find the range of filling fraction in which the independent scatterer model adequately describes propagation and to discover the filling fraction and frequency at which the strongest scattering occurs. This sample was also chosen to allow us to investigate the source of the small optical diffusion coefficient measured near the second Mie resonance of anatase titania spheres with refractive index 2.2 [58].

The second sample is a combination of a $f = 0.3$, $L = 15$ cm alumina sample and a random collection of ½-inch polystyrene spheres at a volume fraction of 0.56 with changeable thickness. Small air bubbles occupy 4.5% of the volume of the polystyrene spheres. The refractive index of polystyrene is 1.59. The polystyrene sample is placed closer to the microwave source. Two samples components are separated by a 1/32-inch thick circular plastic plate.

The sample is placed in a 7.3 cm inner diameter copper tube, as shown

schematically in Fig. 4.1. Samples are close-packed at total filling fraction of spheres f = 0.56. The tube can be rotated about its axis to obtain independent random sample. The tube is coated with a thin layer of nonabsorbing epoxy to avoid contaminating the sample with copper oxide dust. The sample is contained between two 1/32 -inch thick circular plastic windows. The separation between these windows determines the sample length L.

4.2.b Measurements of Correlation Function with Frequency Shift

The experimental setup for measuring correlation function with frequency shift is shown schematically in Fig. 4.1. Two self-biased ACSM2065-N Schottky diodes made by Advanced Control Components are placed behind the output window. Their wire antennae are put through small holes in the window and bent vertically and taped to the window. The antennae are separated by 1.9 cm. The frequency of a K band Alfred oscillator is swept by a computer-controlled voltage. The radiation is launched from a horn placed 20 cm in front of the copper tube. The radiation is initially vertically polarized. The oscillator output is modulated at 20 kHz and the signal detected by the diode goes to a lock-in amplifier. 4000 point intensity spectra are recorded between 18.0 and 26.0 GHz. The signal is integrated at each frequency for 20 msec. Intensity levels in each of the detectors is measured at each frequency and stored in the computer. After each set of spectra is taken, the copper tube is rotated about its axis for a few seconds to produce a new sample configuration. In order to eliminate the influence of the frequency

dependence of the instrumental response, each of the individual spectra is divided by the average of all spectra taken under similar conditions. Thus, the average value of intensity for these normalized spectra is unity, $\langle I \rangle = 1$, and the corresponding correlation functions give the fractional degree of correlation. To reduce drift, a zero level is taken by cutting off the oscillator every fifty spectrum, and the spectra stored are the difference between the detected signal and the most recent zero level.

4.2.c Measurements of Transmission

The relative transmission as a function of thickness of alumina sample is measured at various filling fraction ranging from 0.10 to 0.56 and at various frequency ranging from 18.0 to 26.0 GHz. The experimental setup is the same as shown in Fig. 4.1. We constantly tumble the sample by continuously rotating the cooper tube. The averaging time at each frequency is half hour. Since the intensity correlation time in the tumbling sample is approximately 5 ms, this corresponds to the average of approximately 3×10^5 independent intensity measurements at each position.

4.3 Results and Discussion

4.3.a Measurements of Absorption Coefficient

The results of relative transmission of alumina samples for various thickness as a function of frequency ν ranging from 18.0 to 26.0 GHz are shown in Fig. 4.2. According to Eq. (2.11),

$$T(L) = \frac{\sinh(\alpha z_b)\sinh[\alpha(z_p+z_b)]}{\alpha z_b \sinh[\alpha(L+2z_b)]}. \tag{4.1}$$

For $L + 2z_b$ larger than α^{-1},

$$T(L) \propto \exp(-\alpha L). \tag{4.2}$$

We plot measured relative transmission as a function of sample thickness at each frequency. For all frequencies, we find the measured relative transmission decreases exponentially with L as predicted by Eq. (4.2). Fig. 4.3 shows the scale dependence of relative transmission at ν = 20.6 GHz. The absorption coefficient α is obtained from the slope this curve. In Fig. 4.4 we plot the absorption length, $L_a = 1/\alpha = (D\tau_a)^{1/2}$ as a function of frequency for various filling fraction, where τ_a is the absorption time. We observe resonance structure for filling fraction f = 0.1 to 0.4. The resonance structure at low filling fraction is expected because the frequencies are in the second Mie resonance regime of the alumina spheres. But surprisingly, resonances persist up to filling fractions as high as f = 0.4, and the resonance structure at f = 0.4 is similar to f = 0.10. At f =

0.56 we find the resonances are 'washed out' where the spheres are touched with one another.

We use the Mie theory to calculate the total scattering cross-section σ and the average of the cosine of the scattering angle, taken over the differential cross-section $\sigma(\theta)$, $<\cos\theta>$. The transport mean free path ℓ for single scattering limit is obtained from,

$$\ell = \frac{\ell_s}{1-<\cos\theta>}. \tag{4.3}$$

In Fig. 4.6, we show the calculated ℓ for $f = 0.30$ as a function of frequency. It is interesting that the measured L_a shown in Fig. 4.4 has similar resonance structure as the calculated ℓ shown in Fig. 4.5.

4.3.b Measurements of Diffusion Coefficient

In this section, we discuss results of measurements of diffusion coefficient D from intensity correlation function with frequency shift.

The random sample within the copper tube, shown schematically in Fig. 4.1, is analogous to an electronic resistor. The corresponding dimensionless conductance is the product of the number of modes in the tube, $N \approx Ak^2$, where A is the cross-sectional area of the tube and k is the magnitude of the wavevector, and the transmission coefficient ℓ/L, $g \approx N\ell/L$. We consider a waveguide which has N modes at a given frequency ω. These modes, or linear combinations of them, define N channels which form a basis for describing incoming and outgoing radiation from a random medium inside the waveguide.

We denote by T_{ba} the transmission coefficient from channel a on the left of the disordered region to channel b on the right. In the present study, a mode is launched down a copper tube and the intensity is detected at points on the output face of the disordered region. Therefore, the incoming channel a corresponds to a waveguide mode, whereas the outgoing channel b corresponds, roughly, to regions of area $(A/N) \approx \lambda^2$ on the output face, where A is the cross sectional area of the tube.

Perfect mixing of channels by the scattering medium implies that the ensemble average of T_{ba}, $\langle T_{ba} \rangle$, does not depend on a or b. The correlation matrix, $C_{ab,a'b'} = \langle \delta T_{ba} \delta T_{b'a'} \rangle / \langle T_{ba} \rangle^2$, is then the sum of three distinct terms,

$$C_{ab,a'b'} = C_1 + C_2 + C_3 = \tilde{A}_1 \, \delta_{aa'} \, \delta_{bb'} + \tilde{A}_2 \, (\delta_{aa'} + \delta_{bb'}) + \tilde{A}_3. \tag{4.4}$$

The leading contributions to the coefficients $\tilde{A}_1$, $\tilde{A}_2$ and $\tilde{A}_3$ were calculated in Ref. 12. Using the results of these references to calculate higher order corrections gives,

$$\tilde{A}_1 = 1 - \frac{2}{3g_0} + \frac{13}{45g_0^2}, \tag{4.5a}$$

$$\tilde{A}_2 = \frac{2}{3g_0} - \frac{14}{45g_0^2}, \tag{4.5b}$$

$$\tilde{A}_3 = \frac{2}{15g_0^2}, \tag{4.5c}$$

where g_0 is the leading contribution to the average conductance. The results above are for a fixed frequency in the absence of absorption. However, it is of interest to study correlation between T_{ba} at frequency ω and $T_{b'a'}$ at frequency ω' in the presence of absorption. Since the frequency shift $\Delta\omega$ and absorption do not affect the perfect mixing

of channels, the structure of Eq. (4.4) is not changed. The coefficients of the Kronecker deltas in Eq. (4.4), however, do depend upon the frequency shift $\Delta\omega$, and the inverse absorption rate $\Gamma = 1/\tau_a$ and become functions of $\tau\Delta\omega$ and $\tau\Gamma$, where $\tau = L^2/D$. These coefficients may be written as products of frequency independent functions A_i and frequency form factors F_i:

$$\tilde{A}_i(g_0,\tau\Gamma,\tau\Delta\omega) = A_i(g_0,\tau\Gamma)F_i(g_0,\tau\Gamma,\tau\Delta\omega), \tag{4.6}$$

where, $F_i(g_0,\tau\Gamma,0) = 1$ and $A_i(g_0, 0)$ are given by Eq. (4.5).

In the limit of large g_0 and strong absorption (g_0, $\tau\Gamma \gg 1$), the form factors F_1 and F_2 on the output face of the sample are given by,

$$F_1 = \frac{\sqrt{\tilde{\alpha}^4 + \tilde{\beta}^4}}{\cosh(2\gamma_+) - \cos(2\gamma_-)} \frac{\cosh(2\tilde{\alpha}) - 1}{\tilde{\alpha}^2}, \tag{4.7a}$$

$$F_2 = \frac{\sqrt{\tilde{\alpha}^4+\tilde{\beta}^4}}{\cosh(2\gamma_+)-\cos(2\gamma_-)} \frac{\gamma_+\sinh(2\gamma_+)-\gamma_-\sin(2\gamma_-)-\tilde{\alpha}\sinh(2\tilde{\alpha})}{\tilde{\beta}^4/4}, \tag{4.7b}$$

where $\tilde{\alpha}^2 \equiv \tau\Gamma$, $\tilde{\beta}^2 \equiv \tau\Delta\omega$, and $\gamma_\pm^2 \equiv \frac{1}{2}(\sqrt{\tilde{\alpha}^4 + \tilde{\beta}^4} \pm \tilde{\alpha}^2)$. F_1 is obtained within the field-factorization approximation, and decays as a result of the randomization of phase with frequency shift, whereas F_2 results from the diffusion of short-range intensity fluctuations which arise in the field factorization approximation.

Fig. 4.6 shows intensity fluctuation as a function of frequency for $f = 0.30$ alumina sample at L = 20 cm. We compute intensity correlation functions from 6,000 such

spectra over frequency range 0.4 GHz. The correlation function for a sample of length L = 20 cm and filling fraction f = 0.30 is given by the dots in Fig. 4.7. These data are fit by the expression, $A_1F_1(\Delta\omega) + A_2F_2(\Delta\omega) + Const.$, using A_1, A_2, D and *Const.* as fitting parameters and using the measured value of the absorption length L_a shown in Fig 4.4.

The frequency and filling fraction dependence of D in the alumina sample determined from these fittings are shown in Fig. 4.8. Sharp resonances in D are observed up to f = 0.40. At f = 0.56, D is nearly independent of frequency, indicating the breakdown of the independent scatterer approximation.

4.3.c Measurements of Transport Mean Free Path

Our goal in this section is to determine the transport mean free path ℓ for the alumina samples. In chapter 2, we determined ℓ in optical measurements from the extrapolation length z_b for samples in which internal reflection is eliminated by index-matching. But this technique cannot be applied directly to microwave samples because index-matching is not available in microwave frequency. Two methods are developed to determine ℓ for microwave samples.

Garcia *et al* measured intensity distribution inside the sample along the longitudinal axis $I(z)$ [22]. The extrapolation length on the output surface z_b at each frequency are determined by fitting the expression for the intensity inside the sample versus distance, $L - z$, from the output face, $I(z) \propto \sinh[\alpha(L - z + z_b)]$, to measurements

inside a $f = 0.56$ polystyrene sample of length 150 cm as shown in Fig. 4.9. The values of ℓ and of the reflection coefficient R at 18.5 GHz are determined from measurements of z_b at the output surface and of the relative transmission through the sample with and without additional copper plates with a variety of holes on the output face of the sample. These measurements give $\ell = 6.5 \pm 0.3$ cm and $R = 0.13$ at 18.5 GHz. We expect that the value of R does not display strong resonant behavior over the K band for this high density sample. Therefore, the value of the R at 18.5 GHz is used over this frequency range. The frequency dependence of the transport mean free path is then found by solving the Eq. (2.10),

$$z_{b1,2} = \frac{1}{2\alpha} \ln\left(\frac{1 + \alpha z_{1,2}}{1 - \alpha z_{1,2}}\right), \tag{4.8}$$

using the measurements of the frequency variation of z_b and α. The results are given in Fig 4.10.

The second method is measuring relative transmission through an combination of two different samples $T(L_1, L_2)$, where L_1 and L_2 are the thickness of the first and second sample respectively. $T(L_1, L_2)$ is calculated using the diffusion model developed by Lisyansky *et al*,

$$\frac{T(L_1,L_2)}{T(L_1^{(0)},L_2^{(0)})} = \frac{\cosh Z_2}{\cosh Z_2^{(0)}} \frac{\sinh Z_1 + r \tanh z_2 \cosh Z_1}{\sinh Z_1^{(0)} + r \tanh Z_2^{(0)} \cosh Z_1^{(0)}}. \tag{4.9}$$

where $Z_{1,2} = \alpha_{1,2}(L_{1,2}+z_{b1,2})$, $Z^{(0)}_{1,2} = \alpha_{1,2}(L^{(0)}_{1,2}+z_{b1,2})$, $r = \alpha_1\ell_1/\alpha_2\ell_2$, here $L^{(0)}_{1,2}$ represents initial thickness of two samples. In our experiments, 1 and 2 represent polystyrene and

alumina sample respectively. We choose f = 0.56 polystyrene sample with changeable length as the first sample, and f = 0.30 alumina sample of a constant 15 cm thickness as the second sample, $L_2 = L_{02}$ = 15 cm. At this thickness, $\alpha L_2 > 1.9$ for all the frequencies we study, so $_{Z2} = \alpha(L_2 + 2z_b) > 1.9$ and $\tanh_{Z2} \approx 1$, we can then reduce Eq. (4.9) to,

$$\frac{T(L_1,L_2)}{T(L_1^{(0)},L_2^{(0)})} = \frac{\sinh Z_1 + r\cosh Z_1}{\sinh Z_1^{(0)} + r\cosh Z_1^{(0)}}. \qquad (4.10)$$

The transport mean free path ℓ of f = 0.30 alumina sample ℓ at each frequency are determined by fitting Eq. (4.9) to measurements as shown in Fig. 4.11. Since α_1, α_2, z_{b1} and ℓ_1 are obtained from previous experiments, the only fitting parameter is $r = \alpha_1\ell_1/\alpha_2\ell_2$. Fig. 4.12 shows ℓ as a function of frequency for 0.30 alumina sample.

4.3.d. Results for Transport Velocity and Phase Velocity

From the ratios of the data in Figs. 4.8 and 4.12, we obtain the transport velocity, $v_t = 3D/\ell$ for f = 0.30 alumina sample shown in Fig. 4.13. A low value of v_t is observed with a minimum transport velocity of $v_t \approx 0.6 \times 10^{10}$ cm/s. But no sharp resonance structure is observed. Figs. 4.16 and 4.17 are the frequency dependence of v_t calculated by van Albada *et al* [18] and Soukoulis *et al* respectively [63]. The sharp resonances shown in Fig. 4.16 are not observed in our measurements. On the other hand, the curve in Fig. 4.17 which is calculated using refractive index n = 2.91 agrees qualitatively with our data.

The absorption rate obtained from the relation $\tau_a^{-1} = D\alpha^2$ is shown in Fig. 4.14. The absorption rate may be written as $\tau_a^{-1} = f_t\Gamma$, where Γ is the absorption rate of bulk alumina and f_t is the fractional time that photons dwell inside the alumina spheres. We assume the effective medium approximation can be applied to $f = 0.56$ sample. f_t for $f = 0.56$ sample is estimated using the effective medium approximation to be 0.79. Using this value and $\tau_a^{-1}(\lambda)$ for $f = 0.56$ sample shown in Fig 4.14 we obtain bulk absorption rate $\Gamma(\lambda)$. We then calculate f_t for $f = 0.30$ sample by $f_t = \tau_a^{-1}/\Gamma$. The phase velocity v_p is calculated by $v_p = f_t c/n + (1-f_t)c$, where c the speed of light in vacuum and n is the refractive index of alumina. The frequency dependence of v_p for $f = 0.30$ alumina sample is shown in Fig. 4.15. It shows that v_t is a factor of 2 smaller than v_p. This result is consistent with the theoretical results of van Albada *et al* and Soukoulis *et al.*

4.3.e Proximity to Localization

A Langevin calculation of the magnitude of the leading order term in the contribution of C_2 to the crosscorrelation function, C^x, for $L > L_a$ gives [59-60],

$$C^x = (3\pi/4)(1/Ak^2)(L/\ell) \tag{4.11}$$

where A is the area of the sample cross-section and $k = 2\pi\nu/v_p$ is the wave vector, ν is the frequency and v_p is the phase velocity inside the sample. The dots in Fig. 4.18 represent C^x calculated from Eq (4.11) using ℓ and v_p shown in Fig. 4.12 and Fig. 4.15.

Measurements of crosscorrelation are made for $f = 0.30$ and $L = 20$ cm alumina sample. The intensity is detected by two Schottky diodes with parallel antenna separated

by 1.9 cm at the output surface of the sample. Spectra are taken in successive static configurations as the frequency is swept between 18 and 26 GHz. We compute the crosscorrelation function with frequency of 20,000 spectra over frequency intervals $\Delta \nu$ = 0.5 GHz. The frequency dependence of the magnitude of the crosscorrelation function is shown by the triangles in Fig. 4.18.

The lowest order of the dimensionless conductance g is given by $g = 1/(2C^{x})$. The lowest value of g obtained from Fig. 4.18 is 16. This shows that in the frequency range from 18 to 26 GHz, the localization transition is not approached in this system.

4.4 Conclusion

At low filling fraction, we observe resonances in the transport mean free path ℓ, diffusion coefficient D and absorption time. We find surprisingly that the resonances persist up to filling fraction as high as $f = 0.4$. Resonances structure is no longer observed at $f = 0.56$ where the scatterers are in contact with each other. We determine the frequency dependence of the transport mean free path ℓ and diffusion coefficient D at various filling fractions of the scatterers. The transport velocity v_t inferred from the relation $v_t = 3D/\ell$ is found to be substantially lower than the phase velocity v_p, but resonances in v_t is not convincingly observed.

CHAPTER 5 SUMMARY

In this thesis, we have presented a quantitative description of wave propagation in random media. It provides a diffusion model for both static and dynamic transport and makes connection between them. In order to achieve this, we incorporate interfacial scattering into diffusion model and understand the influence of microparticle resonances. A diffusion model utilizing a minimum number of parameters is established to give a self-consistent description of transport. The model incorporate the internal reflection and randomization processes at the sample interfaces. The model is in excellent agreement with a variety of independent optical measurements, including total transmission, surface intensity profiles and transit time distribution. Internal reflection and surface penetration depth are varied independently in these measurements. The transition from ballistic to diffusive transport is found in measurements of transmission. We find the diffusion model not to adequately describe measurements of the intensity profiles in reflection. We also apply the diffusion model to describe the underlying wave nature of propagation. We demonstrate experimentally a Fourier transform relationship between the angular correlation functions and the spatial intensity distributions. Measurements of the angular correlation functions are in excellent agreement with diffusion model without adjustable parameters. The correlation function within laser speckle and the "memory effect" are treated on the same footing and obtained from a single relationship.

We study microwave propagation in a system of randomly positioned uniform dielectric spheres. At low filling fraction, resonances in the transport mean free path ℓ,

diffusion coefficient D and absorption time are found due to the Mie scattering from individual spheres in this system. We find that the resonances persist up to filling fraction as high as $f = 0.4$. Resonances structure in transport parameters is 'washed out' at $f = 0.56$ where the scatterers are closely packed. Utilizing the diffusion model, we determine the transport mean free path ℓ and diffusion coefficient D as a function of frequency and filling fraction of the scatterers. The transport velocity v_t inferred from the relation $v_t = 3D/\ell$ is found to be substantially lower than the phase velocity v_p, but resonances in v_t is not convincingly observed.

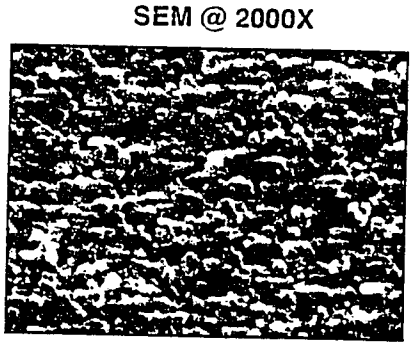

Figure 2.1

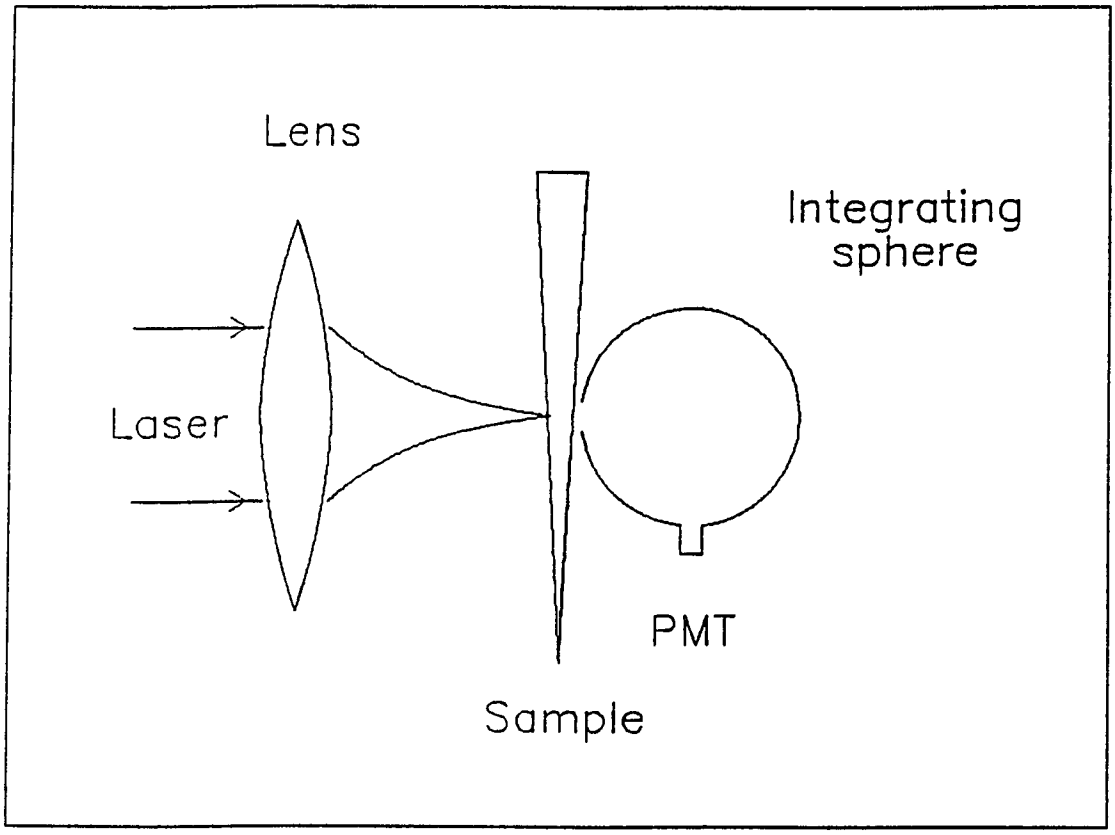

Figure 2.2

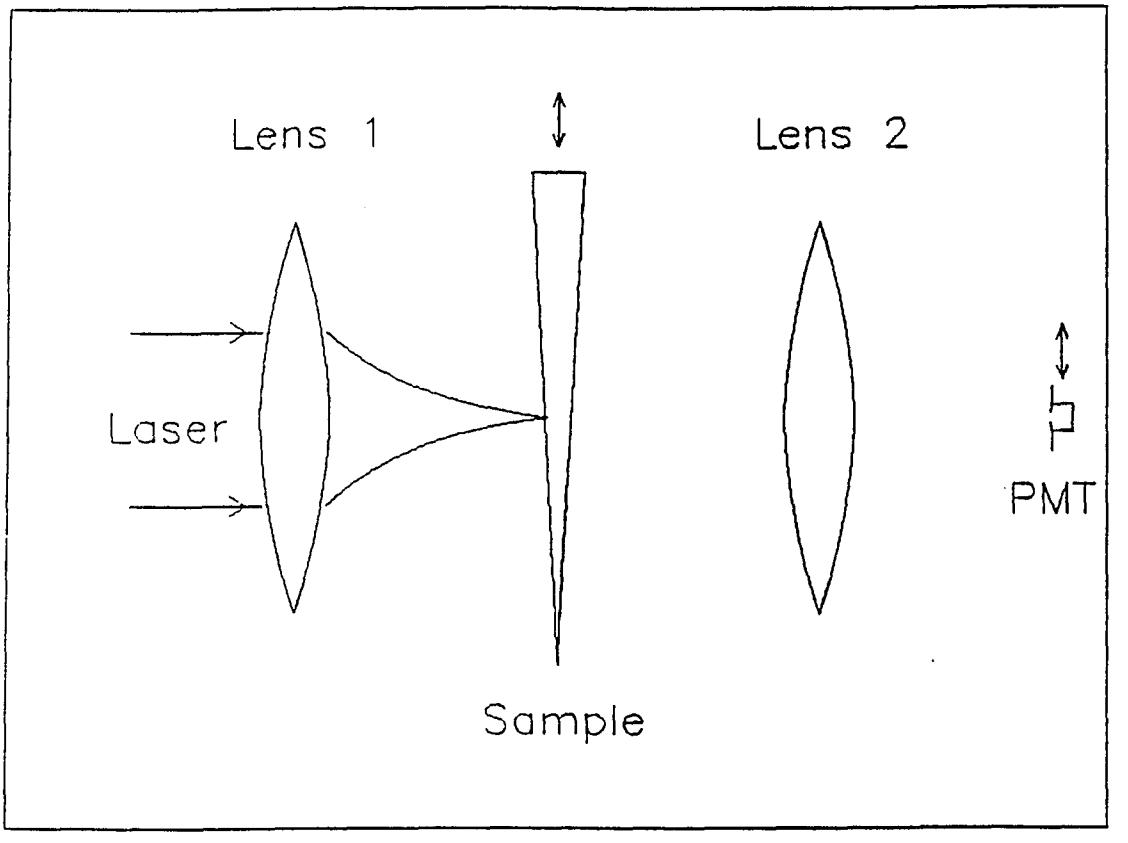

Figure 2.3

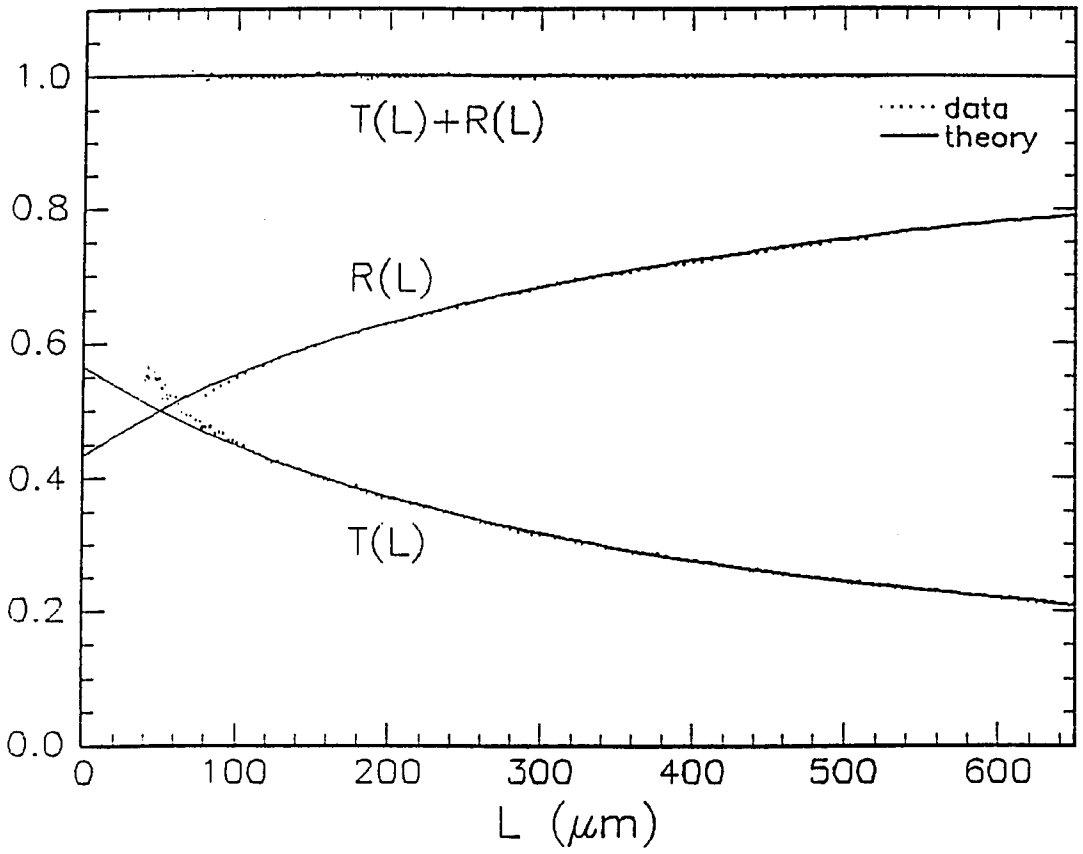
1.0
0.8
0.6
0.4
0.2
0.0
T(L)+R(L)
data
theory
R(L)
T(L)
0
100
200
300
400
500
600
L (μm)

Figure 2.4

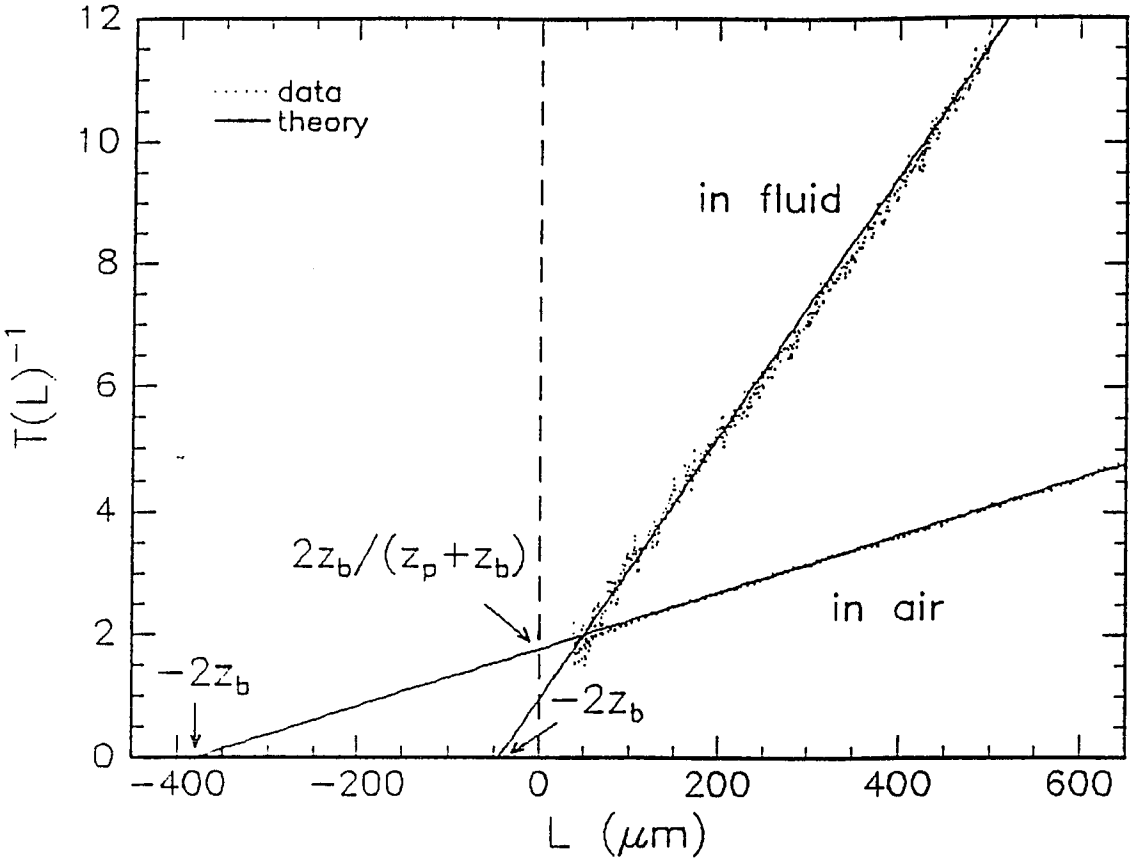
12
10
8
6
4
2
0
T(L)$^{-1}$
data
theory
in fluid
in air
$2z_b/(z_p+z_b)$
$-2z_b$
$-2z_b$
−400
−200
0
200
400
600
L (μm)

Figure 2.5

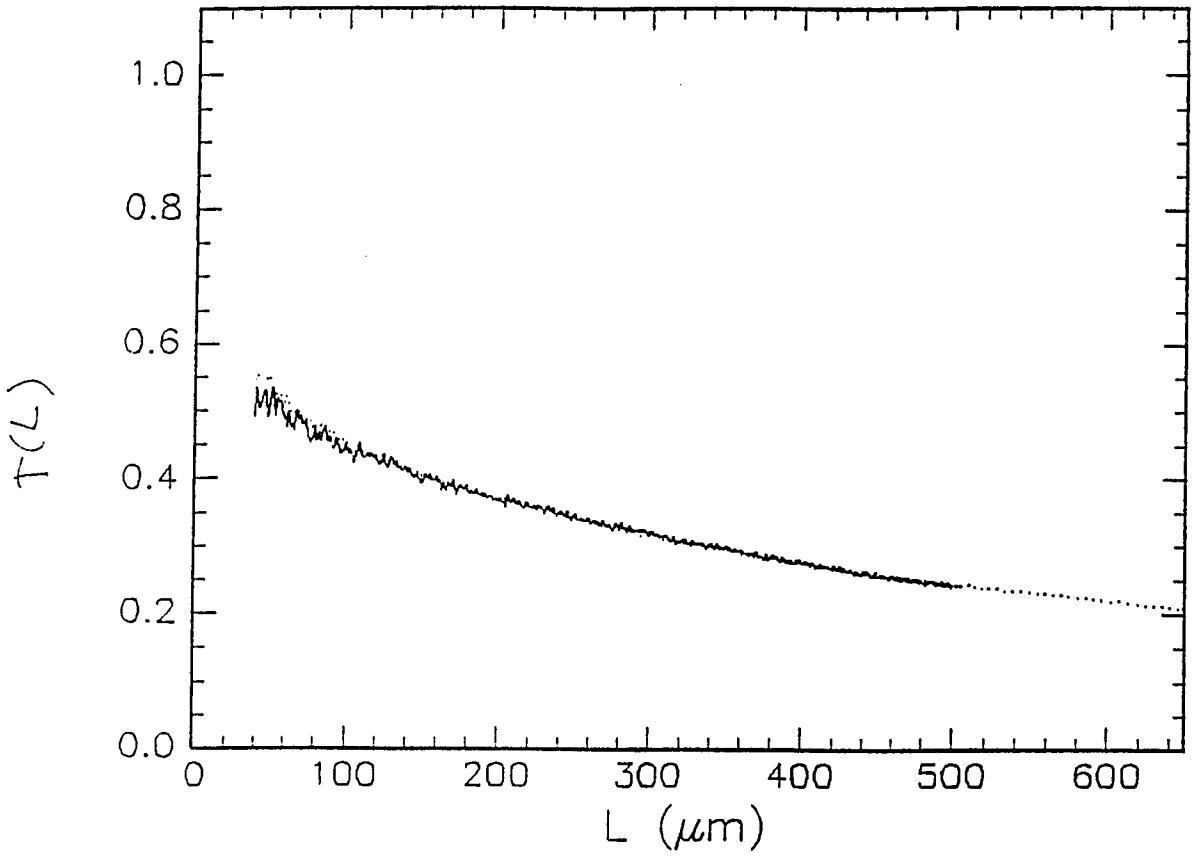

Figure 2.6

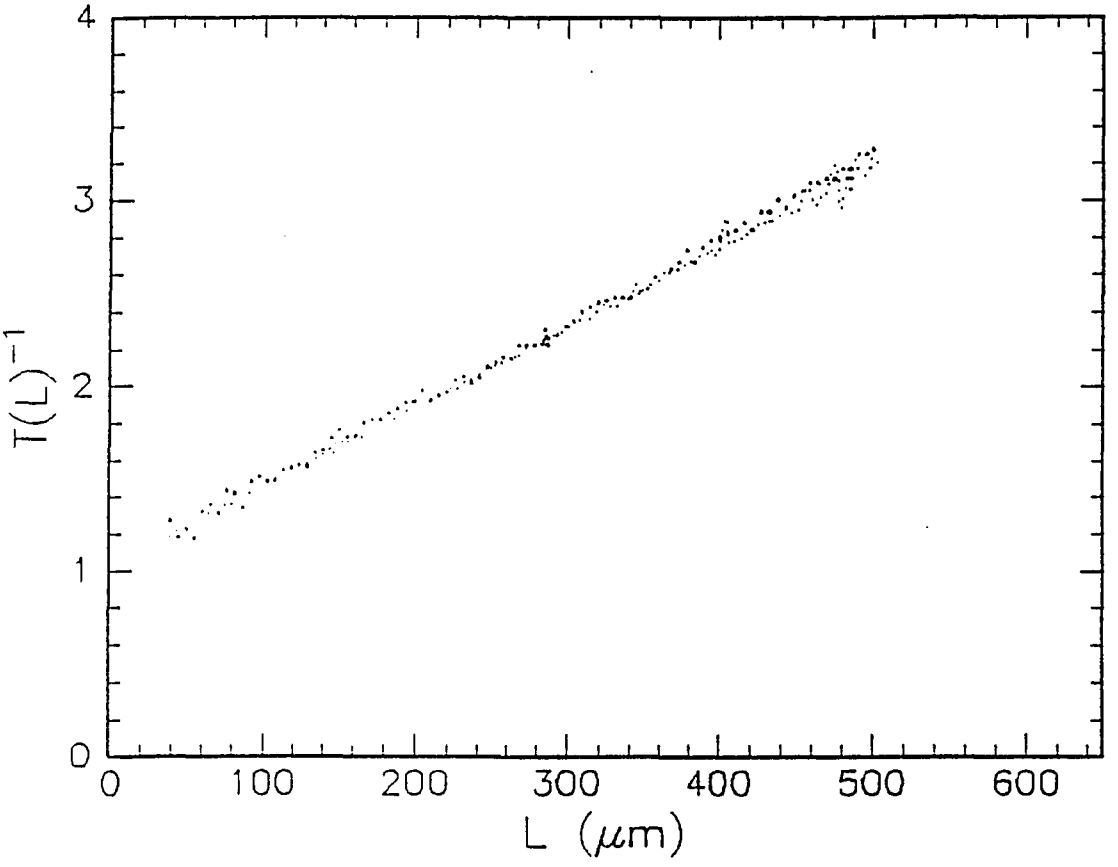

Figure 2.7

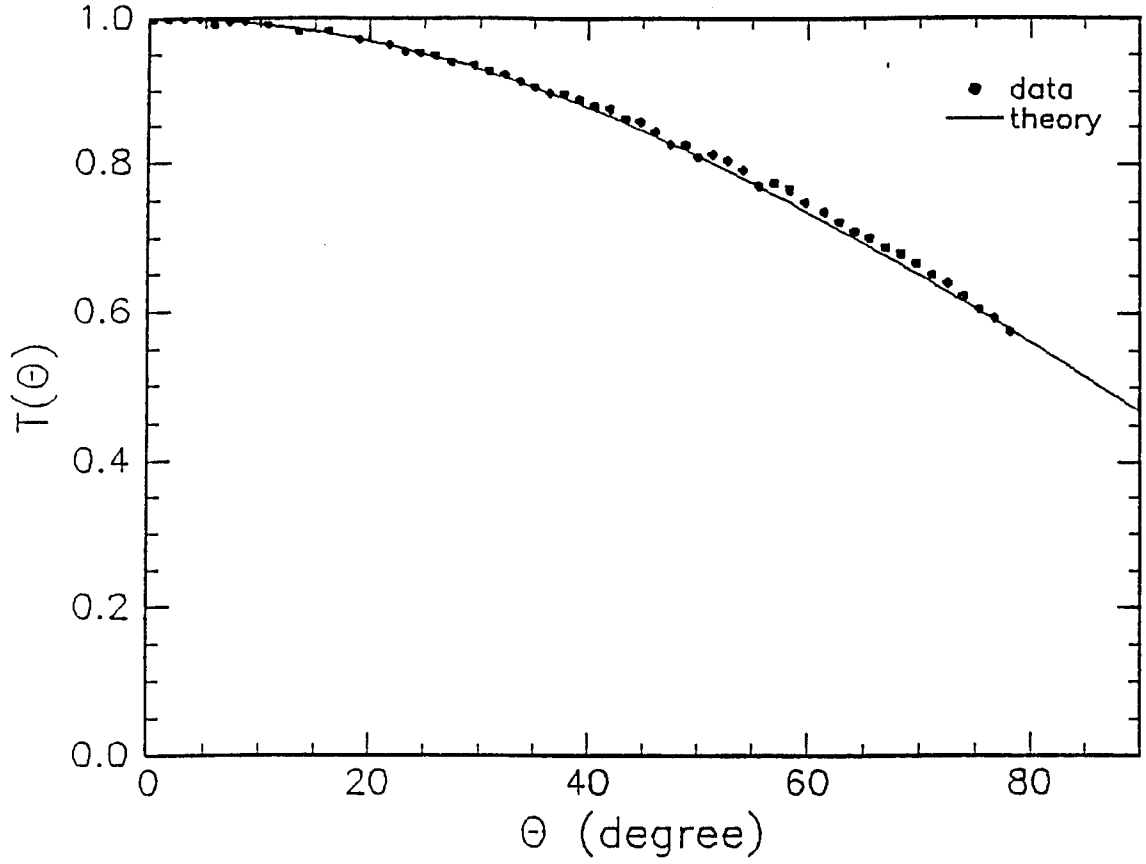

Figure 2.8

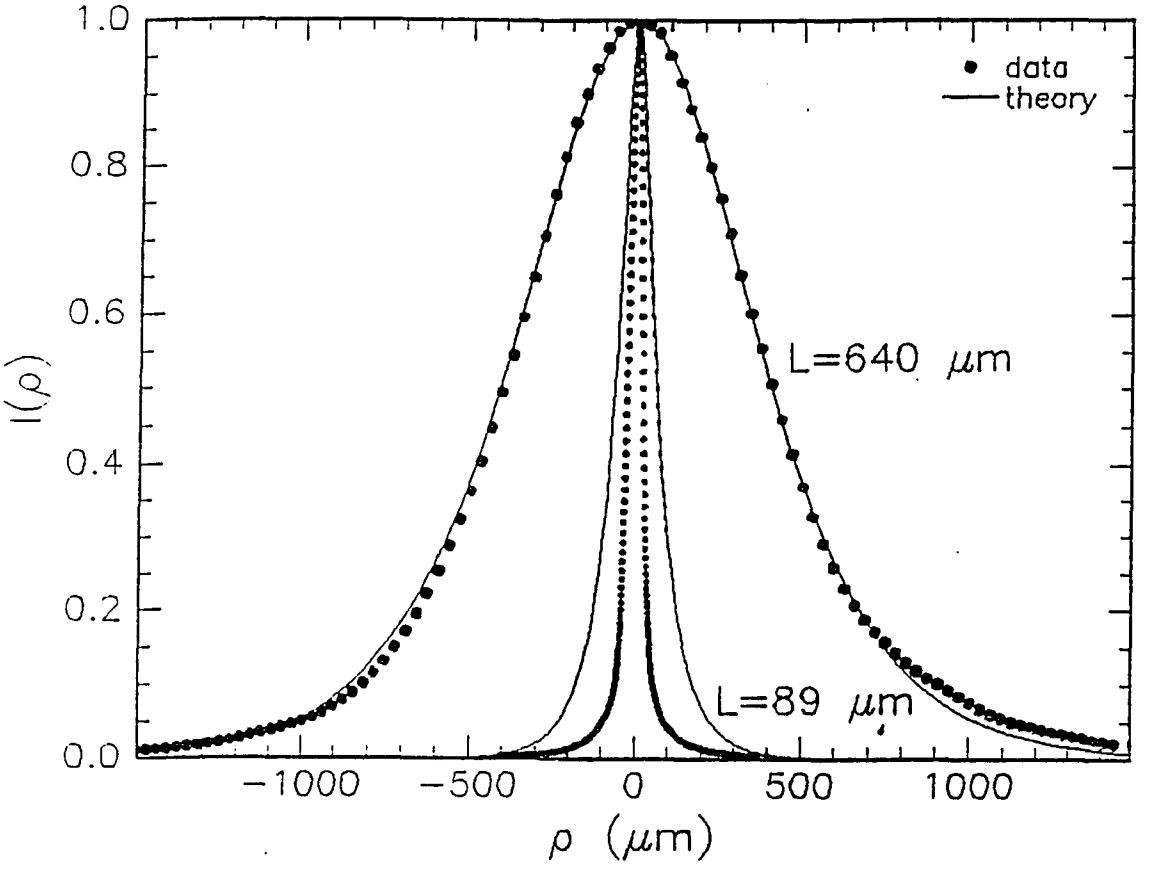
1.0
0.8
0.6
0.4
0.2
0.0
I(ρ)
data
theory
L=640 μm
L=89 μm
−1000
−500
0
500
1000
ρ (μm)

Figure 2.9

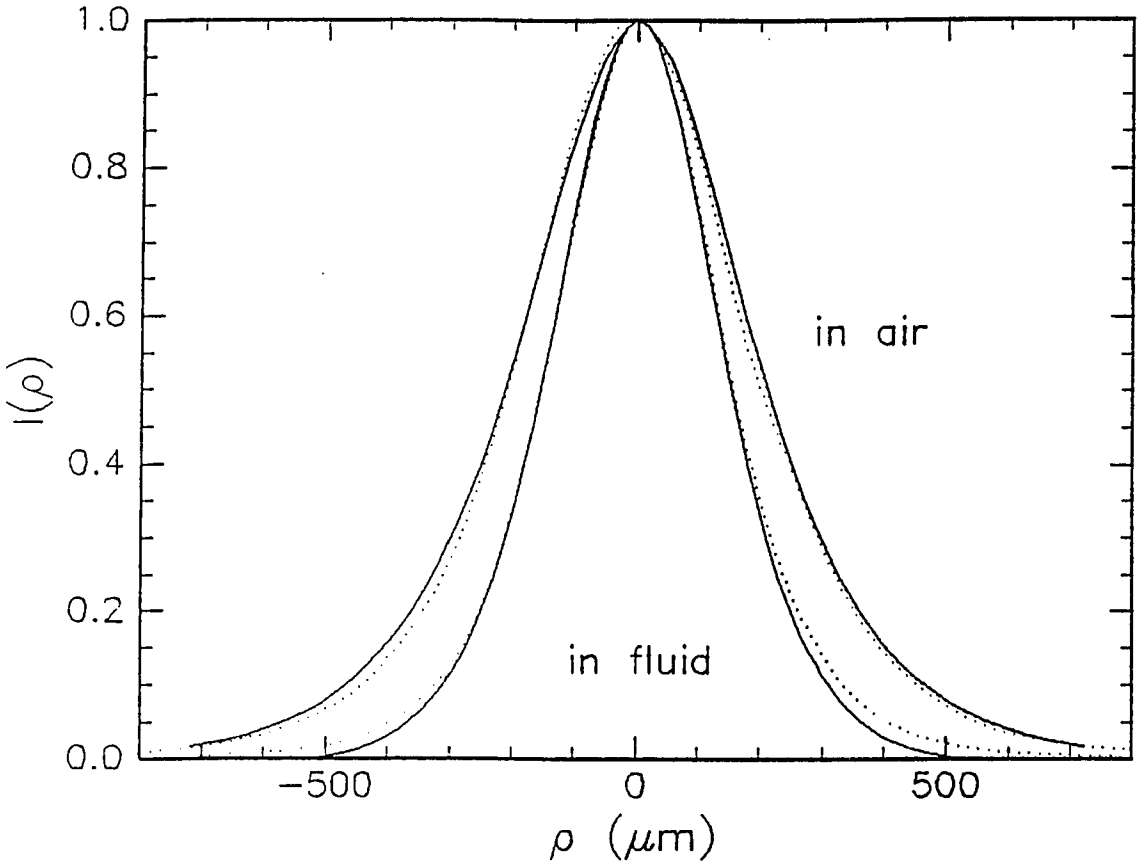

Figure 2.10

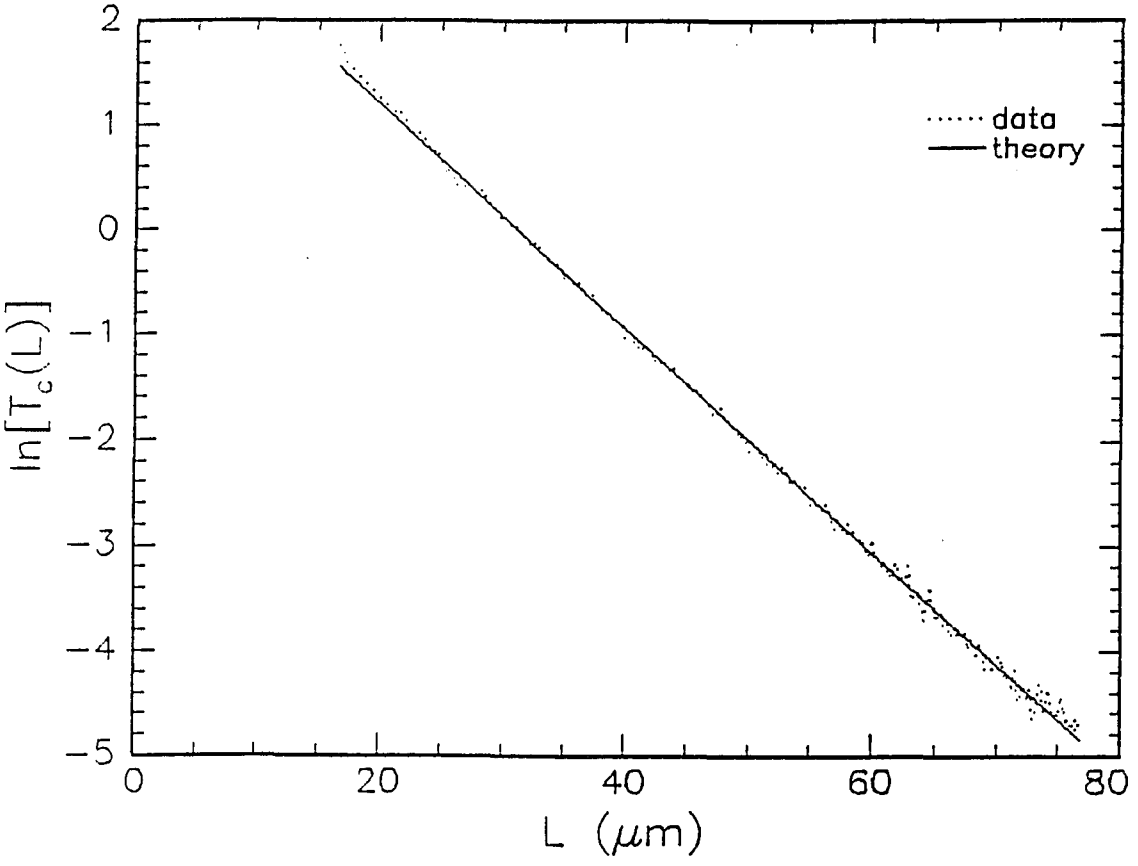

Figure 2.11

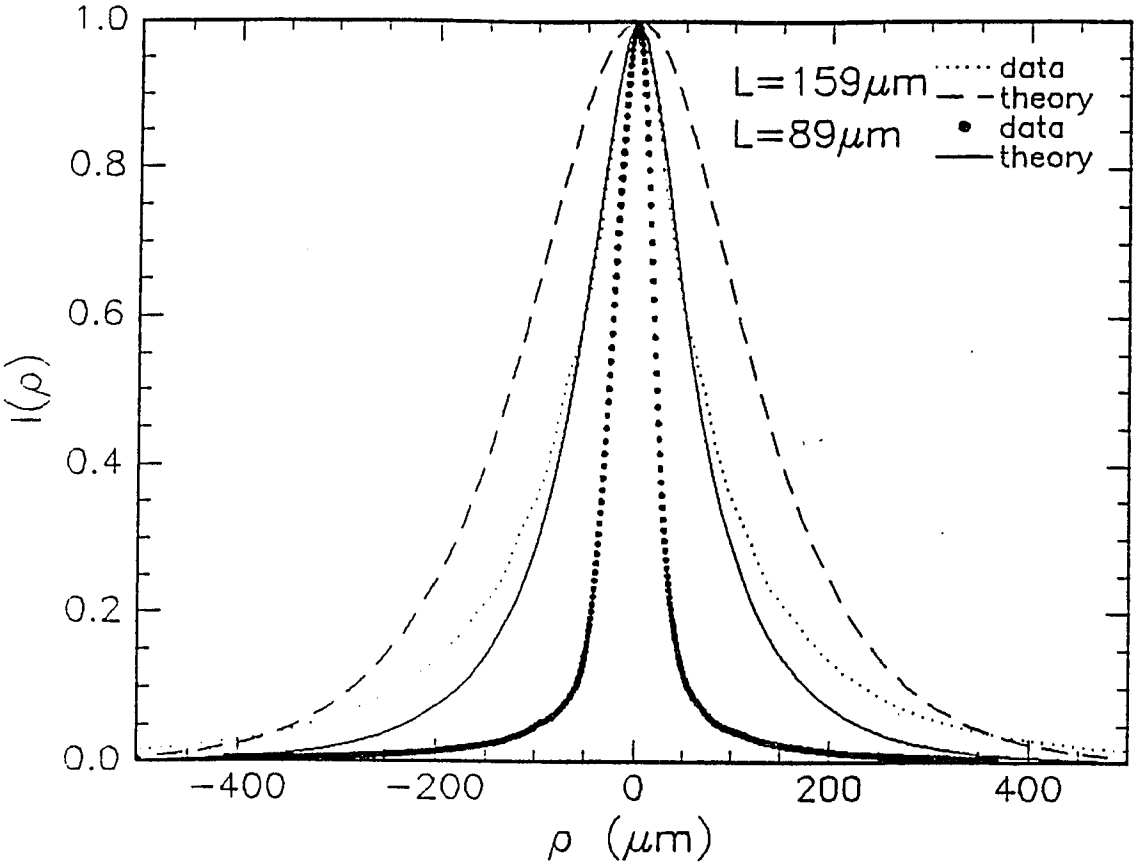
1.0
0.8
0.6
0.4
0.2
0.0
I(ρ)
−400
−200
0
200
400
ρ (μm)
L=159μm
data
theory
L=89μm
data
theory

Figure 2.12

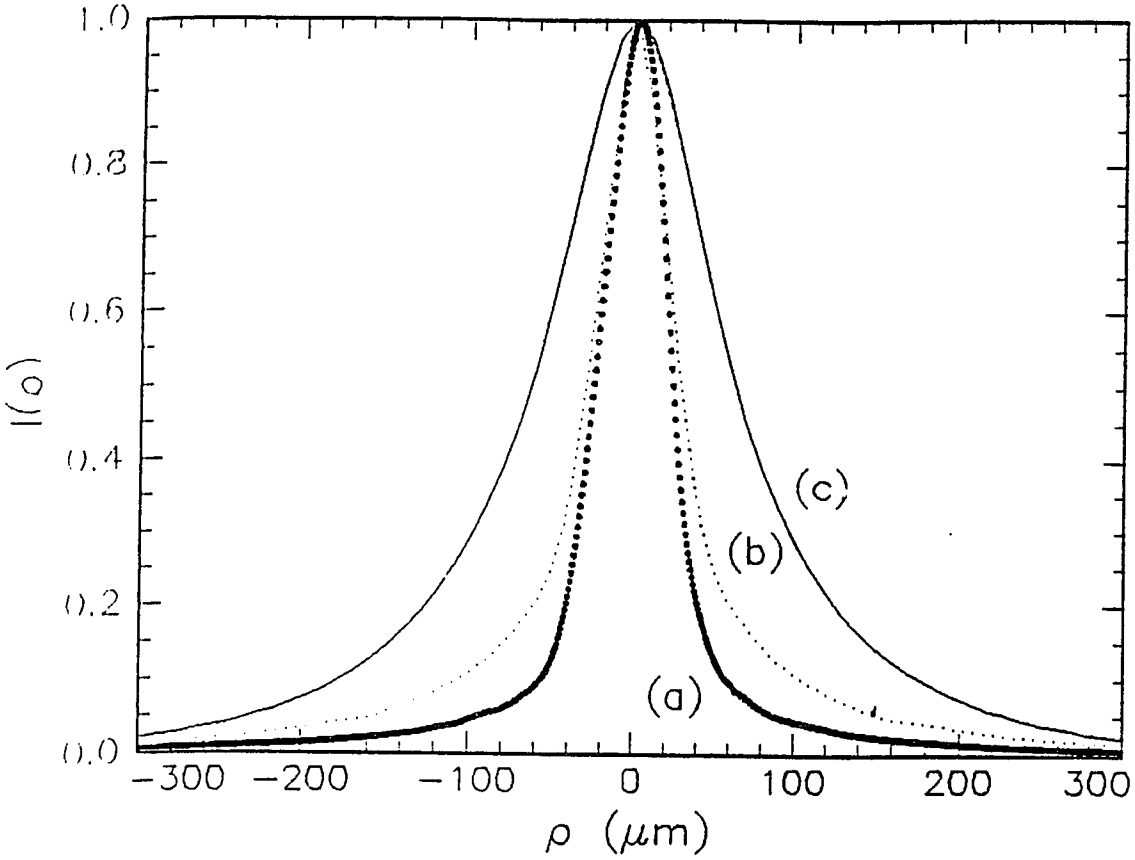

Figure 2.13

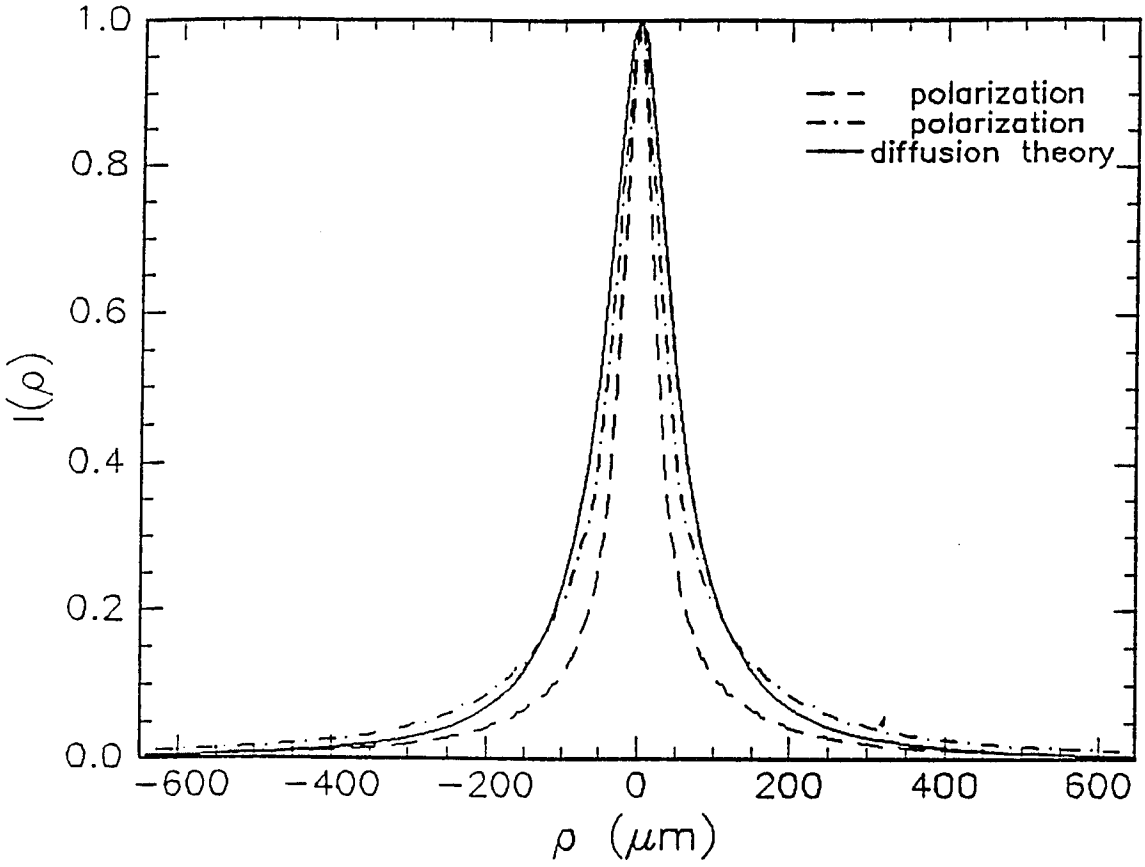
1.0
0.8
0.6
0.4
0.2
0.0
I(ρ)
−600
−400
−200
0
200
400
600
ρ (μm)
polarization
polarization
diffusion theory

Figure 2.14

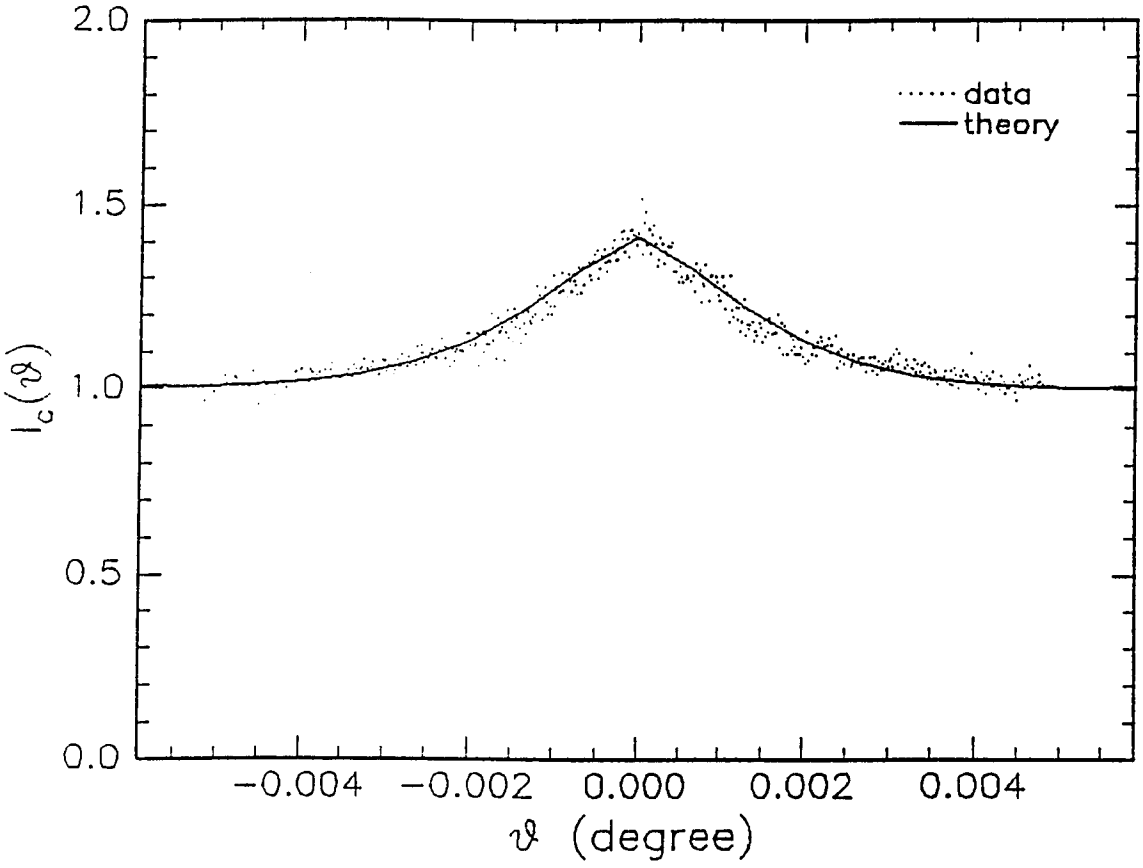
2.0
1.5
1.0
0.5
0.0
$I_c(\vartheta)$
data
theory
−0.004
−0.002
0.000
0.002
0.004
ϑ (degree)

Figure 2.15

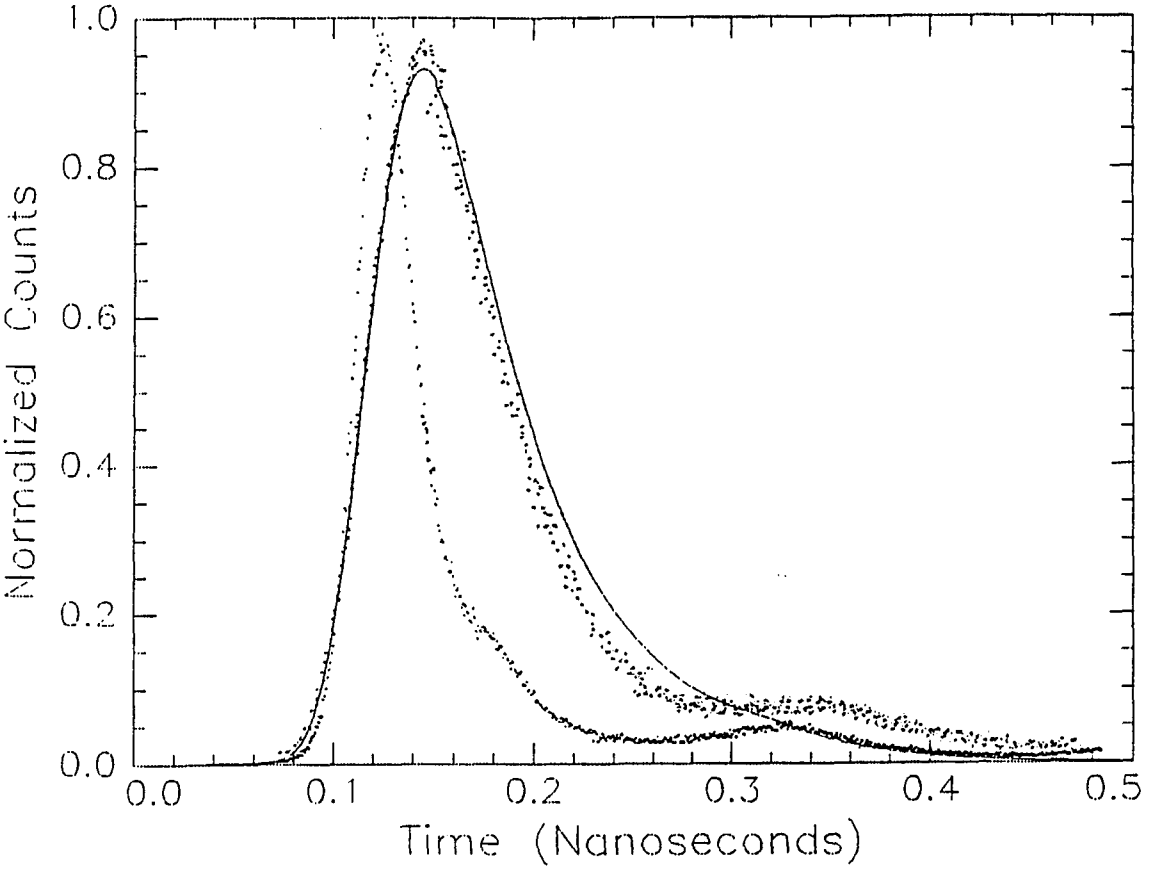
1.0
0.8
0.6
0.4
0.2
0.0
Normalized Counts
0.0
0.1
0.2
0.3
0.4
0.5
Time (Nanoseconds)

Figure 2.16

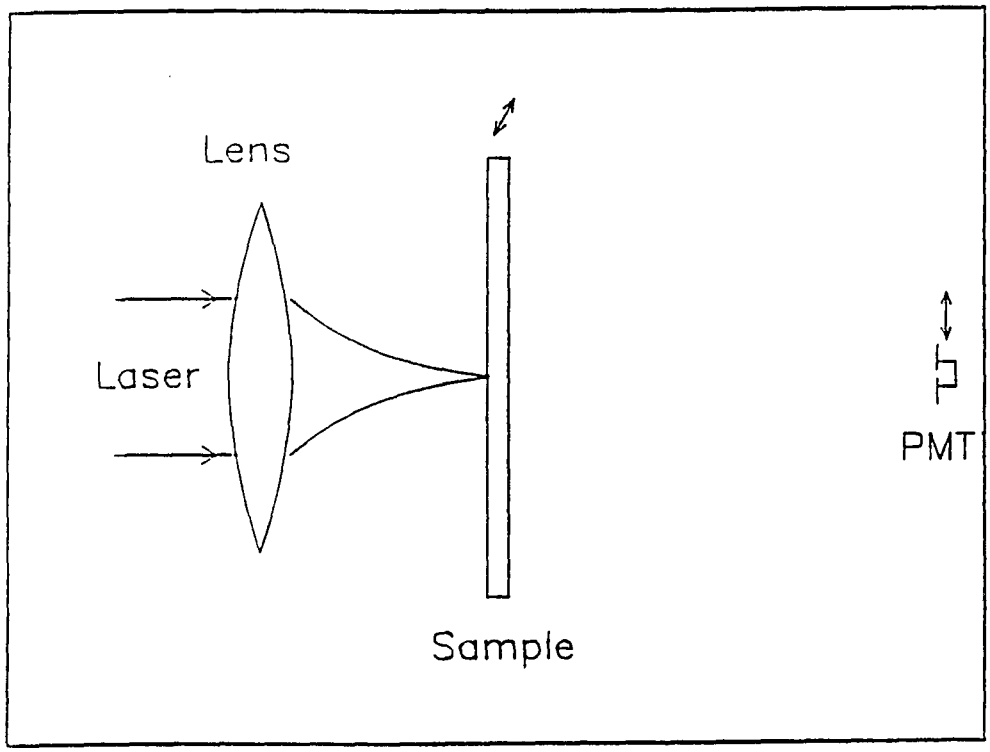

Figure 3.1

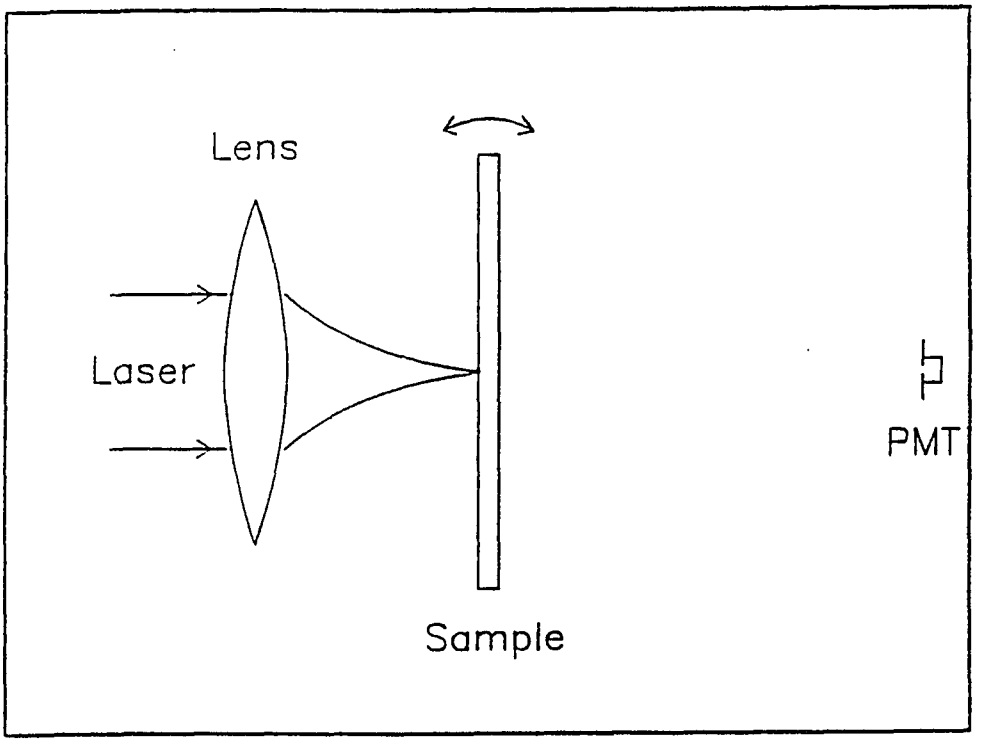

Figure 3.2

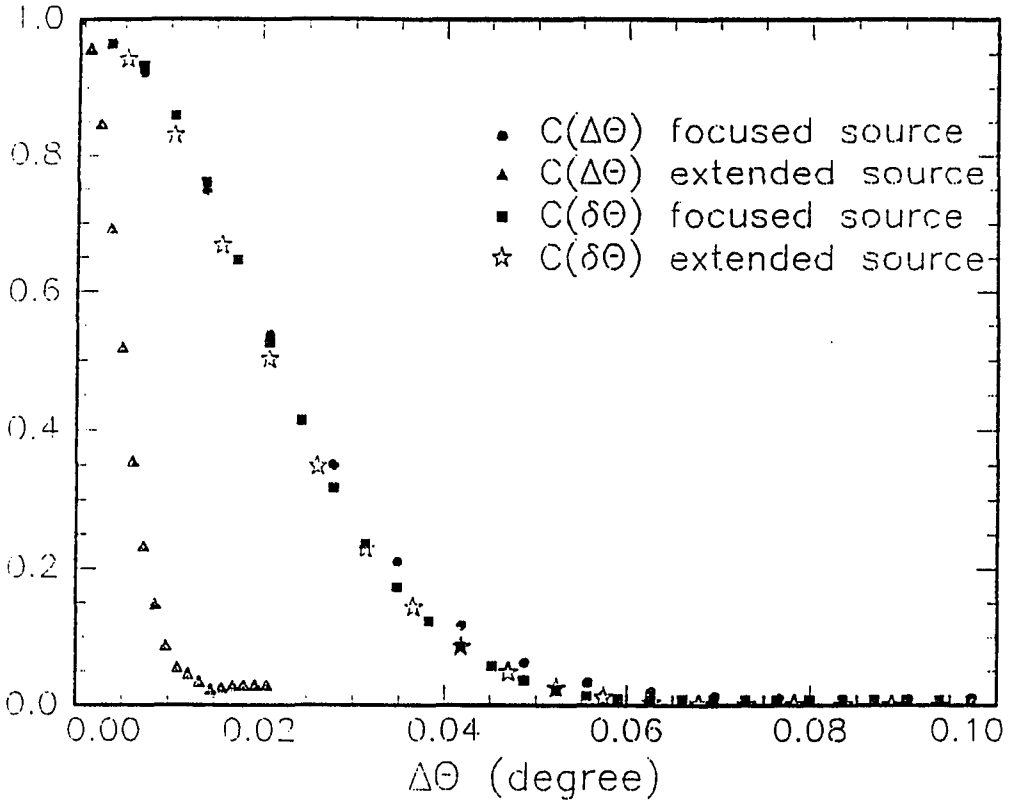
1.0
0.8
0.6
0.4
0.2
0.0
0.00
0.02
0.04
0.06
0.08
0.10
ΔΘ (degree)
C(ΔΘ) focused source
C(ΔΘ) extended source
C(δΘ) focused source
C(δΘ) extended source

Figure 3.3

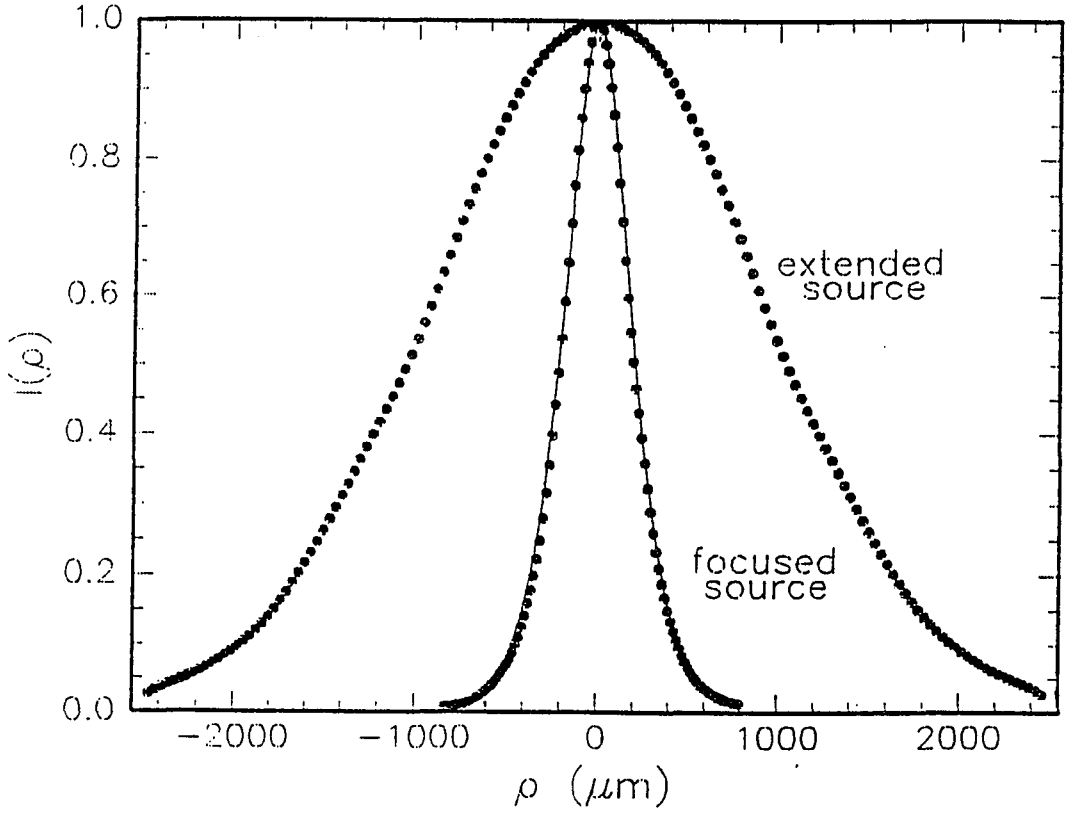
1.0
0.8
0.6
0.4
0.2
0.0
I(ρ)
extended
source
focused
source
−2000
−1000
0
1000
2000
ρ (μm)

Figure 3.4

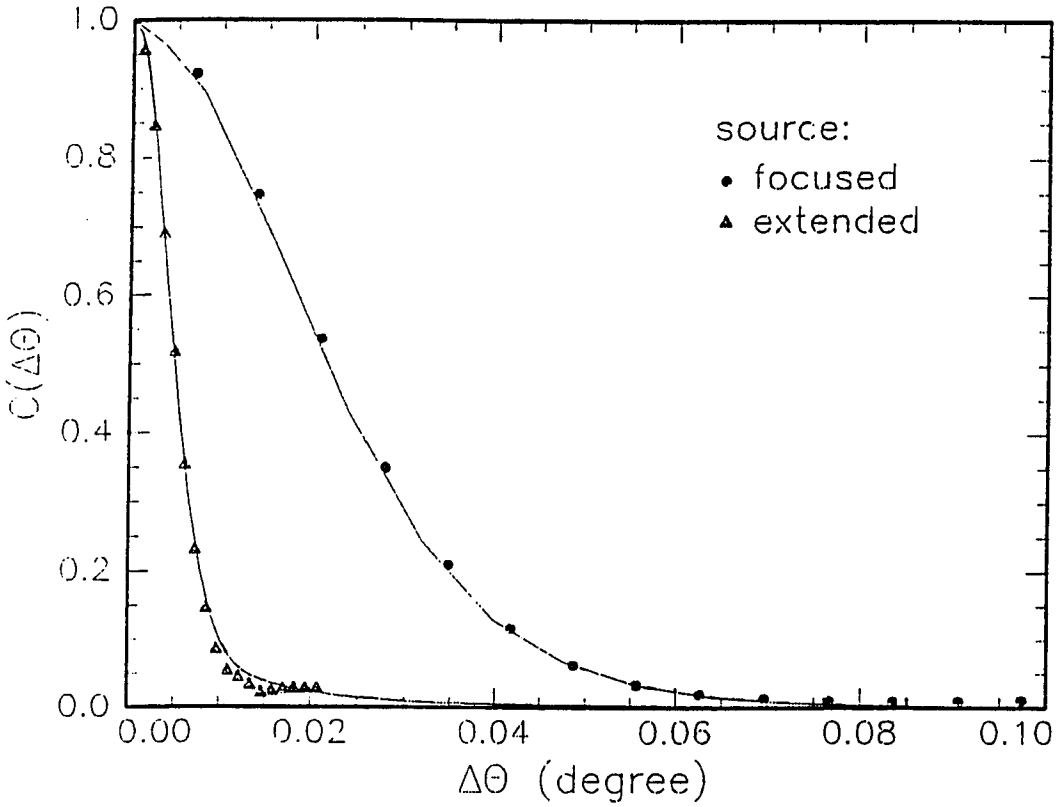
1.0
0.8
0.6
0.4
0.2
0.0
C(ΔΘ)
0.00
0.02
0.04
0.06
0.08
0.10
ΔΘ (degree)
source:
• focused
▲ extended

Figure 3.5

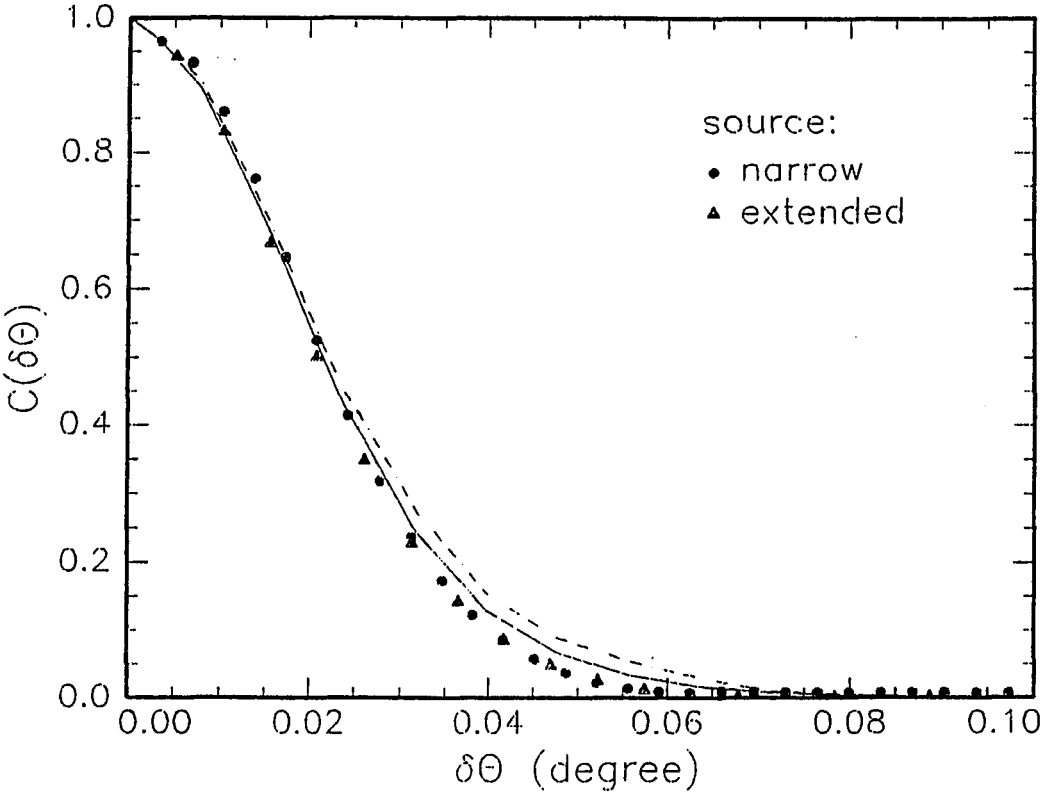
1.0
0.8
0.6
0.4
0.2
0.0
C(δΘ)
0.00
0.02
0.04
0.06
0.08
0.10
δΘ (degree)
source:
• narrow
▲ extended

Figure 3.6

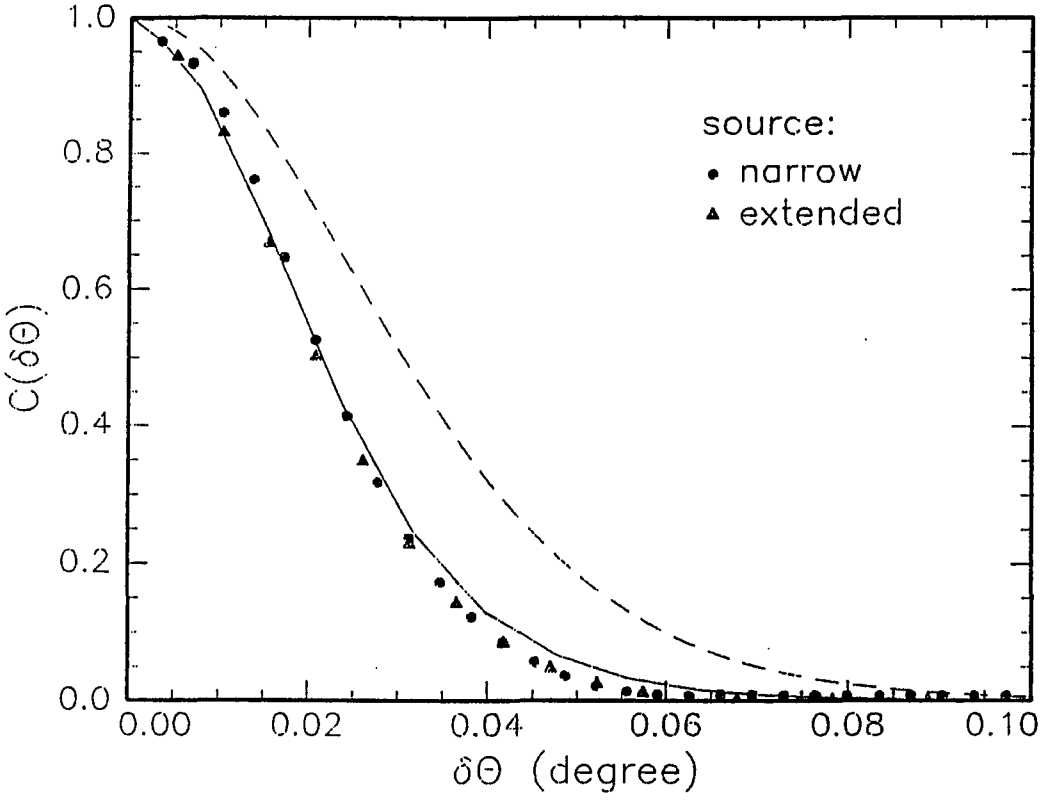
1.0
0.8
0.6
0.4
0.2
0.0
C(δΘ)
0.00
0.02
0.04
0.06
0.08
0.10
δΘ (degree)
source:
• narrow
▲ extended

Figure 3.7

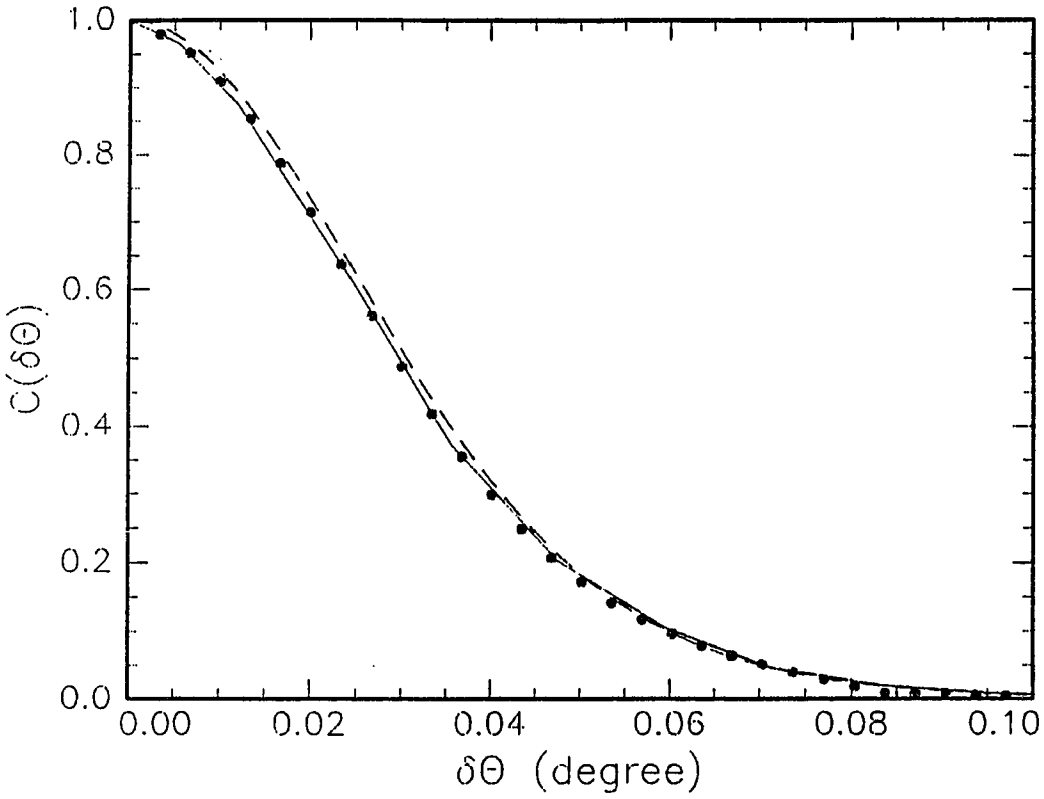

Figure 3.8

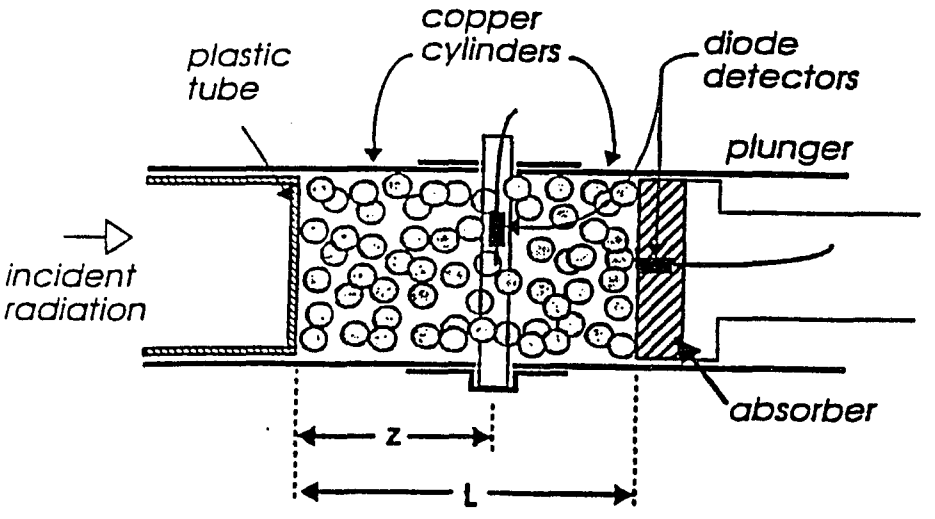
plastic
tube
copper
cylinders
diode
detectors
plunger
incident
radiation
absorber
z
L

Figure 4.1

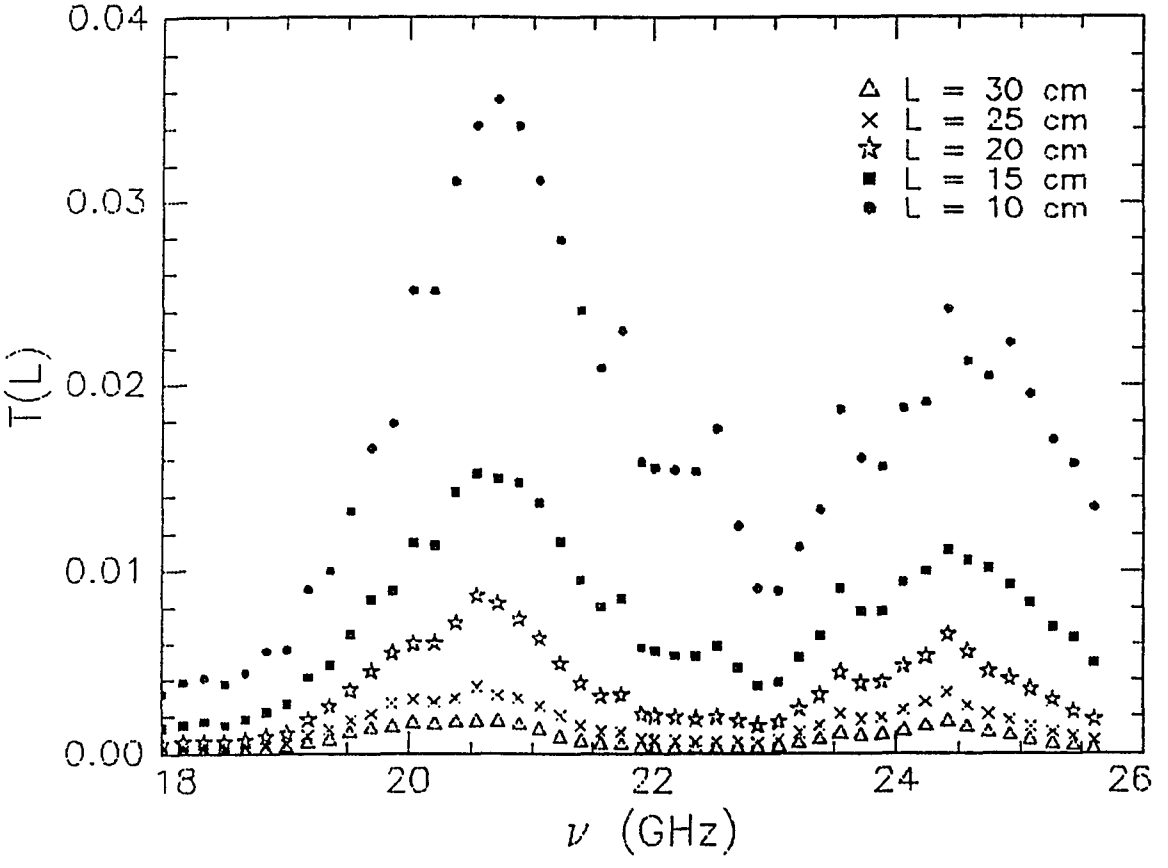
0.04
0.03
0.02
0.01
0.00
T(L)
18
20
22
24
26
ν (GHz)
L = 30 cm
L = 25 cm
L = 20 cm
L = 15 cm
L = 10 cm

Figure 4.2

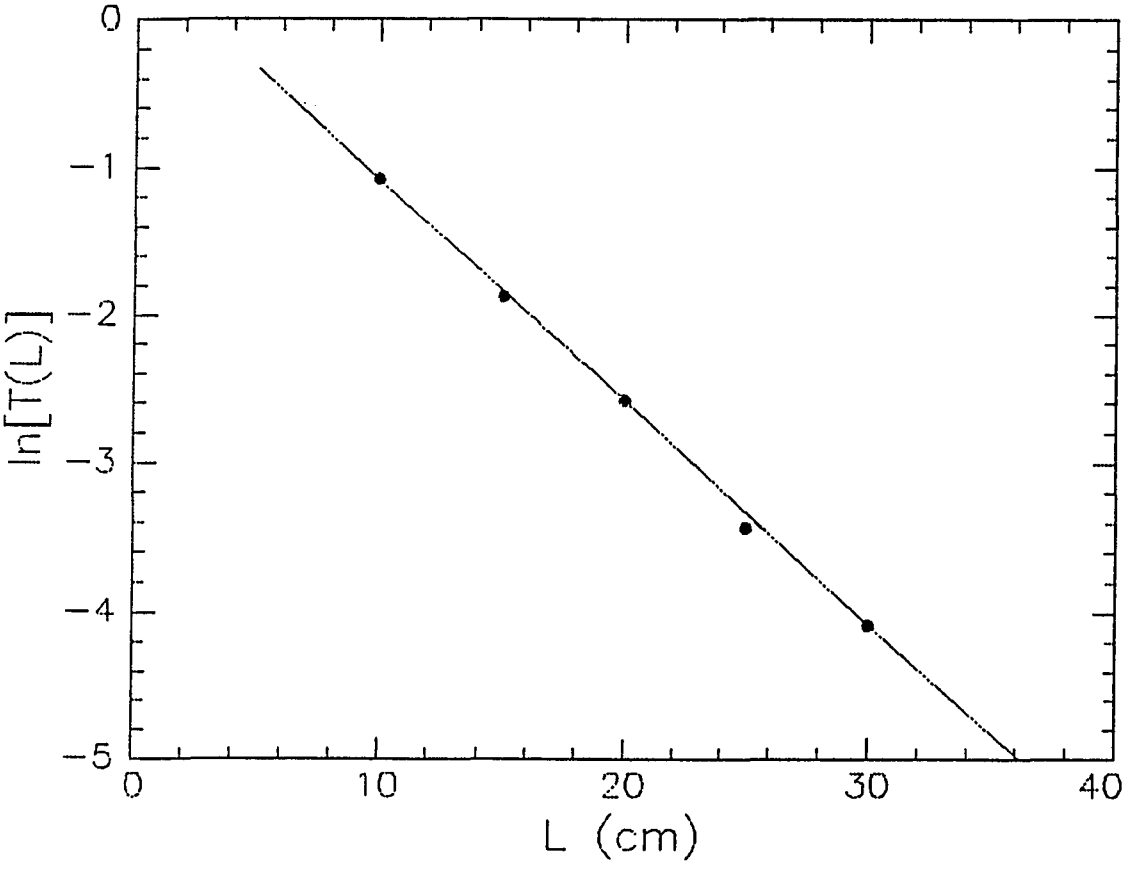

Figure 4.3

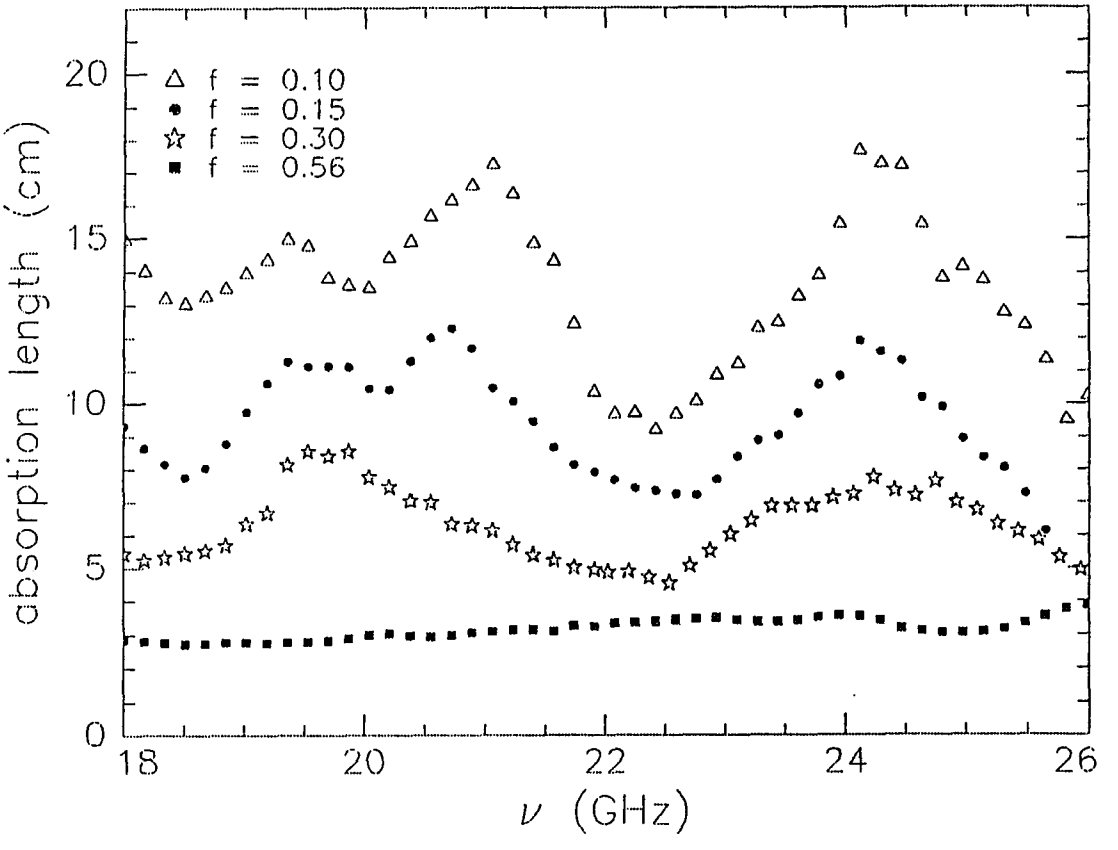
absorption length (cm)
20
15
10
5
0
18
20
22
24
26
ν (GHz)
f = 0.10
f = 0.15
f = 0.30
f = 0.56

Figure 4.4

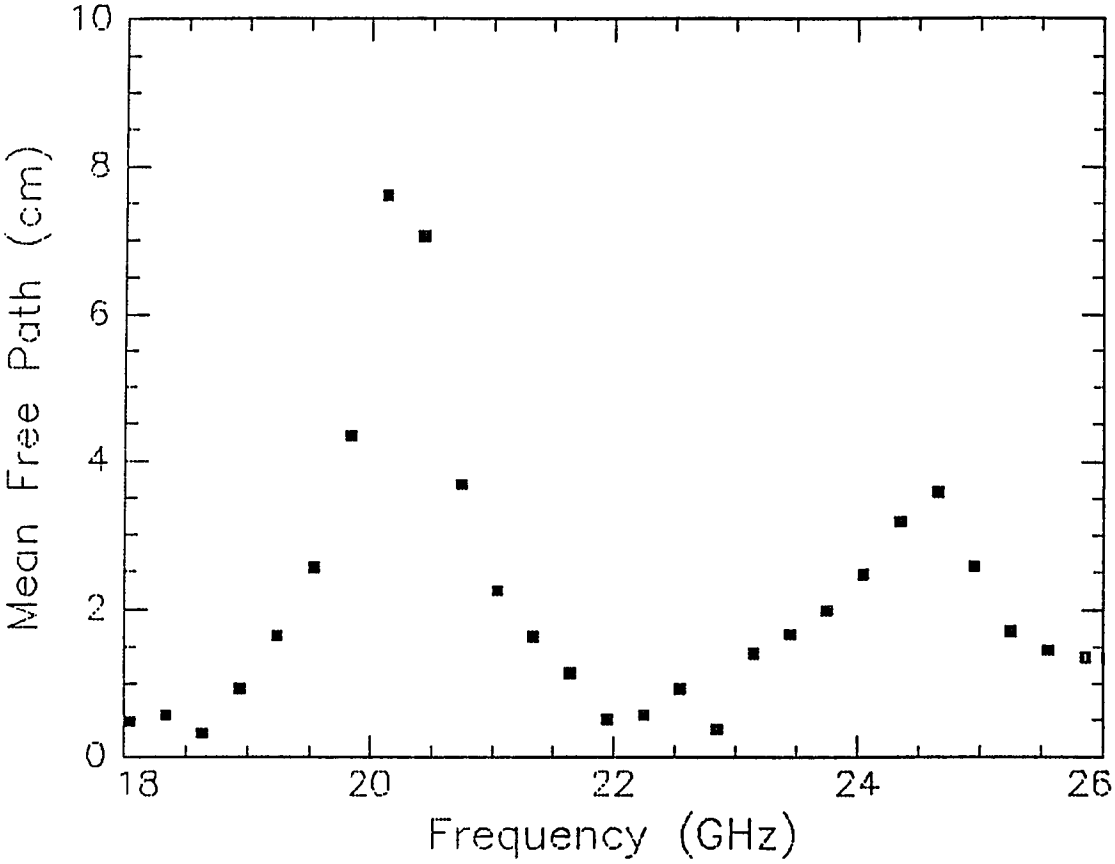

Figure 4.5

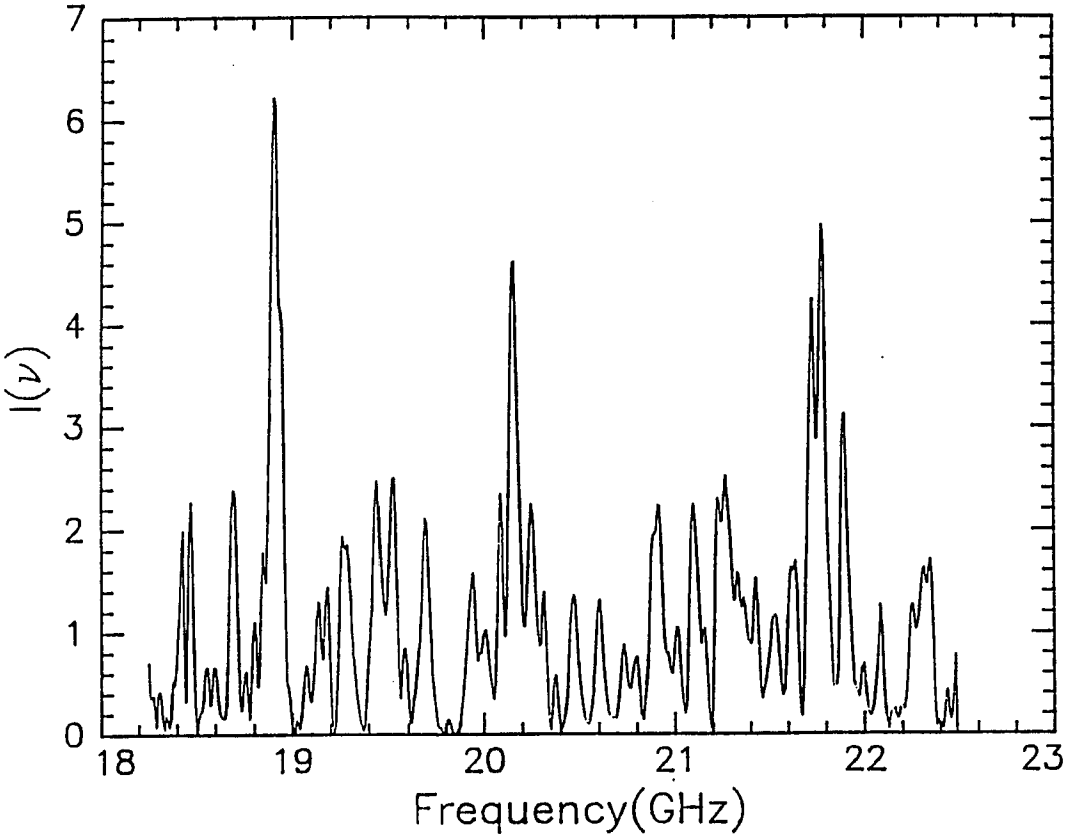

Figure 4.6

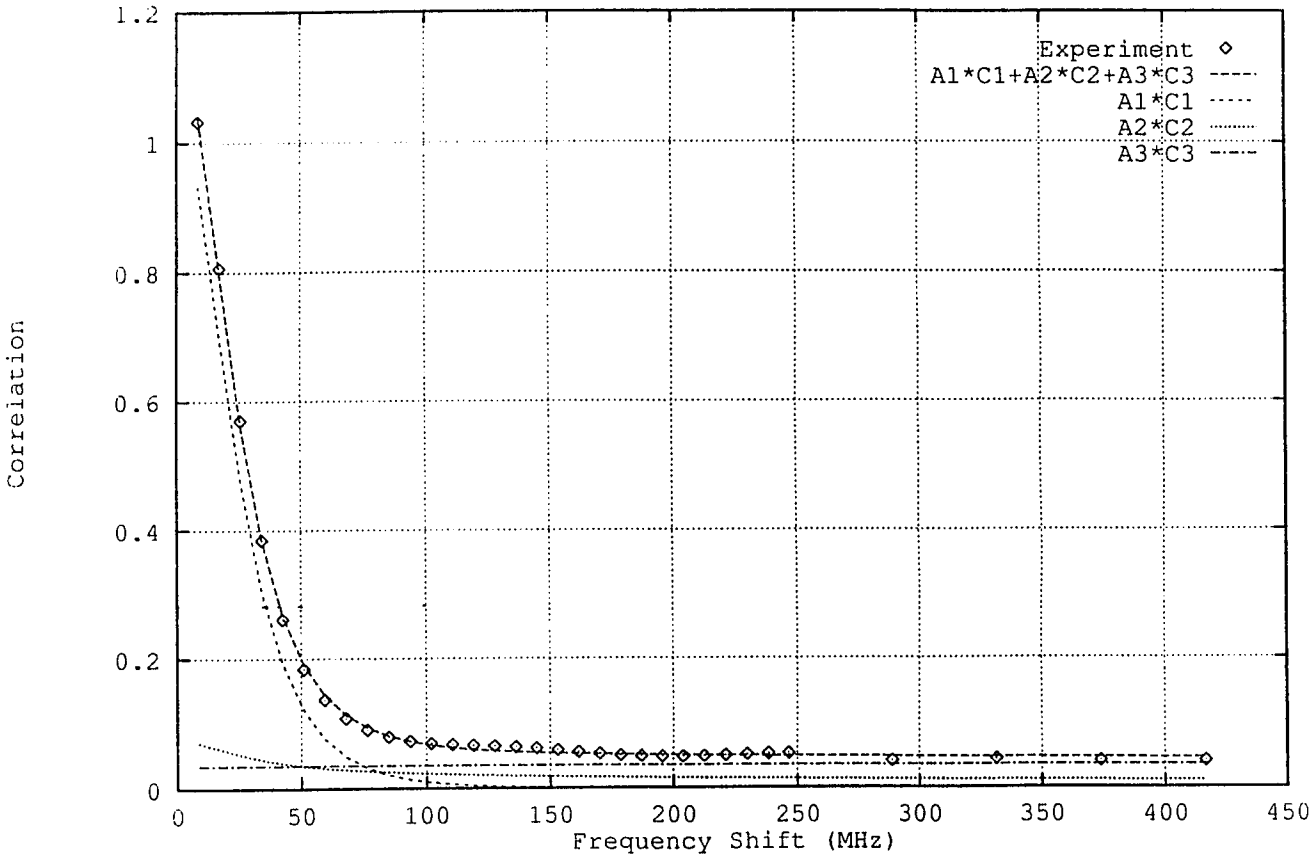
Correlation
Frequency Shift (MHz)
Experiment
A1*C1+A2*C2+A3*C3
A1*C1
A2*C2
A3*C3
1.2
1
0.8
0.6
0.4
0.2
0
0
50
100
150
200
250
300
350
400
450

Figure 4.7

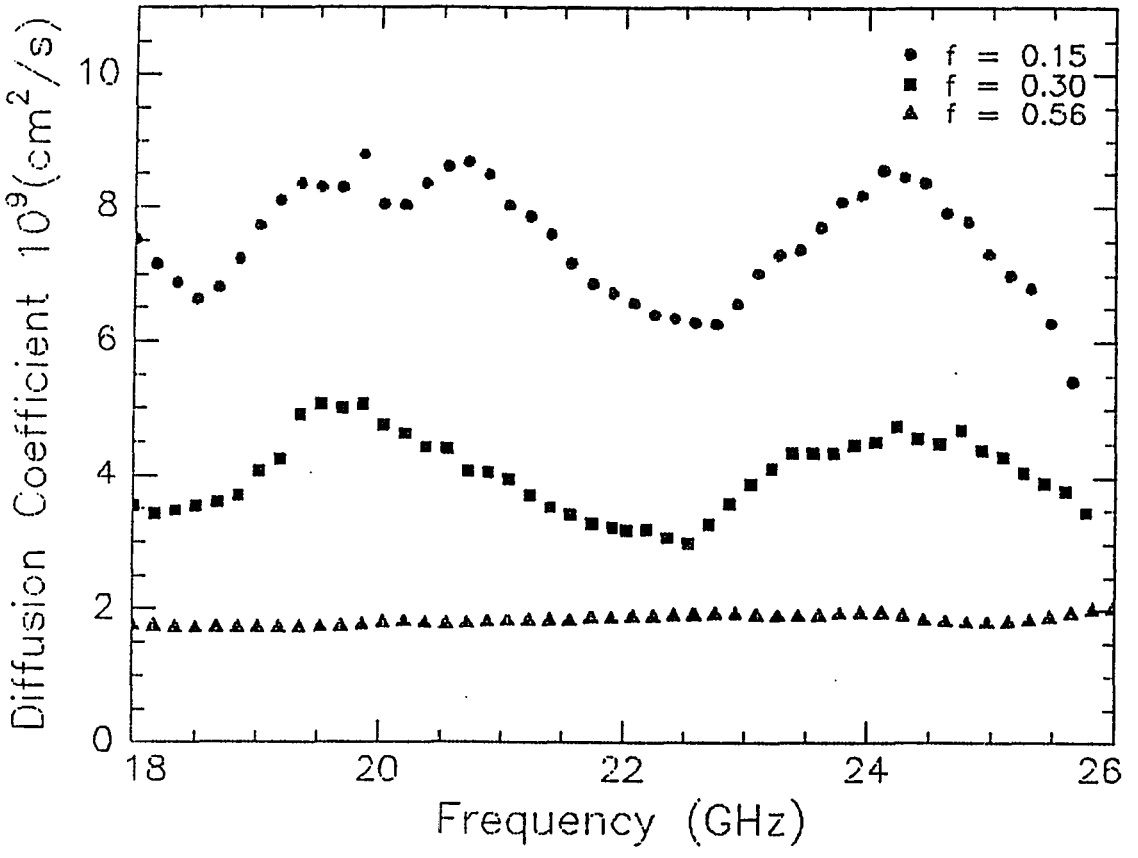
Diffusion Coefficient $10^9(cm^2/s)$
Frequency (GHz)
f = 0.15
f = 0.30
f = 0.56
0
2
4
6
8
10
18
20
22
24
26

Figure 4.8

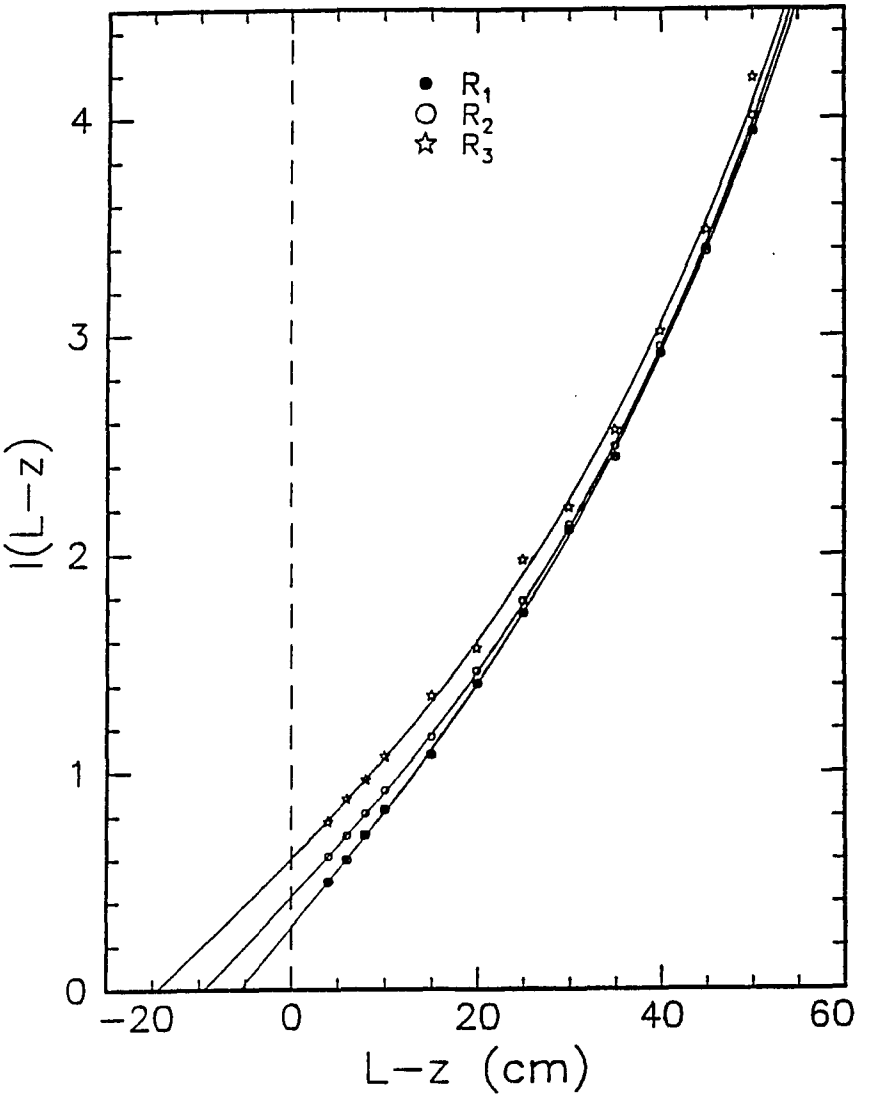

Figure 4.9

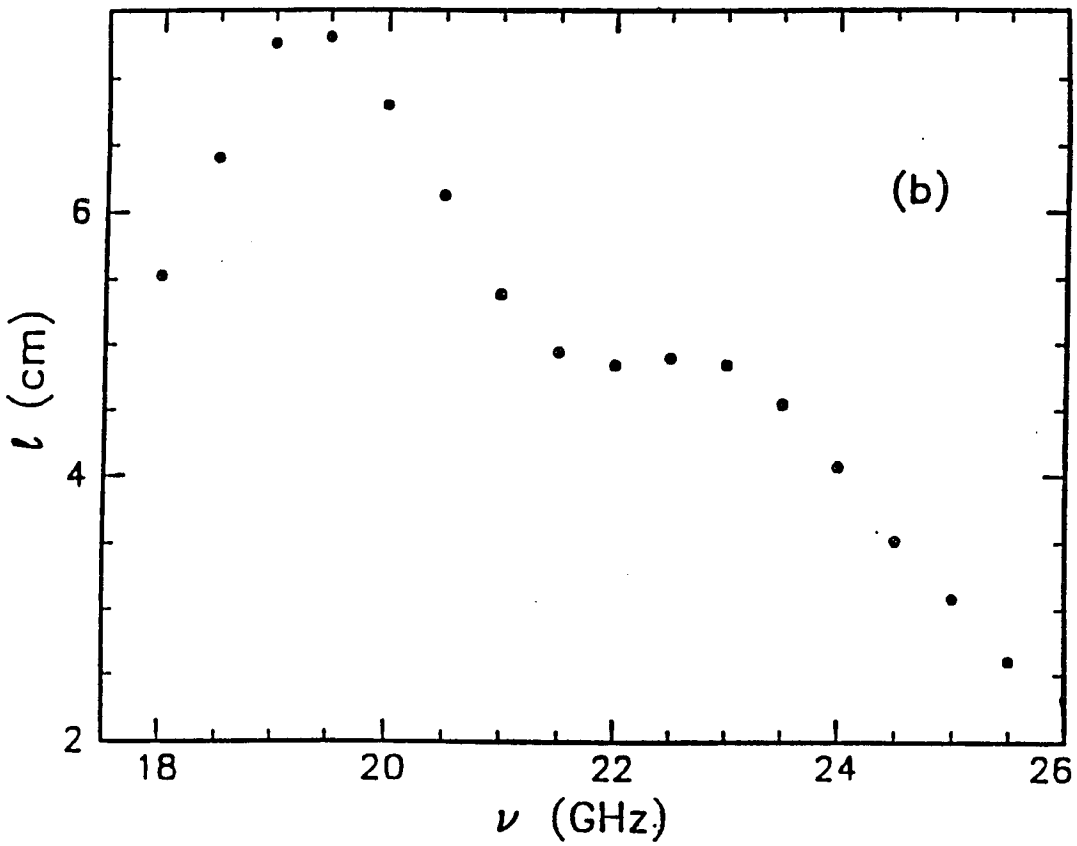

Figure 4.10

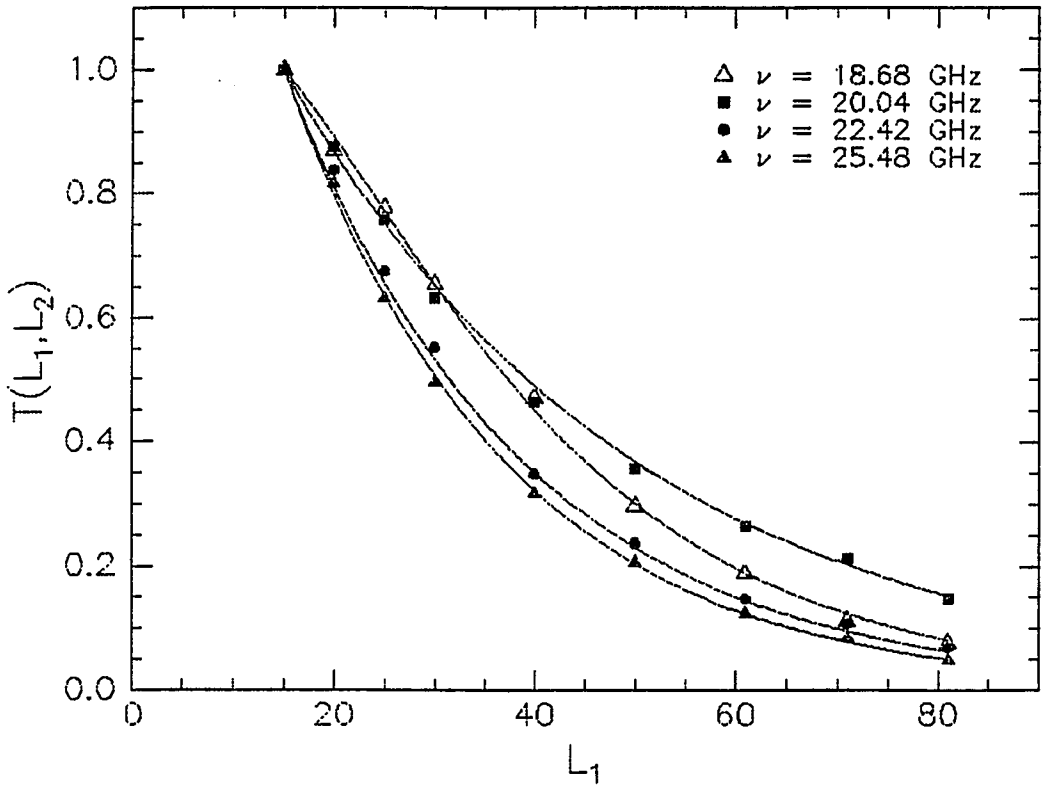
1.0
0.8
0.6
0.4
0.2
0.0
0
20
40
60
80
$T(L_1, L_2)$
L_1
△ ν = 18.68 GHz
■ ν = 20.04 GHz
● ν = 22.42 GHz
▲ ν = 25.48 GHz

Figure 4.11

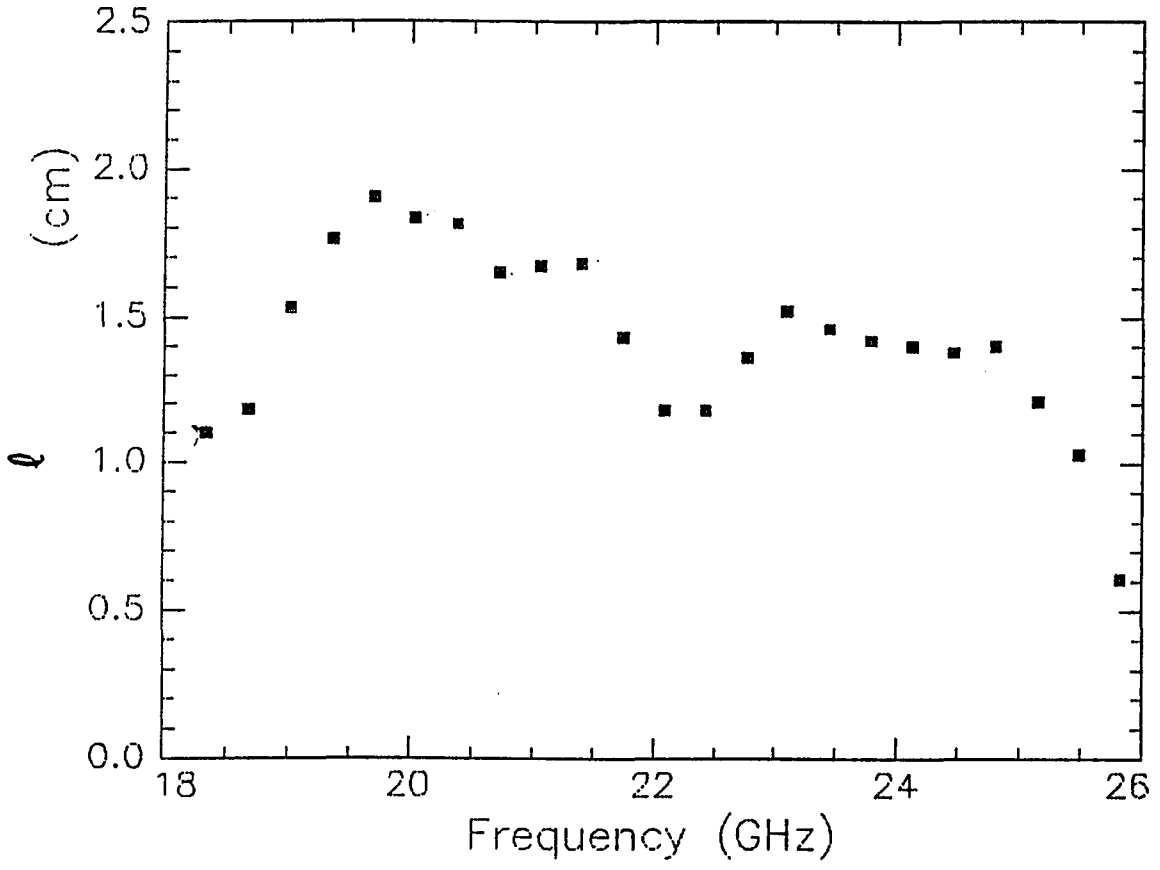

Figure 4.12

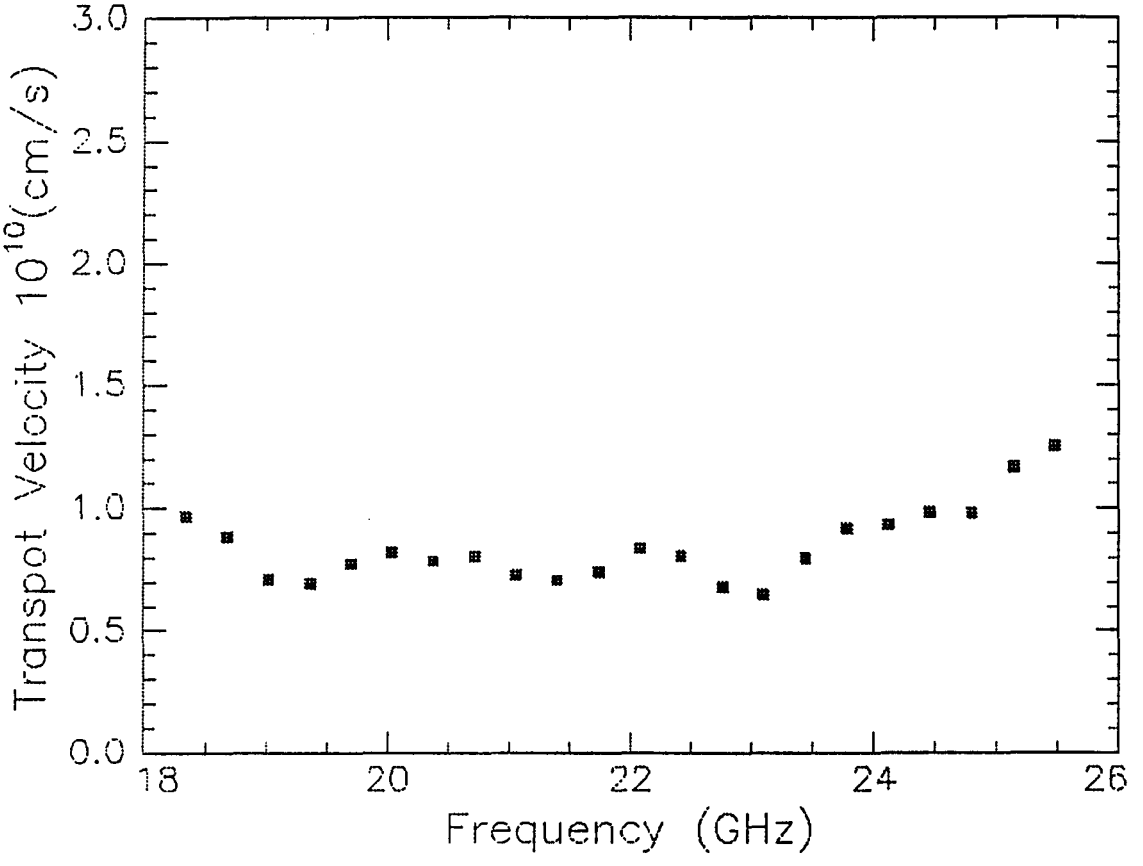
Transpot Velocity 10^{10}(cm/s)
3.0
2.5
2.0
1.5
1.0
0.5
0.0
18
20
22
24
26
Frequency (GHz)

Figure 4.13

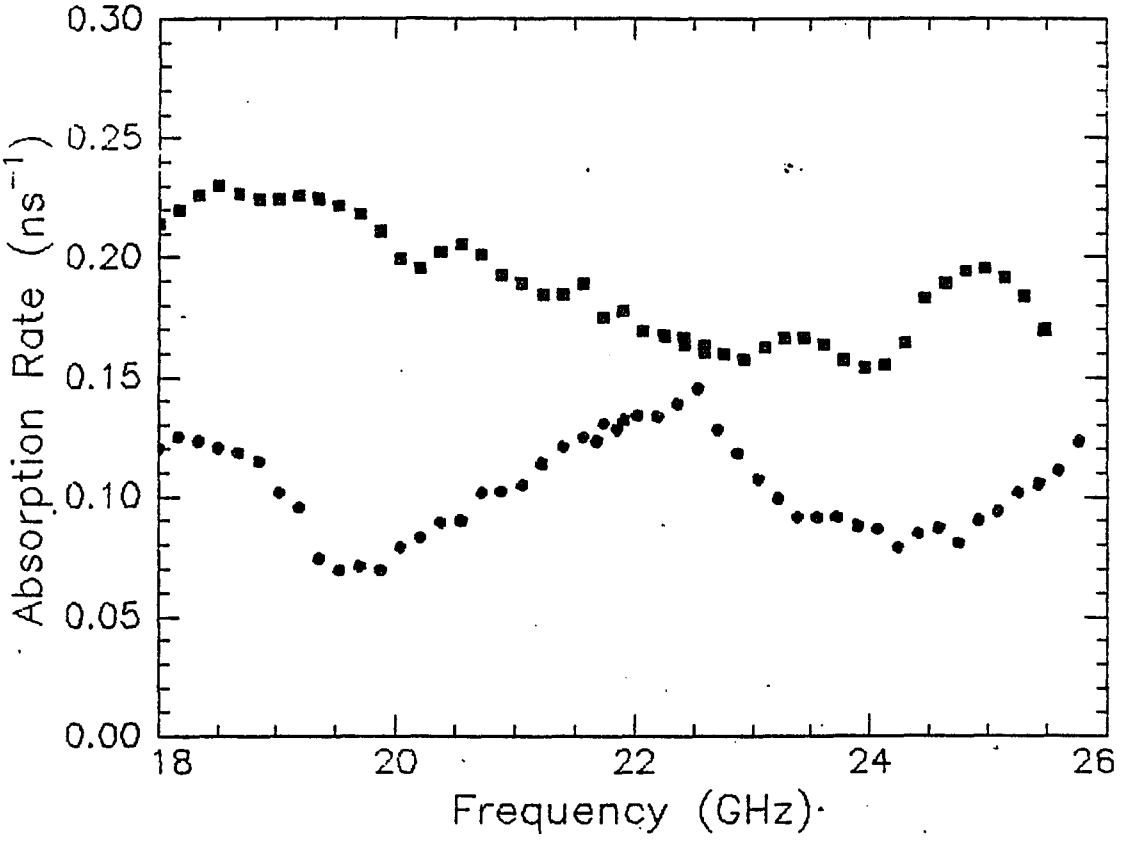
0.30
0.25
0.20
0.15
0.10
0.05
0.00
Absorption Rate (ns^{-1})
18
20
22
24
26
Frequency (GHz)

Figure 4.14

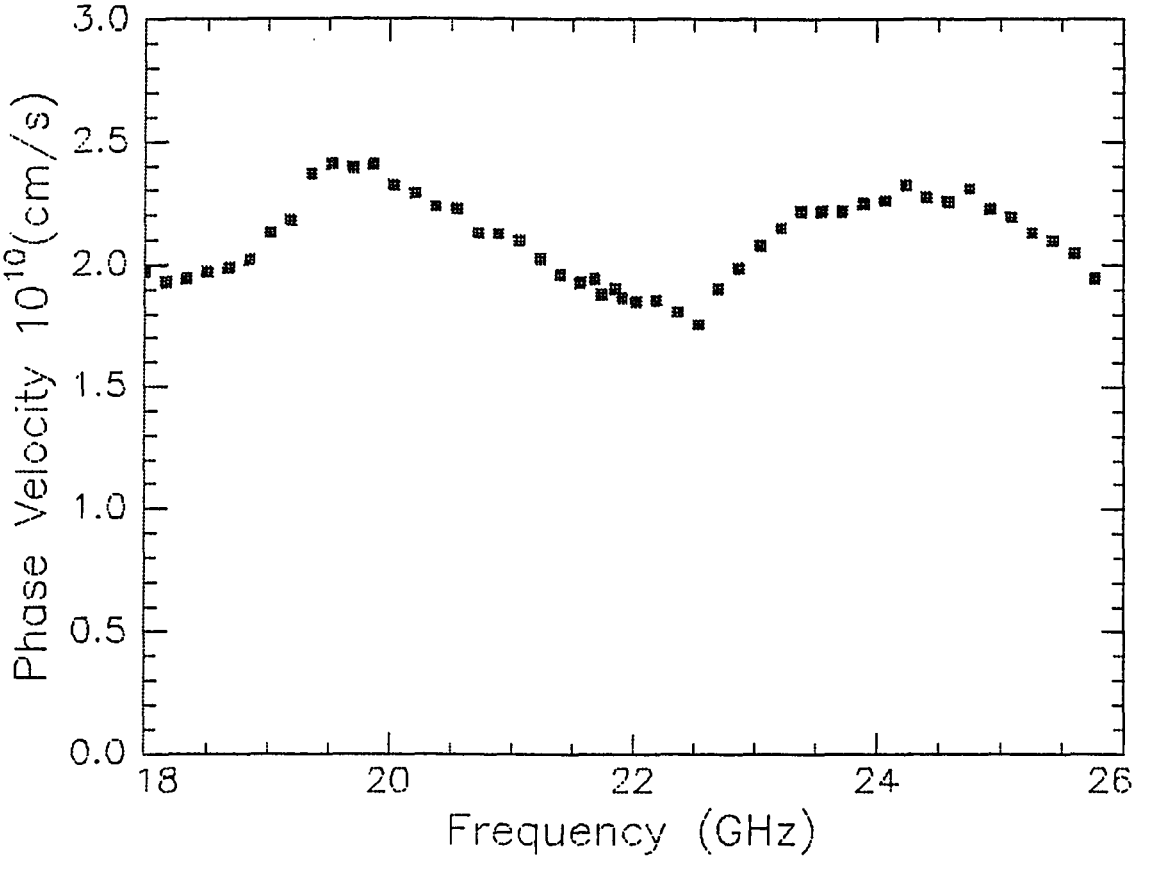
3.0
2.5
2.0
1.5
1.0
0.5
0.0
Phase Velocity 10^{10}(cm/s)
18
20
22
24
26
Frequency (GHz)

Figure 4.15

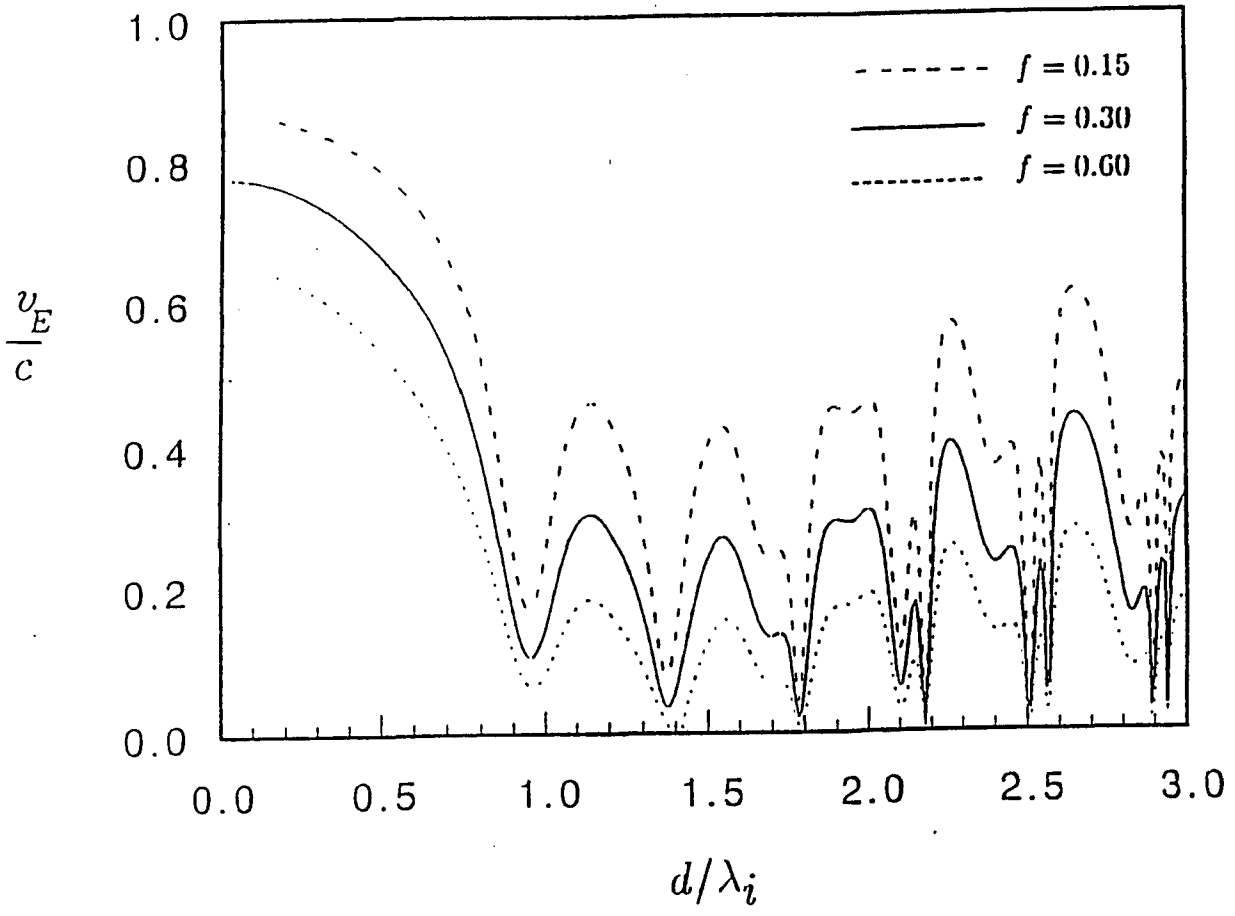
1.0
0.8
0.6
0.4
0.2
0.0
$\frac{v_E}{c}$
0.0
0.5
1.0
1.5
2.0
2.5
3.0
d/λ_i
$f = 0.15$
$f = 0.30$
$f = 0.60$

Figure 4.16

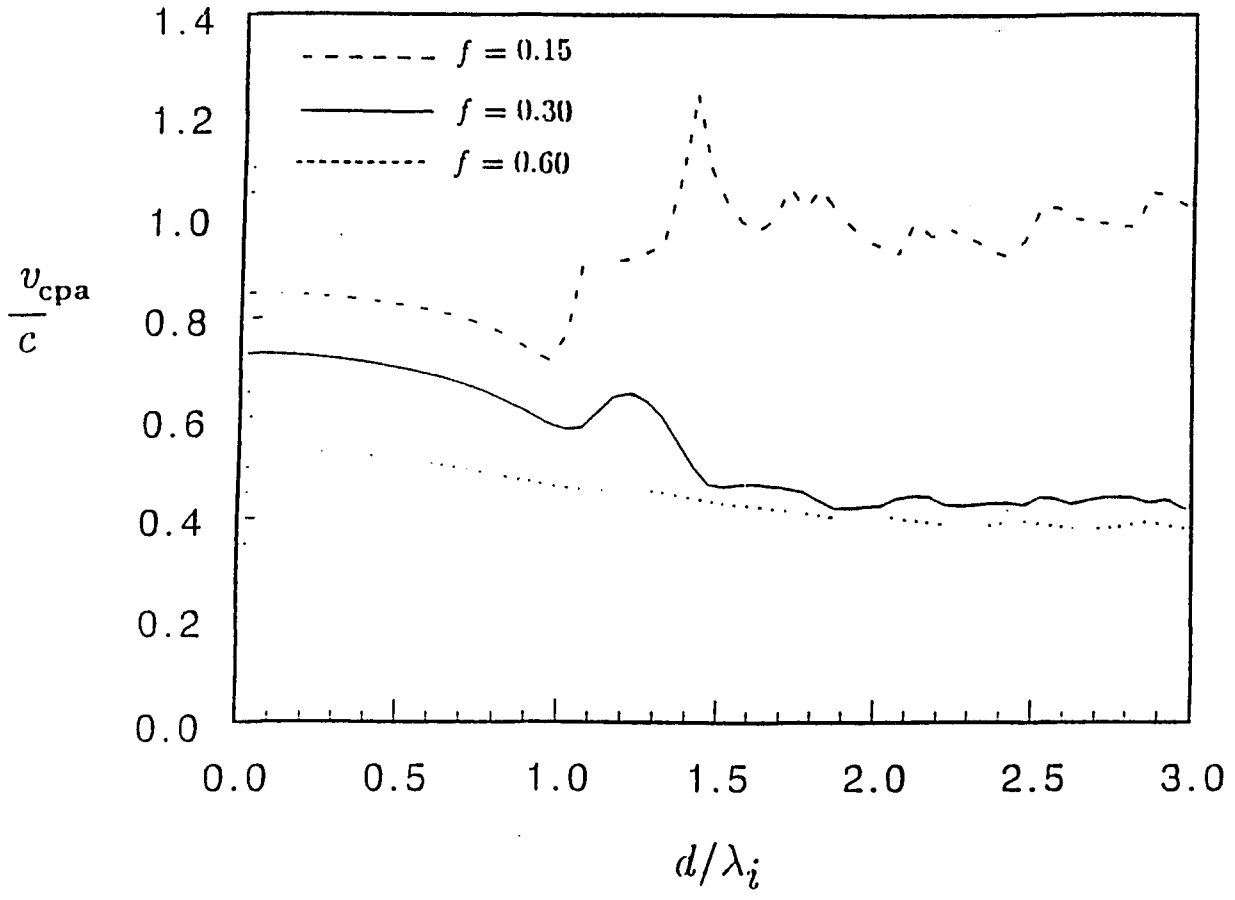
1.4
1.2
1.0
0.8
0.6
0.4
0.2
0.0
$\frac{v_{cpa}}{c}$
$f = 0.15$
$f = 0.30$
$f = 0.60$
0.0
0.5
1.0
1.5
2.0
2.5
3.0
d/λ_i

Figure 4.17

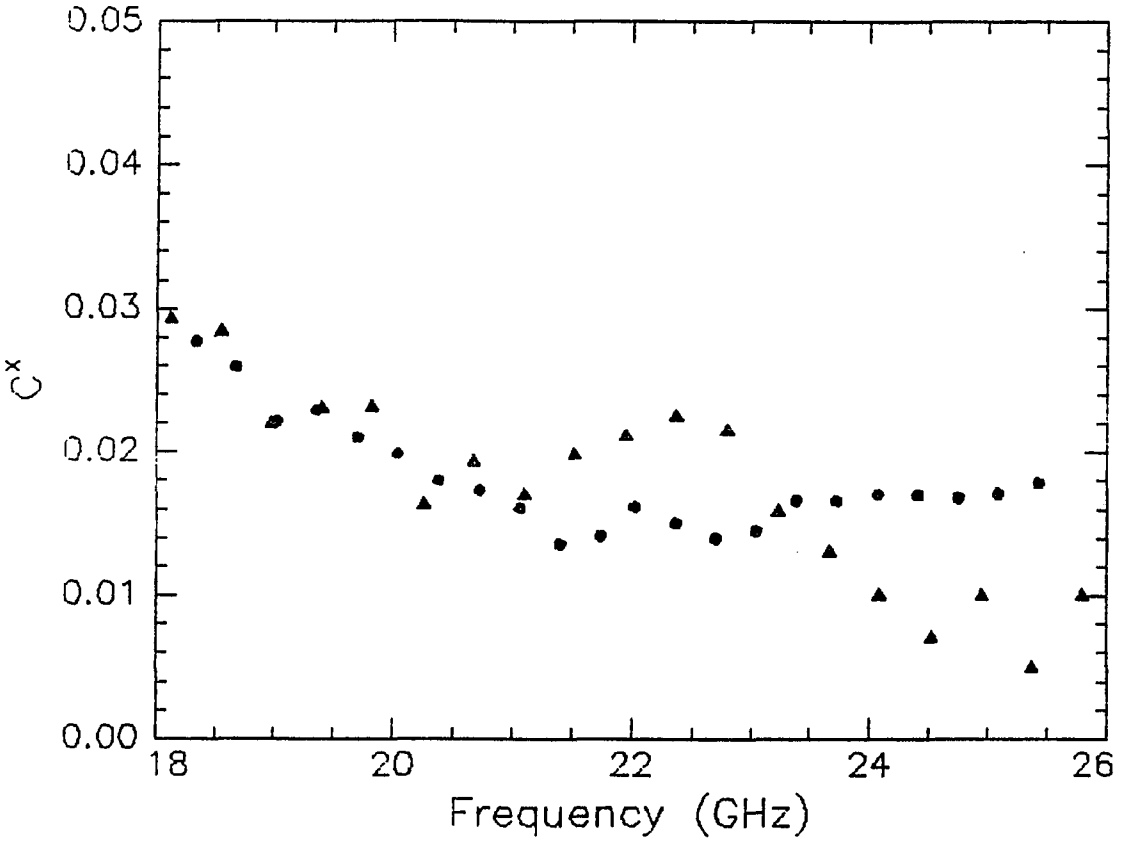

Figure 4.18

REFERENCES

1. *The Scattering and Localization of Classical Waves,* P. Sheng, ed., World Scientific Press, Singapore (1990).

2. A.Z. Genack, Phys. Rev. Lett. 58 (1987) 2043.

3. A. Z. Genack and J.M. Drake, Europhys. Lett. 11 (1990) 331.

4. Y. Kuga and A. Ishimaru, J. Opt. Soc. Am. A 1 (1984) 831.

5. M.P. van Albada and A. Lagendijk, Phys. Rev. Lett. 55 (1985) 2692.

6. P.E. Wolf and G. Maret, Phys. Rev. Lett. 55 (1985) 2696.

7. E. Akkermans and R. Maynard, J. Phys. France Lett. 46 (1985) L1045.

8. G. Maret and P.E. Wolf, Z. Phys. B 65 (1987) 409.

9. M. Rosenbluh, M. Hosen, I. Freund and M. Kaveh, Phys. Rev. Lett. 58 (1987) 2754.

10. D.J. Pine, D.A. Weitz, P.M. Chaikin and E. Herbolzheimer, Phys. Rev. Lett. 60 (1988) 1134.

11. A.G. Yodh, P.D. Kaplan and D.J. Pine, Phys. Rev. B 42 (1990) 4744.

12. R. Berkovits, M. Kaveh and S. Feng, Phys. Rev. B 40 (1989) 737.

13. A. Lagendijk, R. Vreeker and P. de Vries, Phys. Lett. A 136 (1989) 81.

14. R. Berkovits, M. Kaveh and S. Feng, Phys. Rev. B 40 (1989) 737.

15. F.C. MacKintosh, S. John, Phys. Rev. B 40 (1989) 2383.

16. I. Freund and R. Berkovits, Phys. Rev. B 41 (1990) 496.

17. N. Garcia, J.H. Li, W. Polkosnik, T.D. Cheung, P. Tsang, A.A. Lisyansky and

A.Z. Genack, Physica B 175 (1991) 9.

18. M.P. van Albada, B.A. Tiggelen A. Lagendijk and A. Tip, Phys. Rev. Lett. 66 (1991) 3132.

19. J.H. Li, N. Garcia and A.Z. Genack, Bull. Amer. Phys. Soc. 36 (1991) 358.

20. J.X. Zhu, D.J. Pine, and D.A. Weitz, Phys. Rev. A 44 (1991) 3948.

21. P.M. Saulnier and G.H. Watson, Opt. Lett 17 (1992) 946.

22. N. Garcia, A.Z. Genack, and A.A. Lisyansky, Phys. Rev. B 46 (1992) 14475.

23. J.H. Li, A.A. Lisyansky, T.D. Cheung, D. Livdan and A.Z. Genack, Europhys. Lett. 22 (1993) 675.

24. A.Z. Genack, J.H. Li, N. Garcia and A.A. Lisyansky, in: *Photonic Band Gaps and Localization*, edited by C.M. Soukoulis (Plenum, New York, 1993).

25. M.J. Stephen and G. Cwilich, Phys. Rev.Lett. 59 (1987) 285.

26. P.A. Mello, Phys. Rev. Lett. 60 (1988) 1089.

27. P.A Mello, E Akkermans and B. Shapiro, Phys. Rev. Lett. 61 (1988) 459.

28. S. Feng, C. Kane, P.A. Lee and A.D. Stone, Phys. Rev. Lett. 61 (1988) 834.

29. N. Garcia and A.Z. Genack, Phys. Rev. Lett. 63 (1989) 1678.

30. A.Z. Genack, N. Garcia and W. Polkosnik, Phys. Rev. Lett. 65 (1990) 2129.

31. M.P. van Albada, J.F. de Boer and A. Lagendijk, Phys. Rev. Lett. 64 (1990) 2787.

32. S. John, Phys. Rev. Lett. 53 (1984) 2169.

33. J.B. Pendry and P.D. Kirkman, J. Phys. C 17 (1984) 6711.

34. P.W. Anderson, Philos. Mag. 52 (1985) 505.

35. P. Sheng and Z.Q. Zhang, Phys. Rev. Lett. 57 (1986) 1879.

36. C.A. Condat and T.R. Kirkpatrick, Phys. Rev. Lett. 58 (1987) 226.

37. N. Garcia and A.Z. Genack, Phys. Rev. Lett. 66 (1991) 1850.

38. A.Z. Genack and N. Garcia, Phys. Rev. Lett. 66 (1991) 2064.

39. A.F. Ioffe and A.R. Regel, Prog. on Semi-conductors 4 (1960) 237.

40. E. Abrahams, P.W. Anderson, D.C. Licciardello and T.V. Ramakrishnan, Phys. Rev. Lett. 42 (1979) 673.

41. D.J. Thouless, Phys. Rep. 13C (1974) 93.

42. A.Z. Genack, Europhys. Lett. 11 (1990) 733.

43. M.B. van Mark van M. P. Albada and A. Lagendijk, Phys. Rev. B 37 (1988) 3573.

44. A.A. Lisyansky, J.H. Li, D. Livdan, N. Garcia, T.D. Cheung and A.Z. Genack, in: *Photonic Band Gaps and Localization*, edited by C.M. Soukoulis (Plenum, New York, 1993).

45. P.M. Morse, H. Feshbach, *Methods of Theoretical Physics* (McGraw-Hill, New York, N.Y.) 1953.

46. M. Lax, V. Nayaramamurti, and R.C. Fulton, in *Proceedings of the Symposium on Laser Optics and Condensed Matter*, J.L. Birman, H.Z. Cummins and A.A. Kaplyanskii, eds.

47. K.M. Yoo, F. Liu and R.R. Alfano, Phys. Rev Lett. 64 (1990) 2647.

48. van Albada, M.B. Mark and A. Lagendijk, in *The Scattering and Localization of Classical Waves*, P. Sheng, ed., World Scientific Press, Singapore (1990), p. 97.

49. *Laser speckle and Related Phenomena, Topics in Applied Physics* v. 9, ed. J.C.

Dainty (Springer-Verlag, Berlin, 1984).

50. I. Freund, M. Rosenbluh and R. Berkovits, Phys. Rev. B 39 (1989) 12403.

51. J.H Li and A.Z. Genack, preprint.

52. M. Born and E. Wolf, *Principles of Optics*, 4th ed. (Pergamon Press, New York, 1970) pp. 508.

53. C.F. Bohren and D.R. Huffman, *Absorption and Scattering of Light by Small Particles*, (Wiley, New York, 1983).

54. Yu.N. Barabanenkov and V.D. Ozrin, Phys. Rev. Lett. 69 (1992) 1364.

55. G. Cwilich and Y. Fu, preprint.

56. J. Kroha, C.M. Soukoulis and P. Wölfle, preprint.

57. C.M. Soukoulis, S. Datta and E.N. Economou, preprint.

58. J.M. Drake and A.Z. Genack, Phys. Rev. Lett. 63 (1989) 259.

59. R. Pnini and B. Shapiro, Phys Lett. A 157 (1991) 265.

60. E. Kogen and M. Kaveh, Phys. Rev. B 45 (1992) 1049.